論文 / 著書情報
Article / Book Information

題目(和文)	放電加工とレーザ加工用高速・多自由度磁気浮上アクチュエータの研究
Title(English)	High speed and multi-DOF maglev actuators for electrical discharge machining and laser beam machining
著者(和文)	何 冬覚
Author(English)	Dongjue He
出典(和文)	学位:博士(工学), 学位授与機関:東京工業大学, 報告番号:甲第8950号, 授与年月日:2012年9月25日, 学位の種別:課程博士, 審査員:進士 忠彦
Citation(English)	Degree:Doctor (Engineering), Conferring organization: Tokyo Institute of Technology, Report number:甲第8950号, Conferred date:2012/9/25, Degree Type:Course doctor, Examiner:
学位種別(和文)	博士論文
Type(English)	Doctoral Thesis

High Speed and Multi-DOF Maglev Actuators for Electrical Discharge Machining and Laser Beam Machining

Supervised by

Professor Tadahiko SHINSHI

Professor Haruo HOUJOH

Department of Mechano-Micro Engineering

Tokyo Institute of Technology

Dongjue HE

August 2012

Table of contents

Chapter 1 Introduction

1.1 Background

1.1.1 Electrical discharge machining

Electrical discharge machining (EDM) is an un-conventional material removal process based on the thermo-electric energy created between an electrically conductive work-piece and an electrode immerged in a dielectric fluid (machining fluid) [1]. In EDM, the thermo discharge spark generates great amounts of heat in a small area on the work-piece surface which would melt and remove the melted material at a temperature in the range of 8000 to 12,000 °C [2] or even as high as 20,000 °C [3].

Its unique features of using thermal energy to machine all electrically conductive parts regardless of hardness, and having the ability to deal with complex shapes, micro holes have been its distinctive advantage in the manufacture of mould, die, automotive, aerospace and surgical components. In addition, compared to cutting machining, EDM does not make direct contact between the electrode and the work-piece, which can eliminate mechanical stress, chatter and vibration problems of tools during machining, and makes the micro tools easier available [4].

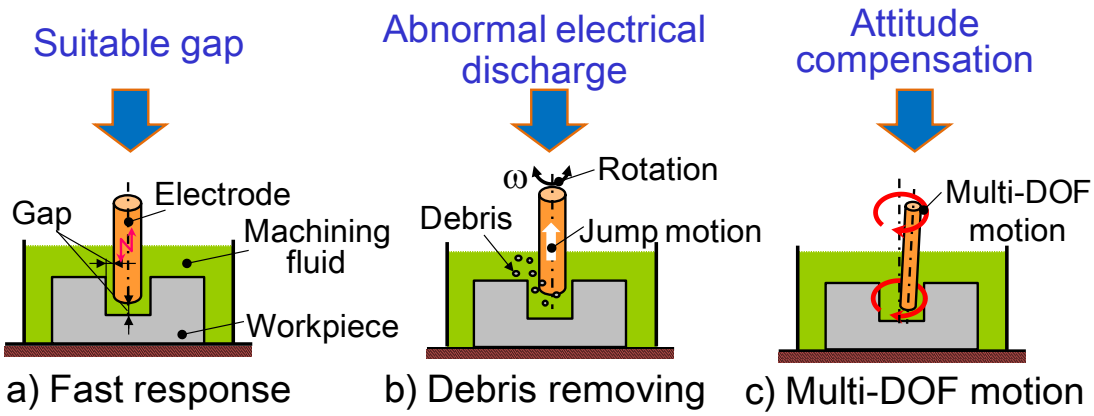

Fig. 1.1 Challenges of electrical discharge machining

In EDM, the machining speed largely depends on probability and efficiency of the electrical discharges. To obtain a stable electrical discharge, it is

necessary to keep a suitable gap distance between the electrode and the work-piece for generating the discharge sparks. However, during the process of EDM, material is being removed from both the electrode and the work-piece, so that the gap distance between them is changing. Therefore, the electrode or the work-piece should be re-positioned quickly and precisely to maintain the suitable gap distance.

However, there are some challenges for the conventional EDM machine to achieve higher machining speed and better machining quality, as shown in Fig. 1.1. In conventional electrical discharge machine tools, stacked one degree of freedom (1-DOF) lead-screw mechanisms or linear positioning tables are normally used for positioning the electrode or work-piece, the positioning response of such mechanisms is somewhat slow, due to the rotary inertia of the lead-screw and the mass of the stacked tables, therefore, the electrode or the work-piece cannot be re-positioned sufficiently quickly to maintain the suitable gap distance [5, 6].

In addition, machining debris accumulating around the electrode would lead abnormal electrical discharge or short circuit during EDM, and decrease the machining efficiency and accuracy. Therefore, the debris is desired to be removed by applying a rotation and/or a high speed jump motion to the electrode, as shown in Fig. 1.1(b). Unfortunately, a conventional electrical discharge machine cannot remove the debris efficiently, especially in the case of machining small holes with a high aspect ratio.

Furthermore, conventional EDM machine tools cannot realize a multi-DOF motion as shown in Fig. 1.1(c). Such a motion can help compensating the attitude of the electrode, and this is benefit for eliminating the electrode clamping error and for realizing a multi-DOF profile machining.

In order to overcome the encountered challenges of conventional EDM machine mentioned above, high speed and multi-DOF actuator for driving an electrode during EDM process is required.

1.1.2 Laser beam machining

Laser beam machining (LBM) is another non-contact machining method which is widely used in many industries. In the LBM process, a high energy laser beam can not only cut almost any material without contact with the work-piece, but can also machine complex geometrical profiles and make miniature holes in the material. The high energy laser beam is focused by a lens to melt and vaporize the work-piece material and the molten material is blown away by an assist gas jet acting at the cutting front [7, 8].

Laser beam cutting is the most frequently performed material removal process in laser beam machining. In laser beam cutting, the capability with which the assist gas removes molten material from the cutting front is reduced as the work-piece becomes thicker. Insufficient gas flow to the cutting front decreases the cutting speed, and generates burr, dross and recast layers [9-11].

In order to improve cutting speed and the capability to remove molten material, as well as to save on the consumption of assist gas, a machining method that applies a suitable eccentricity between the axis of the laser beam (i.e. lens axis) and the axis of a convergent assist gas supply nozzle (off-axis control) was proposed [12], as shown in Fig. 1.2 (a). The eccentricity between the laser beam axis and the convergent nozzle axis was manually adjusted for each experiment.

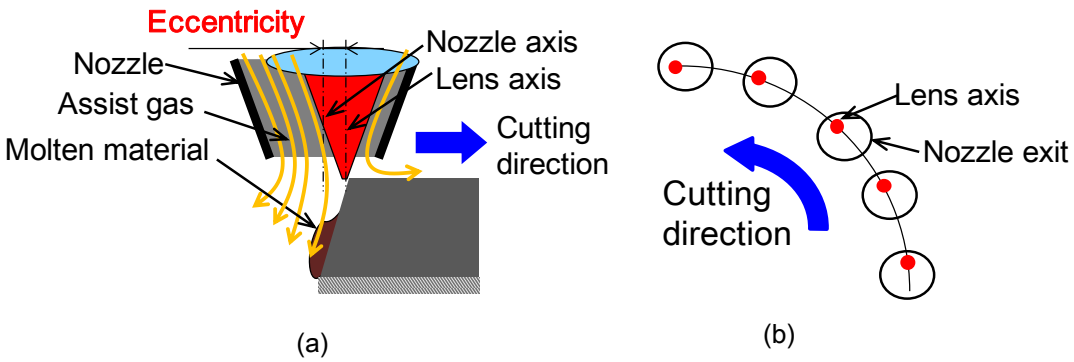

Fig. 1.2 Off-axis laser beam cutting realized by radial motion of the lens

The effect of the off-axis position was also verified using a supersonic nozzle in a straight laser beam cutting experiment. The nozzle angle and the distance

between the injection point of the gas jet and the laser beam were changed manually for each experiment [13, 14].

However, real-time off-axis control of the lens has not been realized by a conventional LBM machine tool, which is required in two-dimensional laser beam cutting. In two-dimensional off-axis laser beam cutting, a relative displacement between the nozzle and the laser beam following the two-dimensional reference cutting trajectory needs to be generated, as shown in Fig. 1.2 (b).

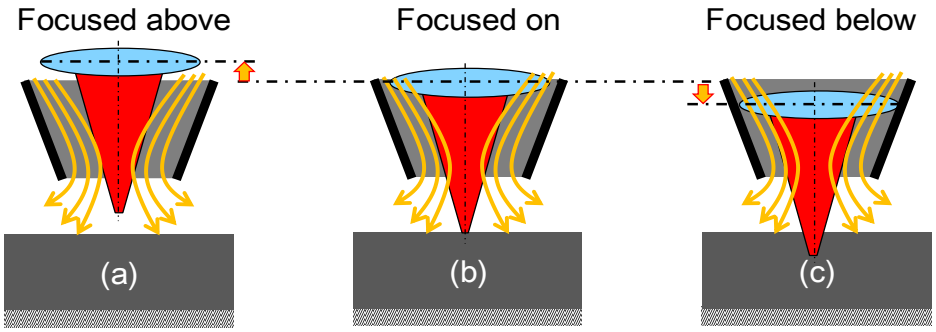

Fig. 1.3 Focal point adjustment realized by axial motion of the lens

On the other hand, the focusing position, defined as the gap between the lens and the surface of the work-piece, is another of the more critical process parameters. The laser beam focal point, as shown in Fig. 1.3 (a. focused above, b. focused on and c. focused below the surface of the work-piece), can be optimized according to the material and thickness of the work-piece to achieve the desired machining accuracy, speed and surface quality in various laser beam machining processes [15-19].

In previous research, the focal point was manually adjusted and fixed during the machining process; however, high speed real-time adjustment of the focal point responding to changes in the thickness and material of the work-piece has not, so far, been reported.

Considering that an optic lens has much smaller size and mass compared to an assist gas nozzle, the lens is usually chosen to be driven for realizing the off-axis control and focal point adjustment.

Therefore, in order to realize the relative displacement between the lens axis and the assist gas nozzle axis for two-dimensional off-axis laser beam cutting and adjust the focal point correctly and speedily during laser machining processes, a supplementary high speed and multi-DOF actuator which can drive the lens in three orthogonal directions is needed.

1.1.3 High speed and multi-DOF actuator

According to the introductions of EDM and LBM mentioned above, in order to obtain higher machining speed and better machining quality in EDM and LBM, both conventional EDM and LBM machine tools encountered some challenges. For EDM process, faster positioning response and multi-DOF motion of the electrode cannot be realized by conventional EDM machine tools. For LBM process, high speed real-time relative displacement between the lens and assist gas nozzle cannot realized by conventional LBM machine tools.

Therefore, development of additional actuators which can drive an electrode and/or a lens speedily and accurately in multi-DOF directions is a potential solution to achieve desired machining speed and quality in EDM and LBM. The developed actuators should have compact size and can be accommodated to conventional EDM and LBM machine tools as optional machining head.

In order to realize a multi-DOF motion, a stacked multi-DOF mechanism is commonly adopted. In the stacked mechanism, the large mass of the moving part limits the positioning response, and the large amount of components makes the structure relatively complex and difficult to realize a compact size [5, 6]. Furthermore, the tilt motion which required in EDM is difficult to be realized by the conventional stacked multi-DOF mechanism.

Parallel mechanism is another frequently adopted multi-DOF driving method. The parallel mechanism can realize very high positioning accuracy and large output driving force in orthogonal and tilt directions. However, the parallel

arranged actuation mechanism makes it have a relative large space size; furthermore, high positioning speed cannot be realized [20-22].

Over the past two decades, magnetic bearings have gained more and more interesting for developing multi-DOF magnetic levitated (maglev) systems. The magnetic bearings can generate electromagnetic driving force acting on the moving target directly without additional power transimisson components, thus the mass of moving part could be decreased, and this make it possible to achieve high positioning speed and to realize a compact size and light weight.

Additionally, the maglev actuator operating with almost zero friction and have no contacting moving parts, there is no wear within the 'system'. This gives extremely long lifetimes with minimal maintenance, resulting in cost effective operation and ownership [23, 24]. Therefore, the maglev technology is adopted for developing the high speed and multi-DOF electrode driving actuator for EDM and lens driving actuator for LBM in this study.

In a maglev electrode driving actuator for EDM, an electrode need to be attached to a rotating spindle shaft, and the spindle should be positioned speedily in three orthogonal and two tilt directions. In previous similar systems, such as in a turbo-machinery [25], in a gas turbine [26], in high speed cutting machine [27], et al, the magnetic bearings are mainly applied to support a rotating spindle, the high speed and multi-DOF motion of the levitated target cannot be realized.

On the other hand, in a maglev lens driving actuator for LBM, an optic lens with a diameter of 2 inch (50.8mm) need to be positioned in three orthogonal directions speedily. There have been several publications reporting similar maglev systems. Holmes et al. developed a 6-DOF controlled scanning stage, which achieved a positioning resolution of several nm and a travel range up to 25mm×25mm in the horizontal plane; however, the range of travel in the vertical direction was only 0.1mm, and the bandwidth was only 28Hz [28]. Shinno et al. designed an aerostatic levitated table driven by a linear motor for nano-machining, which realized a travel stroke of ±10mm in the horizontal plane,

but the vertical motion was constrained [29]. Kim et al. developed high-precision magnetic levitation stage for photolithography, the stage achieved 50mm×50mm positioning range in horizontal plane with positioning nose of 5nm, however, the axial motion was fixed [30]. Morimoto et al. reported two-DOF controlled lens driving actuators for laser cutting, where the lens was supported by elastic-hinges and driven by electro-magnets. With this actuator, two-DOF off-axis laser cutting and improvement of cutting speed and quality were realized, but the radial positioning range of the lens (±0.5mm) was insufficient for further high cutting speed, and axial motion of the lens was not considered [31].

Therefore, new maglev actuators with superior performance should be developed to satisfy the requirements in EDM and LBM.

1.2 Objective of this study

Considering the requirements for overcome the challenges encountered in EDM and LBM for improving the machining speed and quality, additional maglev actuators which can realize high speed and multi-DOF motion of an electrode and/or a lens need to be developed. The objectives of the EDM project and LBM project are stated as follows:

1.2.1 Objective of the EDM project

The purposes of the EDM project are:

Firstly, to develop a compact electrode driving actuator using maglev technology. The actuator should enable an electrode to realize multi-DOF motion in three orthogonal and two tilt directions, bandwidth of a few hundred Hz, several mm jump motion in axial direction, as well as high rotational accuracy of the electrode. The discharge voltage should be fed to the electrode without disturbing the levitation and rotation of the electrode.

Secondary, to construct experimental machining system, consisting of the

maglev electrode driving actuator and a conventional EDM machine, for high speed machining of small deep holes.

Finally, to machine small deep holes and micro holes using the developed maglev electrode driving actuator by EDM, and then evaluate the effectiveness of high speed positioning and rotation of electrode on the machining speed of EDM.

1.2.2 Objective of the LBM project

The purposes of the EDM project are:

Firstly, to develop a maglev lens driving actuator which can realize relative displacement between a lens and an assist gas nozzle in three orthogonal directions, positioning range of several mm, bandwidth of a few hundred Hz. In the actuator, a large aperture is required for attaching a lens with diameter of 2 inch and for the pass of high energy laser beam. The total size of the actuator should be as compact as possible to be accommodated to conventional laser beam machine tool.

Secondary, to evaluate the positioning performance of the developed maglev lens driving actuator.

1.3 Summary

This thesis is summarized as follows:

Chapter 2 “Maglev electrode driving actuator for EDM”

This chapter introduces the mechanical structures and the experimental performance of a new compact electrode driving actuator. The developed maglev actuator realizes 5-DOF motion of a spindle shaft by two radial magnetic bearings and one thrust magnetic bearing. A magnetic coupling mechanism is proposed to realize discharge voltage supply without a direct contact between

brushes and levitated spindle shaft, and to transmit rotational torque from a DC motor to the levitated spindle shaft for rotating the electrode which is attached to the spindle shaft. Furthermore, the magnetic coupling can generate a restoring force to balance the gravity of the spindle shaft.

Control system is designed for the fabricated compact maglev electrode driving actuator. The positioning resolution, full stroke, bandwidth, rotational accuracy, high speed multi-DOF motion and jump motion of the fabricated prototype maglev electrode driving actuator are also experimentally evaluated and discussed in this chapter.

Chapter 3 “Experimental EDM using the maglev electrode driving actuator”

This chapter discusses the problems of applying the prototype maglev electrode driving actuator to experimental EDM and the solutions. The positioning stroke of the prototype actuator is not enough for machining a deep hole with depth than 2mm, a co-operatively controlled EDM system using the prototype maglev electrode driving actuator combined with a conventional EDM machine is proposed to solve this problem.

The co-operative EDM system realizes as large travel range of the electrode as that of the conventional EDM machine, and realizes as fast positioning response of the electrode as that of the prototype maglev electrode driving actuator.

A new attachment mechanism is designed to eliminate the electrode chucking error. The machining schematic is also explained in this chapter.

Small through holes are experimentally machined by using the conventional EDM machine, alone, without electrode rotation; and by the co-operative EDM system, with electrode rotating from 0rpm to 1200rpm at intervals of 200rpm. The effectiveness of fast response and rotation of the electrode to machining speed is evaluated and discussed; the machining rate of each case is compared.

Micro electrode is on-machine fabricated for micro-hole EDM. Micro holes are machined by a conventional EDM machine, alone, without electrode rotation; by the co-operative EDM system, with and without electrode rotation. The machining rate and machined holes' depths are compared and discussed.

Chapter 4 “Maglev lens driving actuator for LBM”

This chapter presents a maglev lens driving actuator for realizing a high speed relative motion between a lens and an assist gas nozzle in three orthogonal directions.

A novel air core coil type electro-magnetic driving unit is proposed. The driving unit can generate both repulsive and attractive forces to a lens holder in both radial and thrust directions by utilizing a modified Halbach array on the driven target and the air core coils on the base. The air core coil windings allowed a spatial-cross-arrangement of the components, enabling the actuator to be sufficiently compact for it to be accommodated in the machining head of a laser beam machining tool.

In the fabricated prototype lens driving actuator, four driving units, which are off-set from horizontal axis and symmetrically arranged around the lens axis, are used to actuate a lens holder, a lens will be attached in a large aperture of the lens holder. The developed lens driving actuator can achieve real-time control of the axial position of the laser beam focal point and of the relative radial displacement between the lens axis and the assist gas jet nozzle axis (off-axis control).

The positioning resolution, full stroke and bandwidth of the prototype lens driving actuator are experimentally evaluated. Furthermore, the positioning performance of the maglev lens actuator under half sine wave (4G, 10ms) and sine wave (2G, 50Hz) acceleration will be experimentally evaluated and discussed.

Chapter 5 “Conclusions”

This chapter summarizes and discusses the achieved results in previous chapters. The future works of this study are also proposed.

Chapter 2 Maglev electrode driving actuator for EDM

2.1 Introduction

The challenges for achieving higher machining speed and better machining quality in EDM have been introduced in chapter 1. In previous research, in order to increase the positioning response of an electrode during EDM, the use of conventional electrical discharge machines together with local actuators has been proposed [32-34]. The conventional EDM machines have long positioning strokes but slow positioning response, the local actuators can realize wide-bandwidth and high positioning accuracy of the electrode in the orthogonal directions. During machining, the local actuators are used to realize the high-speed positioning of the electrode to maintain the suitable gap distance between the work-piece and the electrode.

However, the stroke of these actuators is limited to from several tens to several hundreds of micrometers and consequently they are unable to realize a neither high speed nor long stroke jump of the electrode in the axial direction to flush the dielectric fluid away from the work-piece. The necessity for flushing the dielectric fluid for removing the debris and stabilizing the electrical discharge condition during small deep hole-EDM processes is well known. The increased flushing is expected to increase the material removal rate, decrease tool wear rate and improve surface finish.

Related to the enhanced flushing, there have been many reports in the literatures that rotation of the electrode [35-38], orbital motion [39] and high speed jump motion [40, 41] of the electrode increased the machining speed and quality in small hole-EDM.

Furthermore, the use of tilt compensation of electrode in rotary EDM has not been conducted. This is considered to eliminate the tapper error of machined hole and to compensate a tilt clamping error of an electrode.

In order to realize high speed and highly precise positioning of the electrode, our group has developed a 5-DOF controlled maglev electrode driving actuator

(previous type) [42-44]. The actuator not only has a wide-bandwidth and high-accuracy in 5-DOF, but also has a stroke of 2mm in the axial direction to realize the rapid retraction of the electrode during EDM. Micro holes have been machined in multi-directions using the maglev actuator combined with a conventional electrical discharge machine (EA12E, Mitsubishi Electric Corp.), as shown in Fig. 2.1, and the machining speed was improved by 20~400%, compared with using the conventional EDM machine alone.

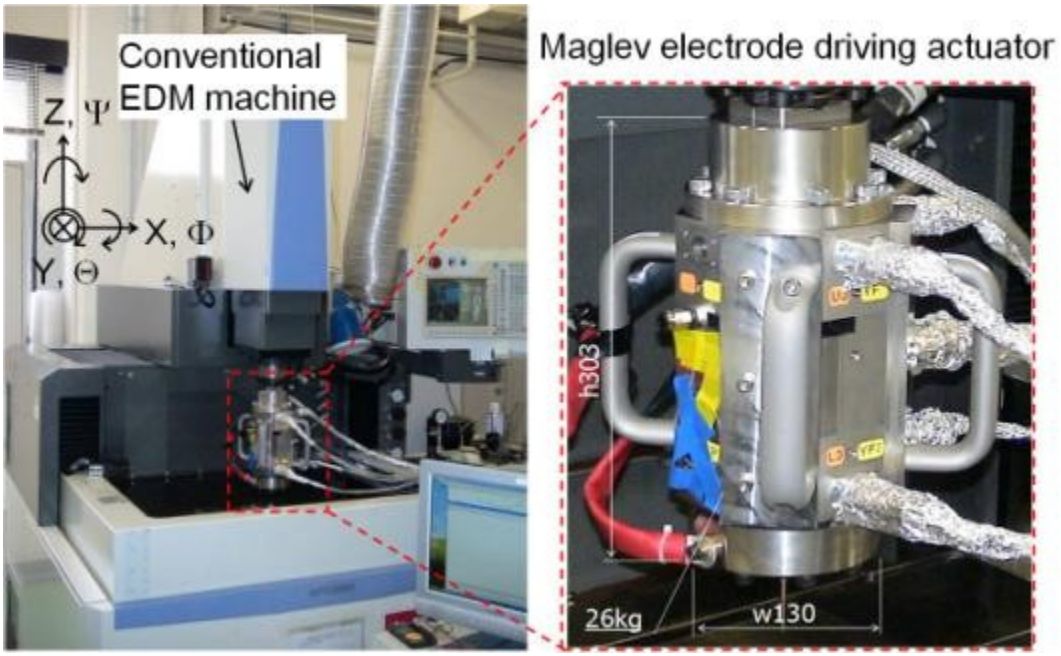

Fig. 2.1 Combination of conventional electrical discharge machine and maglev electrode driving actuator (previous type)

However, the previous type actuator has a height of 303mm without an electrode and its attachment, a width of 130mm and a weight of 26kg. And the brushes feeding the discharge voltage to the spindle shaft contact the levitated spindle shaft directly, so that the friction between the spindle shaft and the brushes disturbed the rotation of the spindle shaft, which made the actuator could not rotate the electrode.

The large size of the previous type electrode driving actuator decreases the machining area and the large mass makes it difficult for the conventional electrical discharge machine to drive and position the actuator with a high speed

and accuracy, and without the electrode rotation, debris cannot be removed efficiently when machining small-deep holes.

Therefore, for solving these problems, a new compact maglev electrode driving actuator with sufficient positioning response and positioning accuracy is designed and fabricated in this chapter. A new discharge voltage supply mechanism without disturbing the electrode levitation and rotation is proposed.

2.2 Principle and design of the maglev electrode driving actuator

2.2.1 Design specification

Considering the achieved performance of the previously developed maglev electrode driving actuator, the new maglev electrode driving actuator should enable an electrode to realize 0.2~2mm positioning stroke in three orthogonal directions and several mrad positioning stroke in two tilt directions, sub-micrometer and several micro radian positioning resolution, bandwidth greater than 100Hz [42]. In addition, the new actuator should be more compact and can rotate the electrode without disturbance from the discharge voltage feeding brushes.

Fig. 2.2 shows the configuration of the new maglev electrode driving actuator. The new actuator primarily consists of a 5-DOF controlled magnetic bearing (MB) system, a novel magnetic coupling mechanism and a spindle shaft. The 5-DOF controlled MB system consists of an upper radial MB, a lower radial MB and a thrust MB, which are used to levitate and position the spindle shaft precisely and speedily in three orthogonal (X-, Y- and Z-) and two tilt (Θ- and Φ-) directions.

2.2.2 Configuration of magnetic coupling mechanism

Fig. 2.3 shows a preciously developed discharge voltage supply mechanism in the precious developed maglev electrode driving actuator [42]. The power

supply brushes are in direct contact with the levitated spindle shaft, so the positioning and rotation of the spindle shaft are disturbed by the friction between the spindle shaft and the power supply brushes. To solve this problem, a novel discharge voltage supply method using a magnetic coupling mechanism is proposed.

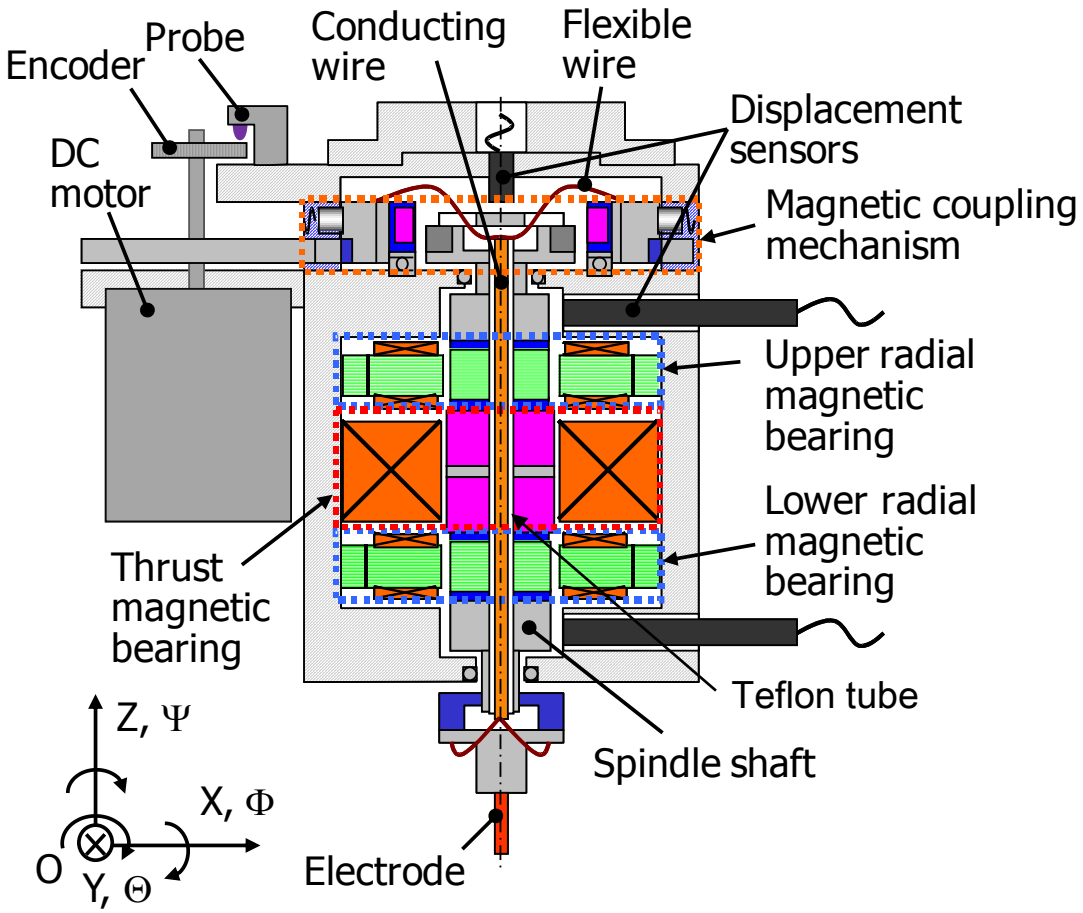

Fig. 2.2 Configuration of new maglev electrode driving actuator

Fig. 2.4 shows the configuration of the proposed magnetic coupling mechanism, which is designed to feed the discharge voltage to the electrode and to transmit a torque from the motor to the spindle shaft. The main components comprise of a power supply brush, a power supply ring, a ball bearing, a magnetic coupling, a levitated spindle shaft, a conductive flexible wire, spur gears and a motor.

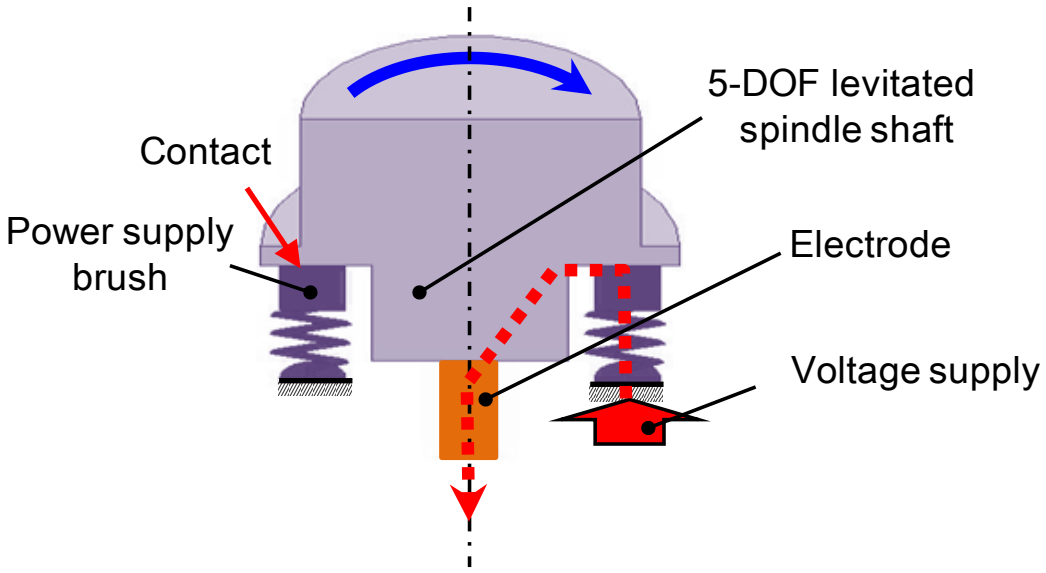

Fig. 2.3 Conventional discharge voltage supply mechanism

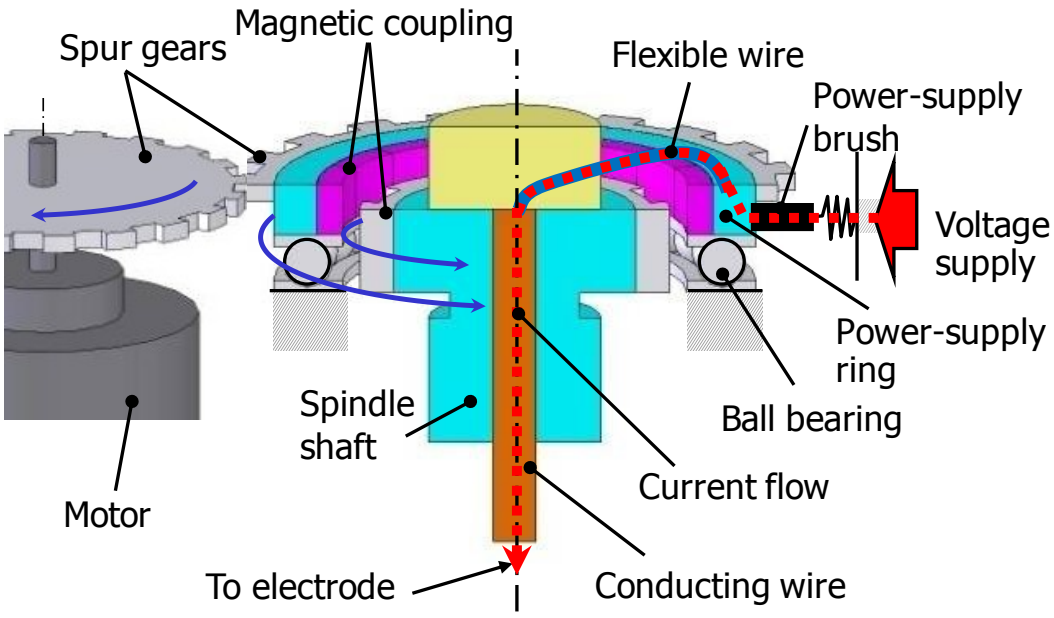

Fig. 2.4 Configuration of the magnetic coupling mechanism

The power supply ring contacting with the power supply brush is arranged on the outer circumference of the spindle shaft, and it is supported by the ball bearing. The conductive flexible wire connects the power supply ring to the conducting wire attached to the levitated spindle shaft, so that the spindle shaft is

free from direct contact with the power supply brush.

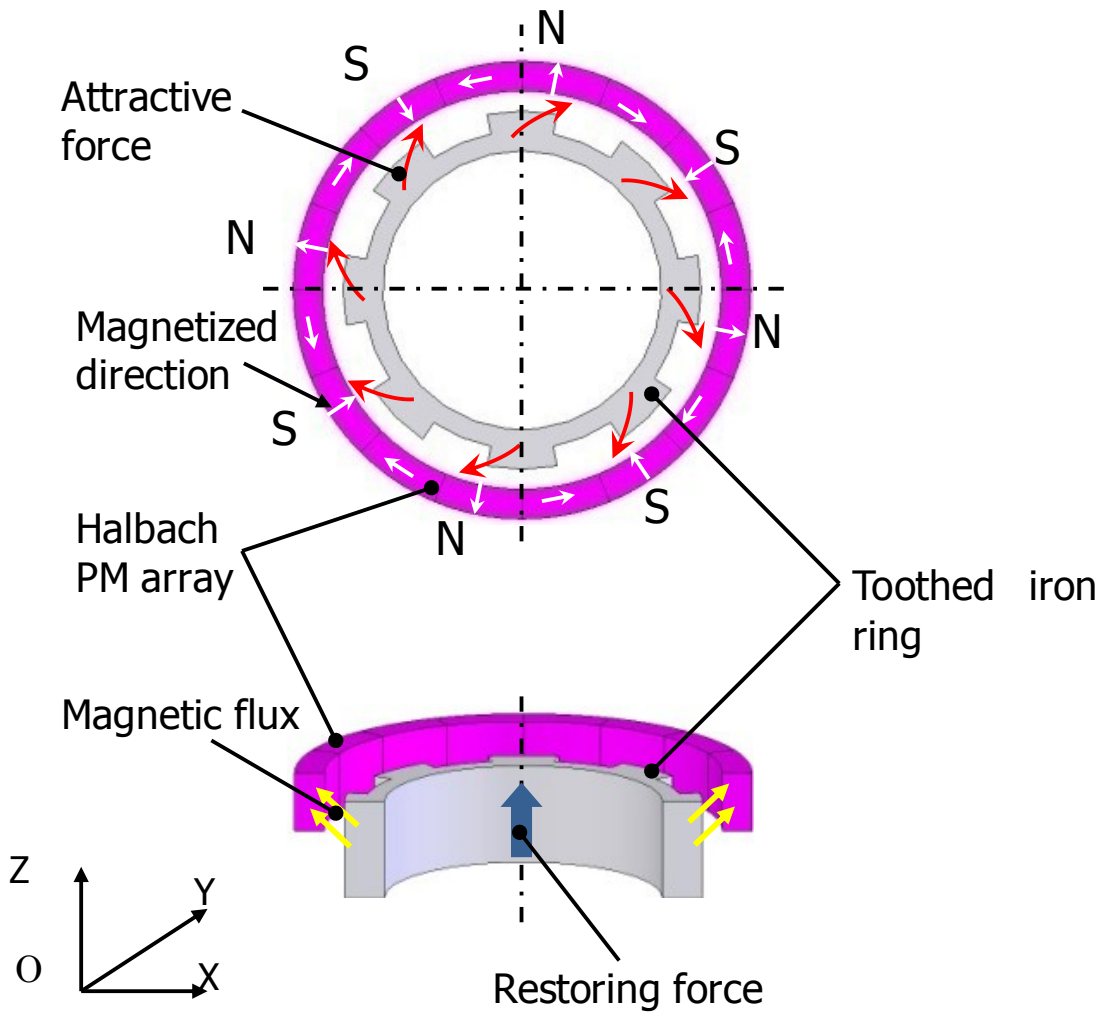

Fig. 2.5 Configuration of the designed magnetic coupling

The magnetic coupling includes of a permanent magnet (PM) ring comprising a Halbach PM array, and a toothed iron ring, as shown in Fig. 2.5. The Halbach PM array is located in the power supply ring, while the iron ring is located in the spindle shaft.

Using the attractive force between the outer Halbach PM array and the inner toothed iron ring, as shown in Fig. 2.5, the torque generated by the motor can be transmitted from the power supply ring to the levitated spindle shaft. Therefore, the spindle shaft can be rotated in synchronism with the rotation of the power

supply ring, and the flexible wire between the power supply ring and the spindle shaft can feed the discharge voltage to the electrode for EDM, without any adverse effect caused by friction from the power supply brush or any entanglement of the flexible wire. Furthermore, to avoid the 'out-of-step' between the spindle shaft and the power supply ring, the acceleration and deceleration of rotational speed should be limited. The power supply ring is rotated by the motor via a pair of spur gears.

The magnetic coupling has a positive stiffness characteristic in the thrust direction. As the toothed iron ring is moved downward in the thrust direction related to the Halbach PM array, an axial upward restoring force is generated, as shown in Fig. 2.5. Therefore, the magnetic coupling also can balance the effects of gravity on the spindle shaft, reducing power consumption of the thrust magnetic bearing.

2.2.3 Design objective of magnetic coupling

For the design of the magnetic coupling, it is necessary to consider the transmission torque and the axial restoring force. Firstly, to avoid 'out-of-step' effects of the magnetic coupling, it is desirable to generate a large transmission torque with a small relative angle between the PM ring and the magnetic ring. The 'out-of-step' effect occurs due to inertial torque during acceleration and deceleration of the spindle rotation, and due to eddy-current-torque at high rotational speeds.

Secondly, since the transmission torque can be reduced by sinkage of the magnetic ring below the Halbach PM array, it is also desirable to generate a large restoring force to minimize sinkage. However, a small change in the restoring force is expected to be generated when the spindle shaft is moved in the thrust direction.

The desired specifications for the magnetic coupling can be defined as follows. The permitted sinkage is set to 2mm or less to reduce the influence of

sinkage on the transmission torque. The restoring force is set to 4.9N, assuming that the mass of the spindle shaft is 0.5kg. The desired change in the restoring force is set to be less than 10% of the electromagnetic force of 55N, the maximum generated by the thrust magnetic bearing, assuming that the maximum displacement of the spindle shaft in the thrust direction is ±1mm during EDM. Moreover, the desired transmission torque is set to 7.6×10^{-2}Nm at a sinkage of 2mm based on the eddy current torque measured in the other magnetic bearing [45], assuming the maximum rotational speed of the spindle is 5,000rpm.

Considering the maintenance performance and control stability, the magnetic coupling mechanism is attached to the upper end of the MLA, as shown in Fig. 2.2. Firstly, if this mechanism was attached to the middle of the actuator, the replacement of the flexible wire would be troublesome if the wire was to break.

Secondly, if it was attached to the lower end of the actuator, then motion control of the electrode would become difficult, because it would be hard to measure the true vibration of the electrode due to the increase in the distance between the displacement sensors and the electrode.

2.2.4 Designed magnetic coupling

A magnetic coupling is designed based on numerical analysis using a static magnetic field simulation, as shown in Fig. 2.6. The Halbach PM array of the magnetic coupling consists of eight radially-magnetized and eight circumferentially-magnetized PMs. The magnetic ring, which has eight teeth, is made of electromagnetic soft iron. The geometrical dimensions of the coupling are also detailed in Fig. 2.6.

Fig. 2.7 shows the simulated relationship between the sinkage of the magnetic ring and the restoring force. At a sinkage Δh = 2mm, the restoring force is 6.7N. Thus, the weight of the spindle shaft can be balanced when the sinkage is less than the designed value of 2mm. Furthermore, when the spindle shaft is

moved by ±1mm in the thrust direction, based on the initial sinkage position of *Δh* = 2mm, the change in the restoring force is about ±3N, which is also less than 10% of the maximum force generated by the thrust magnetic bearing.

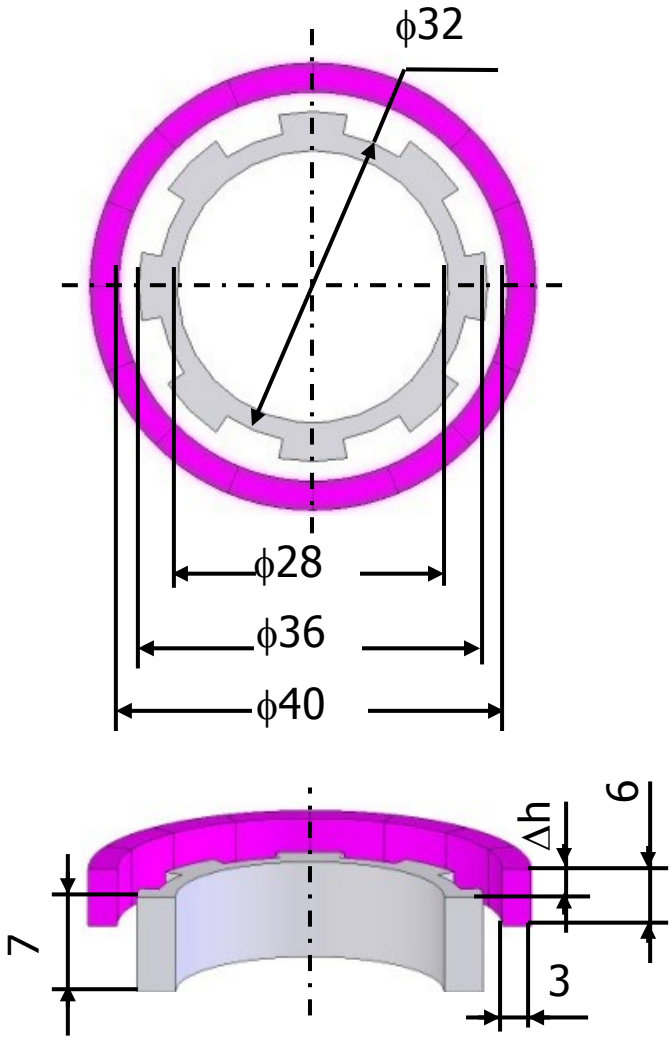

Figure 2.6 Dimensions of the designed magnetic coupling

Moreover, the relationship between the relative angle and the magnetic coupling torque is calculated at a sinkage *Δh* = 2mm by using FEM (Finite element method) software (Ansoft Maxwell 3D, Ver.10.0). At a relative angle of 10.5°, a maximum torque of 8.1×10^{-2}Nm can be statically transmitted, and when sinkage *Δh* = 1mm, maximum torque of 9.3×10^{-2}Nm can be statically transmitted at the relative angle of 11°, which are both more than the desired value of 7.6×10^{-2}Nm.

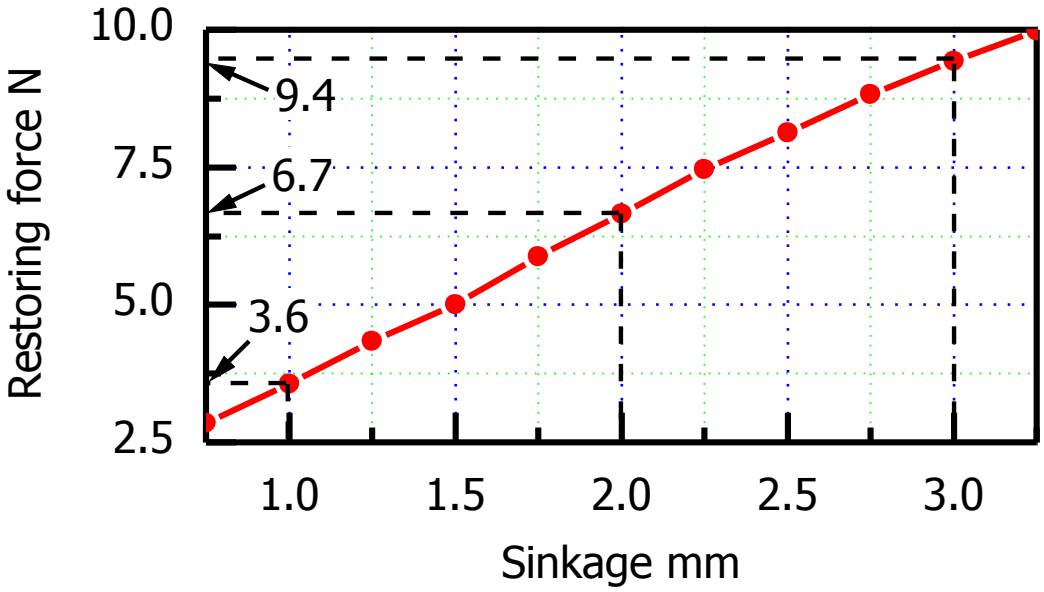

Fig. 2.7 Relationship between the sinkage of the magnetic ring and the restoring force (simulation)

2.2.5 Design of thrust positioning actuator

During EDM of micro-holes with a high aspect ratio, a voice-coil-motor type of thrust magnetic bearing is used to realize positioning strokes of a few millimeters for the rapid retraction of the electrode in the Z direction. Fig. 2.8 shows both the previous-type and new-type thrust magnetic bearings. The previous thrust magnetic bearing comprised of two air-core coils located in the stator and a cylindrical PM located in the spindle shaft [42], while the new-type thrust magnetic bearing consists of an air-core coil and a pair of oppositely magnetized cylindrical permanent magnets (PMs) sandwiching a ring made of pure iron. The new-type is shorter in the axial direction in comparison to the previous design because the coils are not separated, which improves the compactness of the maglev actuator. When current is supplied to the coil as shown in Fig. 2.8, a corresponding upward Lorentz force would be generated to the spindle shaft.

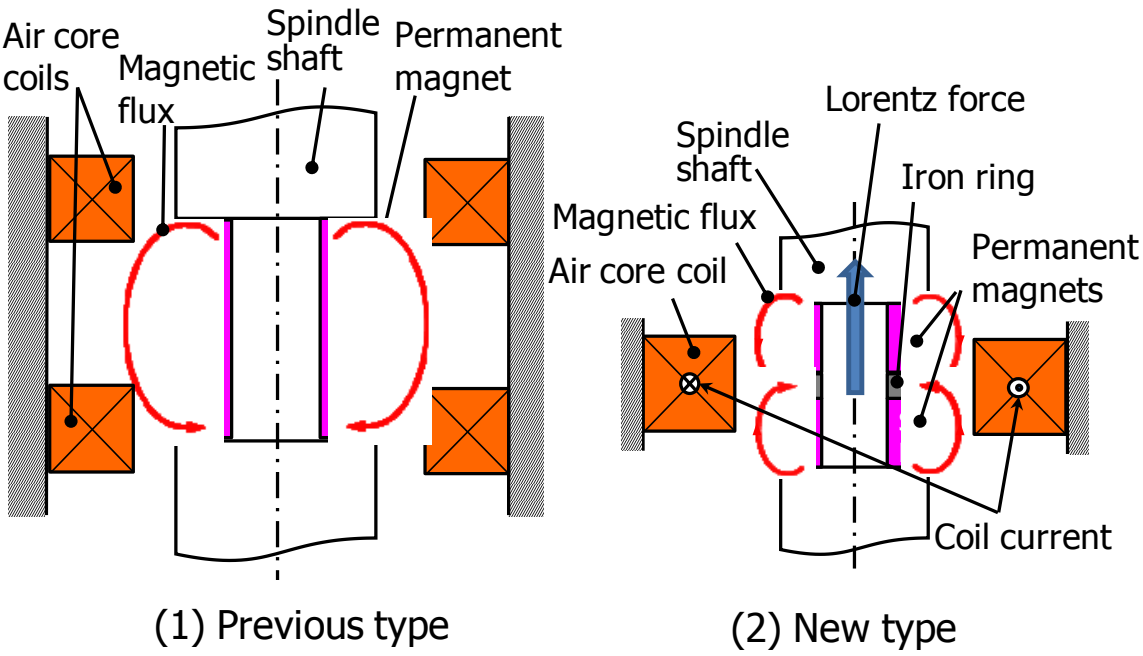

Fig. 2.8 Principle of thrust magnetic bearing

The two oppositely magnetized PMs generate very strong repulsive force to each other, which makes the assembly become difficult. A sandwiched iron ring between the PMs generates attractive force to the PMs, in order to cancel the repulsive force between the PMs (i.e. to avoid magnetic saturation of the iron ring), the thickness of the iron ring should be at least 3mm. Moreover, the iron ring can concentrate the magnetic flux in the air-core coil, thus, the driving force can be increased. Under the premise of avoiding magnetic saturation of iron ring, the smaller of the iron ring thickness is the better effectiveness of magnetic flux concentration and the more compact size of the thrust magnetic bearing becomes. Therefore, the thickness of the iron ring was set to be 3mm.

2.3 Fabricated maglev electrode driving actuator

2.3.1 Prototype maglev electrode driving actuator

Fig. 2.9 shows a prototype and its spindle shaft (excluding the magnetic ring for the magnetic coupling and a thrust sensor target). Compared to the previous actuator, the height of the new prototype maglev electrode driving actuator

(excluding an electrode holder) was decreased from 303mm to 159mm, the width was decreased from 130mm to 100mm, and the mass was decreased from 30kg to 10kg. The length of the spindle shaft, as shown in Fig. 2.9, was 123mm, its maximum diameter was 28mm, and its mass without all the attachments was 0.35kg.

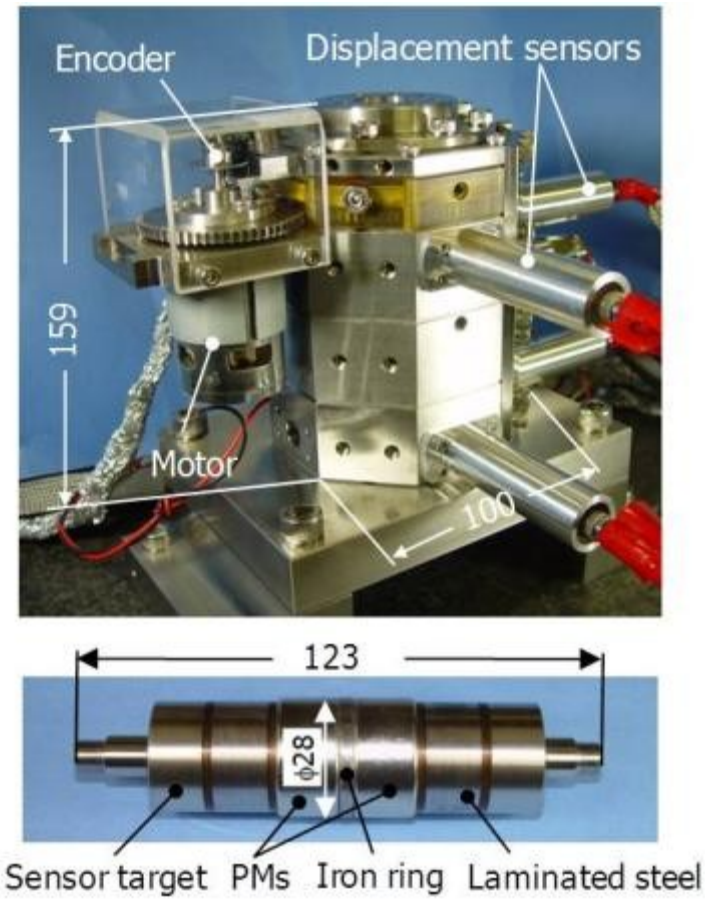

Fig. 2.9 Fabricated prototype maglev electrode driving actuator and its spindle shaft

The displacement of the spindle shaft in the thrust direction was measured using an eddy-current displacement sensor (PU-05, AEC Corp., measurement range ±1.0mm, resolution 0.5μm), and the displacements in the radial directions were measured using four capacitive displacement sensors (MicroSense 5502, ADE Corp., measurement range ±0.1mm, resolution 20nm, cut-off frequency 5kHz).

The power supply ring was driven by a DC motor (RS-755WC-8017,

Mabuchi motor Corp.) and gears (Gear ratio 1:1.5), while the rotational speed of the spindle shaft was measured by an encoder (MG-20-1200, Microtech Laboratory Inc, resolution 1200ppr). The actuator was controlled via a digital signal processor (DS1005, dSPACE Corp.) with a sampling rate of 10 kHz.

2.3.2 Control system

Modeling and model identification:

In this research, according to experience in developing the previous type maglev electrode driving actuator, some assumptions are made for simplifying the control system:

1) No interference is generated between the motions of radial, tilt and thrust directions;
2) The back electro-motion force is ignored;
3) The gyro effect is not taken into consider.

Based on these assumptions, the motion of the rotor in the X direction can be described as Eq. (2.1), the motions in the Y, Z, Θ and Φ directions (which are not shown) are almost the same as that in the X direction.

The electromagnet is driven by bias current using push-pull method, after linearization, the generated driving force of the electromagnet in the X direction can be calculated by Eq. (2.2), and Eq. (2.3) deriving the relationship between the voltage and current of the electromagnet coil.

$$m\ddot{x} + c_x\dot{x} - k_x x = f_x \quad \text{.....(2.1)}$$

$$f_x = k_{ix} i_x \quad \text{.....(2.2)}$$

$$v_x = R_x i_x + L_x \dot{i}_x \quad \text{.....(2.3)}$$

Here,

m : the mass of rotor

x : displacement in the X direction

c_x : damping coefficient in the X direction

k_x : stiffness in the X direction

f_x : electromagnetic driving force in the X direction

k_{ix} : the current-force coefficient in the X direction

i_x : current of electromagnet coil in the X direction

v_x : voltage of electromagnet coil in the X direction

R_x : resistance of electromagnet coil in the X direction

L_x : inductance of electromagnet coil in the X direction

Via Laplace transfer, the equations can be written as:

$$X(s)=\frac{1}{ms^2+c_x s-k_x}F_x(s) \quad \text{(2.4)}$$

$$F_x(s)=k_{ix}I_x(s) \quad \text{(2.5)}$$

$$I_x(s)=\frac{1}{L_x s+R_x}V_x(s) \quad \text{(2.6)}$$

Fig. 2.10 shows the control system of the actuator in the X-direction; the control systems in the Y-, Z-, Θ- and Φ-directions (which are not shown) are almost the same as that in the X direction. In the control system, a positioning controller, which was composed of an integrator compensator and a regulator, consisting of a 2nd order numerator and 2nd order denominator, was used. To improve the response speed of the electromagnetic force for the magnetic bearings, a local current feedback loop using PI compensators and lead/lag controllers were also added.

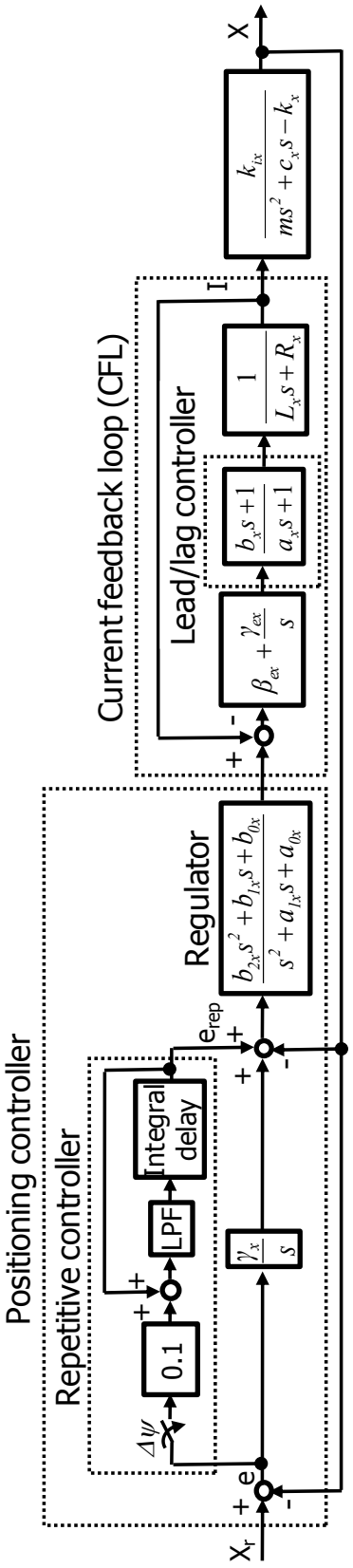

Fig. 2.10 Control system in the X-direction

Moreover, a space-domain repetitive controller comprising of a low-pass-filter (LPF) and an integral delay element was used in order to suppress the vibrations caused by the unbalance force of the spindle shaft and the unbalance magnetic pull of the magnetic bearings whilst the spindle shaft is rotating [46]. However, the motion in the thrust direction suffers very little interference from radial vibrations according to the experimental results, so no repetitive controller was added to the control system in the Z direction.

The control parameters in the X-, Θ- and Z-directions, as shown in Table 2.1, were set through trial and error using simulation and experiments, and Table 2.2 shows the model parameters in the X-, Θ- and Z-directions. Here, the inductance and resistance of the coil L and R, and the mass of the spindle shaft m were measured directly. The damping c, stiffness k and current-force coefficient k_i of the magnetic bearing were identified using the measured frequency responses of the maglev electrode driving actuator.

Table 2.1 Controller parameters in the X-, Θ- and Z-directions

X – direction		Θ – direction		Z – direction	
γ_x	1.9×10^{2}	γ_θ	2.1×10^{2}	γ_z	4.2×10^{2}
a_{1x}	7.8×10^{3}	$a_{1\theta}$	5.9×10^{3}	a_{1z}	4.3×10^{3}
a_{0x}	2.6×10^{7}	$a_{0\theta}$	1.5×10^{7}	a_{0z}	9.1×10^{6}
b_{2x}	1.3×10^{5}	$b_{2\theta}$	4.7×10^{3}	b_{2z}	5.2×10^{4}
b_{1x}	4.3×10^{8}	$b_{1\theta}$	1.3×10^{7}	b_{1z}	2.3×10^{8}
b_{0x}	3.1×10^{11}	$b_{0\theta}$	6.8×10^{9}	b_{0z}	1.1×10^{11}
γ_{ex}	15.0	$\gamma_{e\theta}$	15.0	γ_{ez}	25.0
β_{ex}	1.0×10^{3}	$\beta_{e\theta}$	1.0×10^{3}	β_{ez}	1.0×10^{3}
a_x	5.0×10^{-4}	a_θ	5.0×10^{-4}	a_z	4.2×10^{-4}
b_x	6.9×10^{-4}	b_θ	6.9×10^{-4}	b_z	8.8×10^{-4}

In the repetitive controller as shown in Fig. 2.10, parameter e is defined as the deviation of the spindle reference in the X-direction and ψ is the rotational angle of the spindle shaft. In the space domain repetitive controller, $\Delta\psi$ is the sampling angle of the spindle rotation. Moreover, the parameter values in the Y-

and Φ-directions, which are not shown in the tables, are almost the same as those in the X- and Θ-directions [47].

Table 2.2 Identified model parameters in the X-, Θ- and Z-directions

X – direction			Θ – direction			Z – direction		
L_x	7.6×10^{-3}	H	L_θ	7.6×10^{-3}	H	L_z	5.0×10^{-2}	H
R_x	0.63	Ω	R_θ	0.63	Ω	R_z	8.0	Ω
m	0.45	kg	J_θ	9×10^{-4}	Kg. m^2	m	0.45	kg
c_x	5.0	N/(m/s)	c_θ	0	N.m/(rad/s)	c_z	1.0	N/(m/s)
k_{ix}	18.0	N/A	$k_{i\theta}$	18.0	N.m/A	k_{iz}	15.0	N/A
k_x	5.0×10^{5}	N/m	k_θ	3.9×10^{-2}	N.m/rad	k_z	9.6×10^{-2}	N/m

2.4 Experimental performance of the maglev electrode driving actuator

2.4.1 Positioning performance

The positioning performance of the actuator was evaluated at a rotational speed of 0rpm. The positioning resolutions and the frequency response characteristics were measured by using a digital signal processor and a frequency response analyzer (FRA 5095, NF Corp.).

Fig. 2.11 and Fig. 2.12 show the experimental results for the positioning resolutions and frequency responses in the X-, Y-, Θ-, Φ- and Z-directions. The positioning resolution and bandwidth of the prototype maglev electrode actuator were 0.3μm and 215Hz in the X-direction, 0.5μm and 202Hz in the Y-direction, 5μrad and 225Hz in the Θ-direction; 5μrad and 212Hz in the Θ-direction and 0.5μm and 255Hz in the Z-direction, respectively. The actuator possessed sub-micron and several micro-radians positioning resolution, and bandwidths greater than 200 Hz in the 5-DOF directions.

The positioning resolutions in the radial directions were not sufficiently good compared with those of the displacement sensors. Fig. 2.13 shows the experimental output of the capacitive displacement sensor when the spindle

shaft is not levitating. We found that the output of the capacitive displacement sensor has a variation of 0.1μm which is larger than the resolution of the sensor—20nm.

As the spindle shaft was not levitating at this time, and the variation of the sensor output has the same magnitude with the experimental positioning resolutions in radial directions, so we think the insufficient good resolution of the spindle shaft is mainly caused by environment noise. The positioning resolution in the Z-direction was the same as the resolution of the displacement sensor.

Fig. 2.14 shows that the actuator enabled the spindle shaft to have a full stroke of 2mm in the Z-direction for the rapid retraction of the electrode, which is helpful for removing debris during the EDM process. Fig. 2.15 demonstrates the rapid retraction of the electrode in the thrust direction. The actuator could realize a maximum speed of about 40mm/s with a retraction stroke of 0.91mm.

Fig. 2.16 shows that the actuator had a full stroke of 180μm in the X- and Y-directions and 3.6mrad in the Θ- and Φ-directions at 1Hz, respectively. These motions enable attitude compensation of the electrode during EDM.

Fig. 2.17 shows the orbital trajectory of the spindle shaft in the X-Y plane and the Θ–Φ plane at high frequencies of 100, 200 and 300Hz. The reference amplitude was set to 30 μm in the X-Y and 0.5mrad in the Θ–Φ planes, respectively.

The prototype actuator achieved these orbital motions at a few hundred Hz in the X-Y plane and the Θ–Φ plane. However, the measured amplitudes were smaller than the reference values, caused by the gain attenuation of the frequency characteristics as shown in Fig. 2.12.

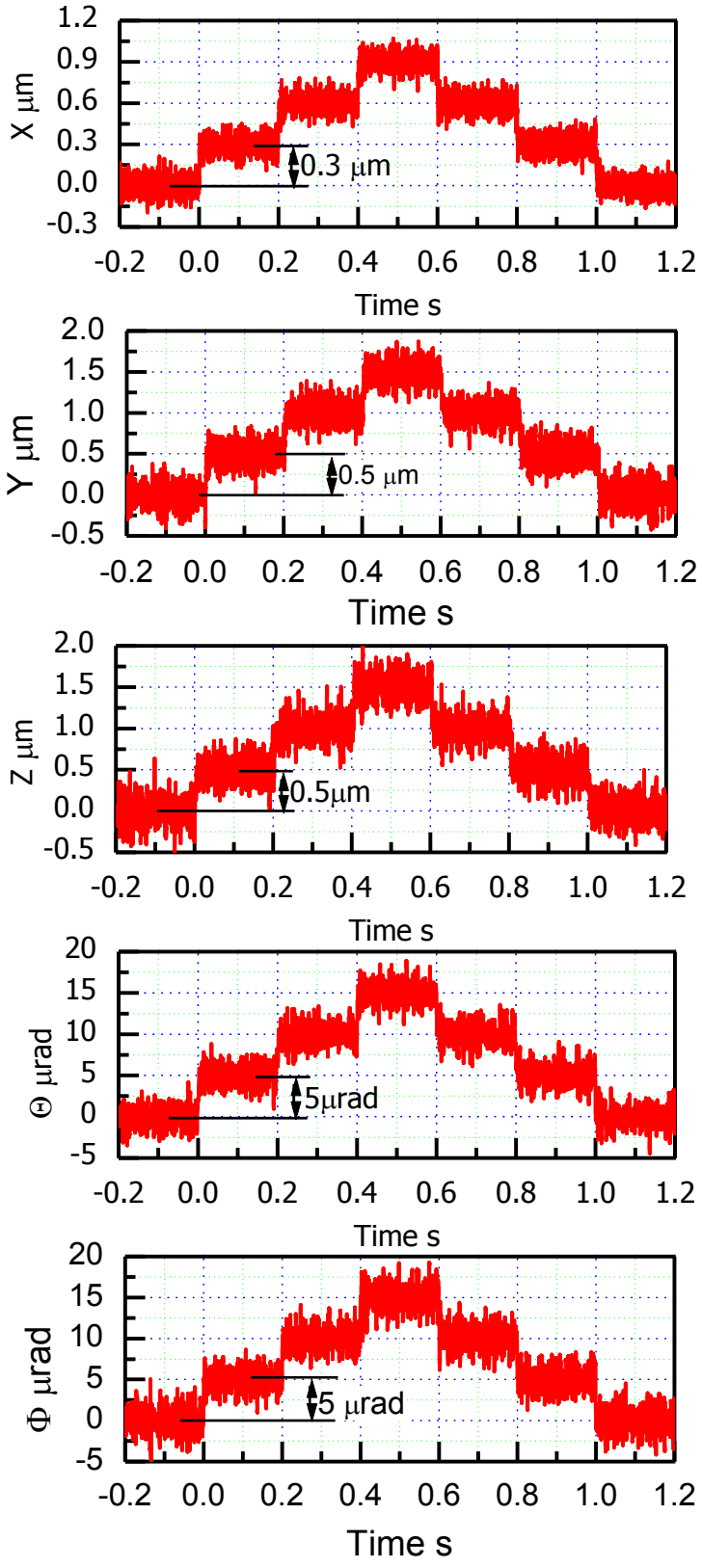

Fig. 2.11 Positioning resolution

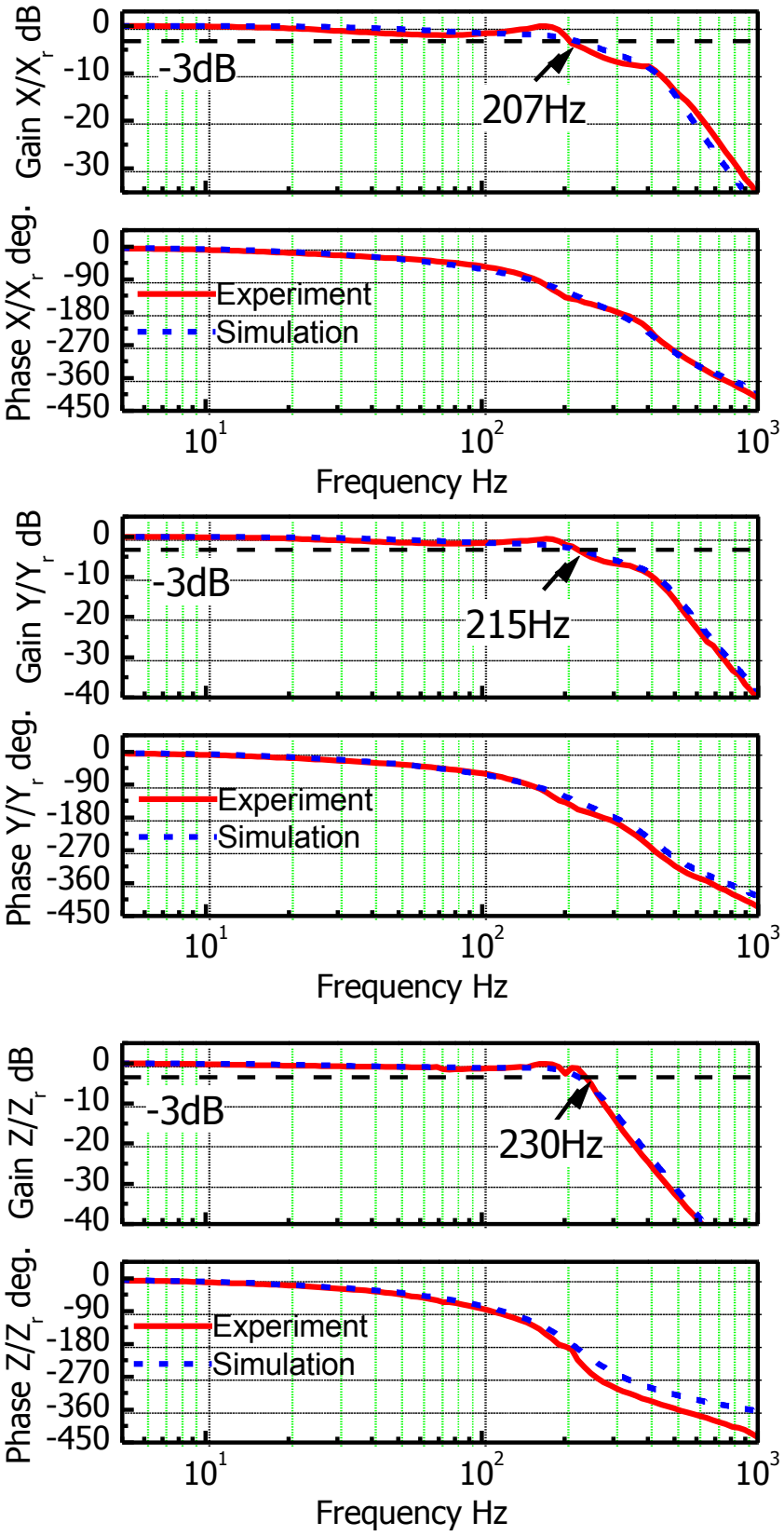

Fig. 2.12 Frequency response (1)

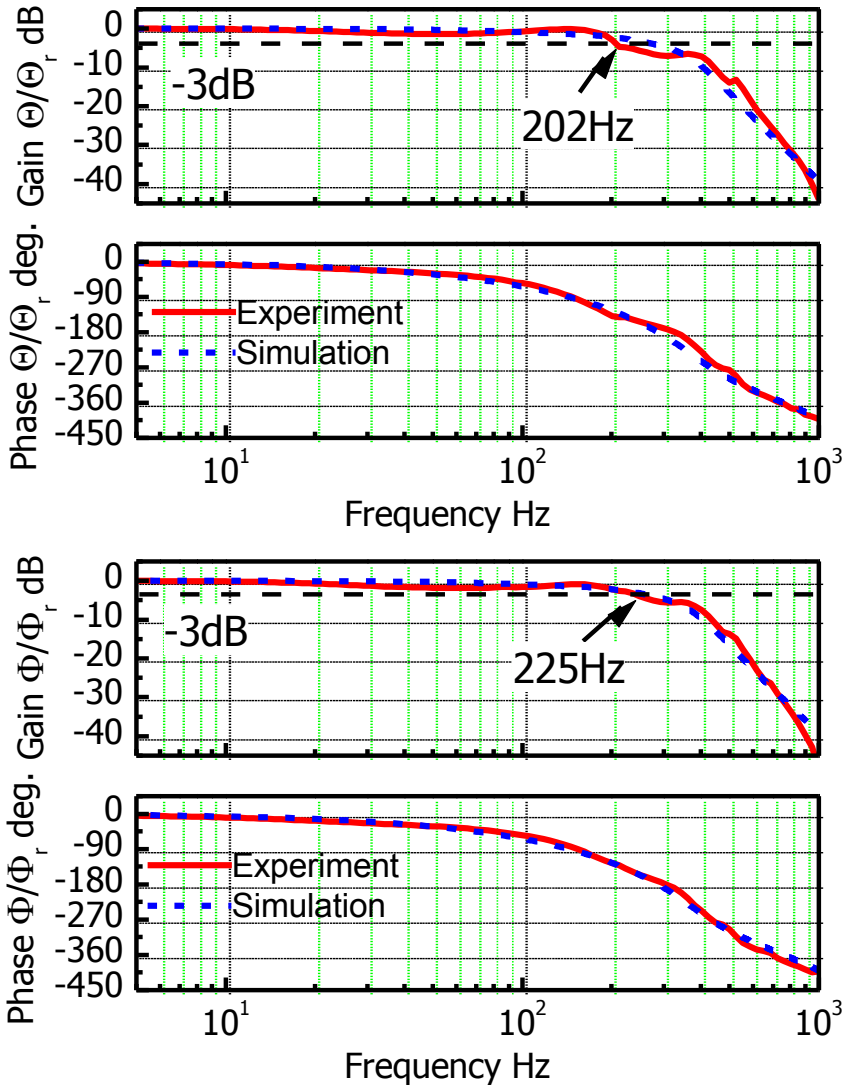

Fig. 2.12 Frequency response (2)

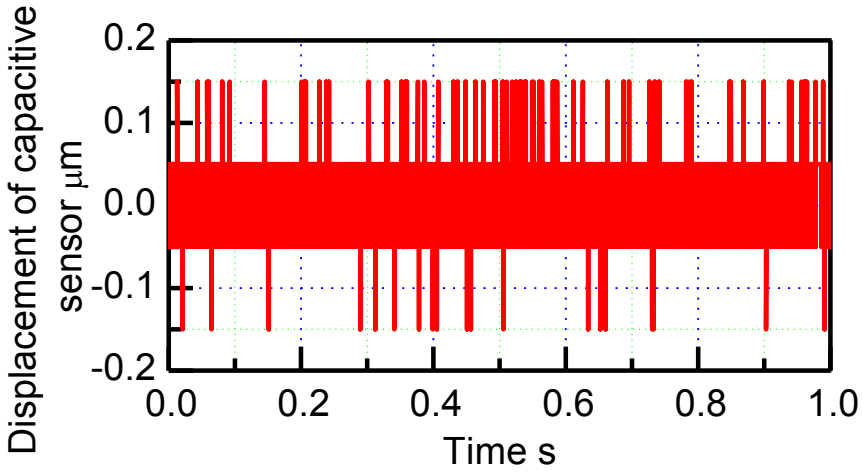

Fig. 2.13 Output of capacitive displacement sensor

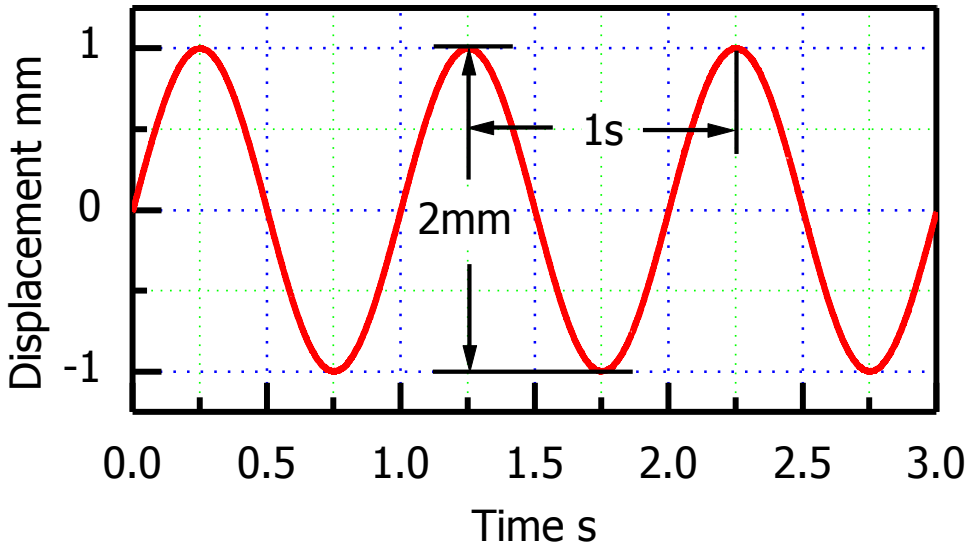

Fig. 2.14 Full stroke in the Z-direction

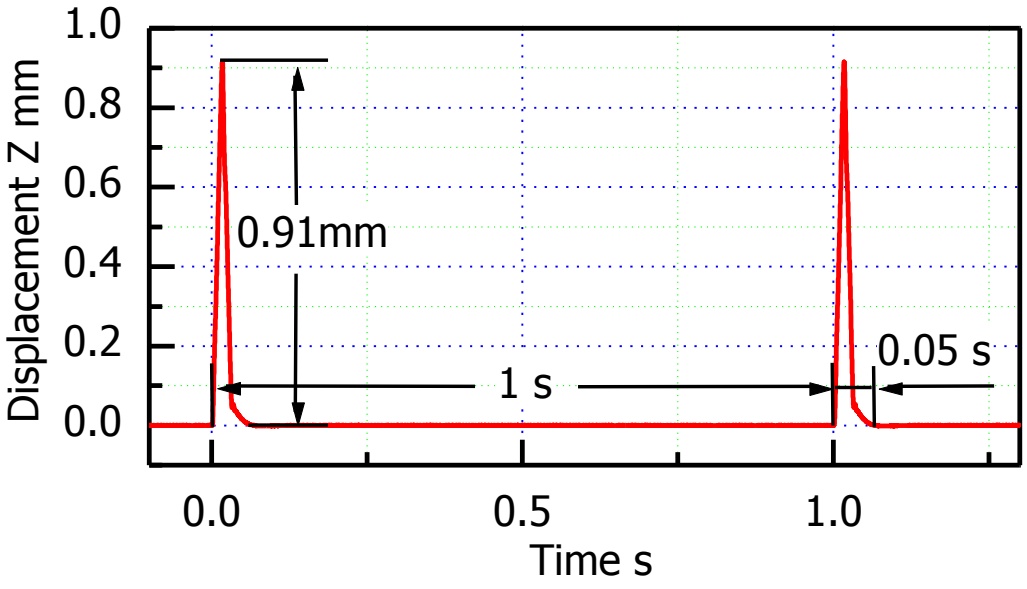

Fig. 2.15 Jump motion of the spindle shaft

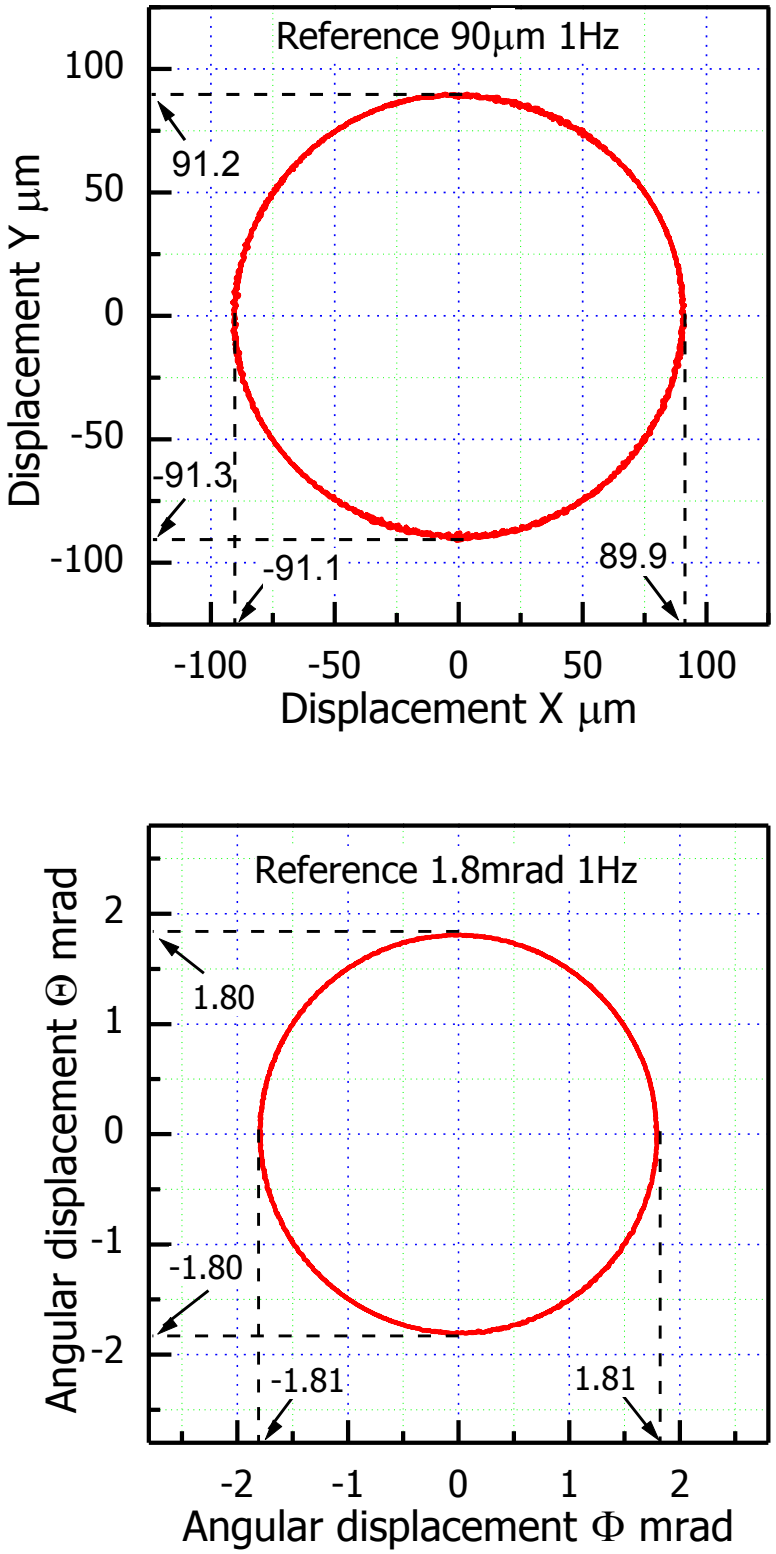

Fig. 2.16 Full strokes in the radial and tilt directions

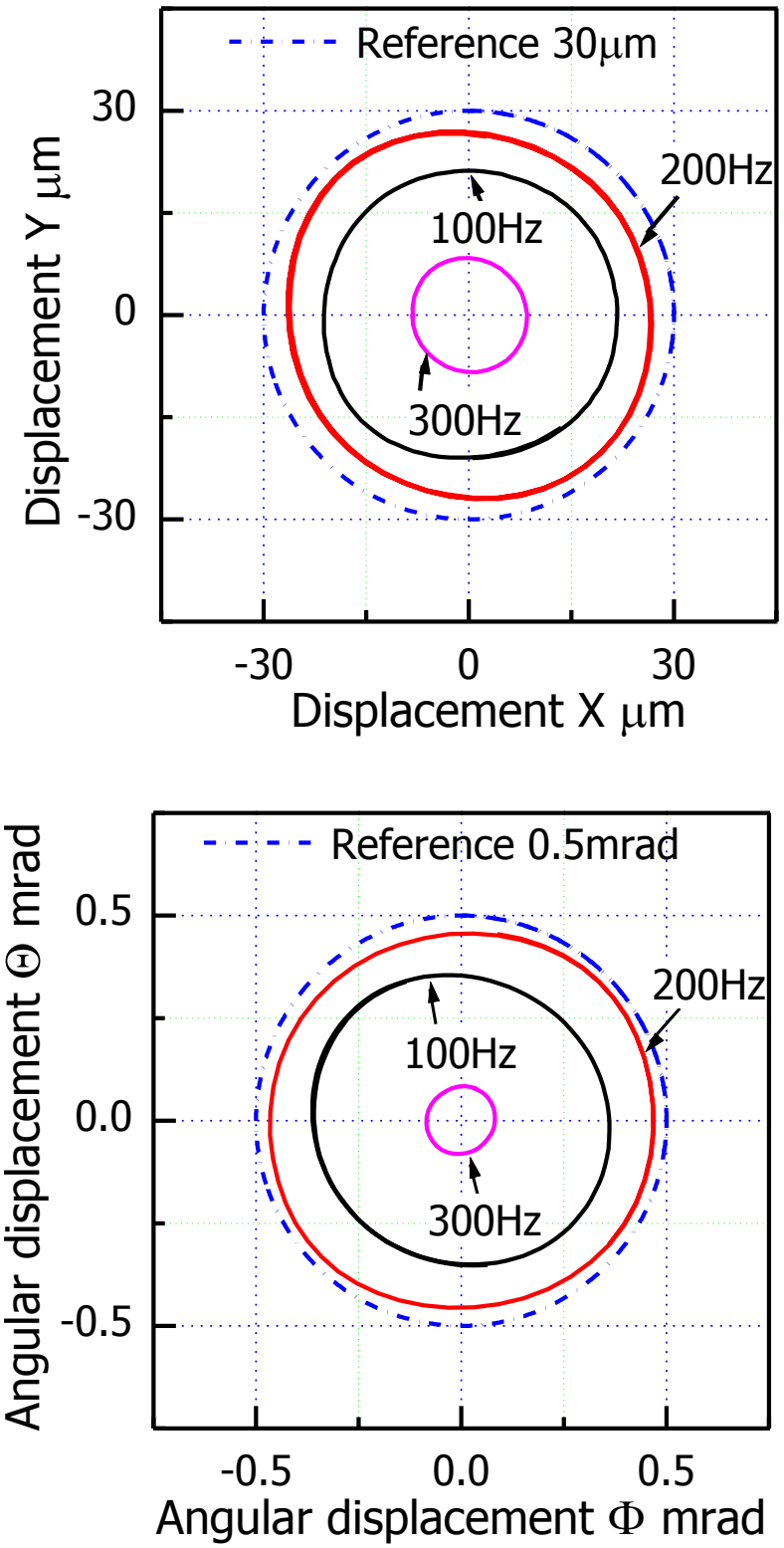

Fig. 2.17 Trajectory of the spindle shaft

2.4.2 Transmission torque of magnetic coupling mechanism

The transmission torque of the magnetic coupling mechanism was measured experimentally. In this experiment, the magnetic ring attached to the spindle shaft was fixed and the current applied to the motor was gradually increased, to rotate the PM ring attached to the power supply ring. The relative angle between the PM ring and the magnetic ring was measured by a rotary encoder, which was installed on the motor axis. The transmission torque of the magnetic coupling mechanism was calculated from the measured motor current and the torque-current coefficient of the motor.

Fig 2.18 shows the relationship between the relative angle between the PM ring and the magnetic ring and the transmission torque. When the torque was less than 0.07Nm, the relative angle did not change, and its value was almost zero. It is believed that the motor torque of 0.07Nm was balanced by the static friction induced by the power supply brush and the gearing. On the other hand, when the torque was more than 0.17Nm, the magnetic coupling was out-of-step.

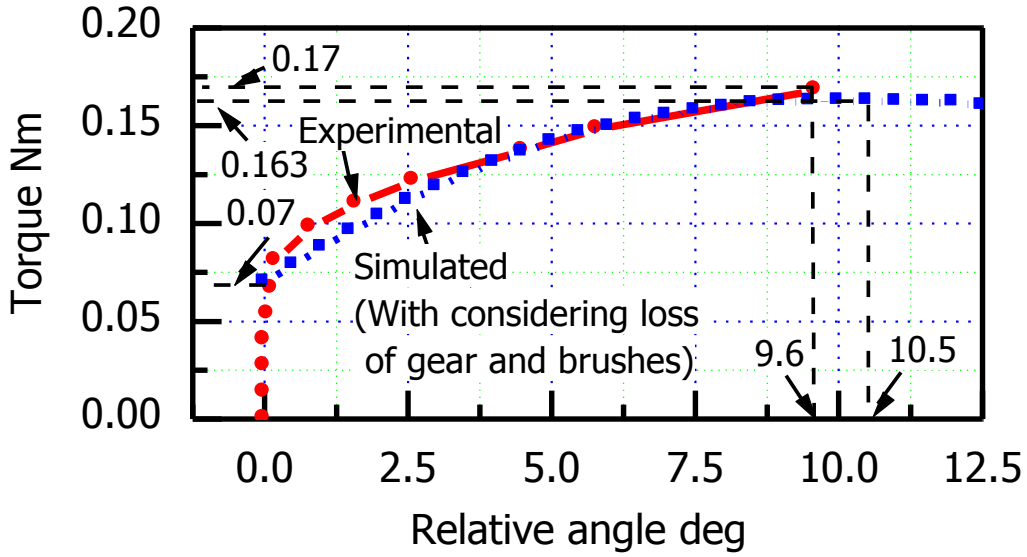

Fig.2.18 Relationship between the relative angle and the transmission torque

The experimental results indicated that the maximum transmission torque, neglecting the effect of friction, was 0.1Nm and the relative angle was 9.6° with

this system. Comparing the experimental result with the simulation, and considering the friction of the brush and the gear, it can be seen that the measured transmission torque was almost the same as the simulated value.

2.4.3 Rotational accuracy of the spindle shaft

The spindle shaft supported by the 5-DOF controlled magnetic bearing was rotated following rotation of the power supply ring via the magnetic coupling. Fig. 2.19 shows the peak-to-peak vibration amplitudes of the spindle shaft in the X-, Y-, Θ- and Φ-directions at 2,000 rpm. The results show that, at 2,000 rpm, the peak-to-peak vibration amplitudes of the spindle were significantly decreased from 7.1μm to 1.22μm and from 124μrad to 20.6μrad in the X- and Θ-directions, respectively, by the space-domain repetitive controllers.

Fig. 2.20 shows the peak-to-peak vibration amplitudes of the spindle shaft at various rotational speeds in the X- and Θ-directions. The experimental results in the Y- and Φ-directions, which are not shown, were almost the same as those in the X- and Θ-directions.

2.4.4 High speed multi-DOF motion of the spindle shaft

Fig 2.21 shows the spindle shaft possesses a multi-motion of rotation and orbital motion. In the experiment, the rotational speed ω_1 was 950 rpm and the orbital frequency ω_2 was 100Hz, the reference orbital radian r0 was set to 10μm, and the measure orbital radian became to about 7.5μm due to the gain attenuation at 100Hz, which coincided with the frequency characteristic of the prototype actuator as shown in Fig 2.12. Such a combination of high frequency orbital motion and rotation has never been implemented by neither conventional EDM machines nor local actuators.

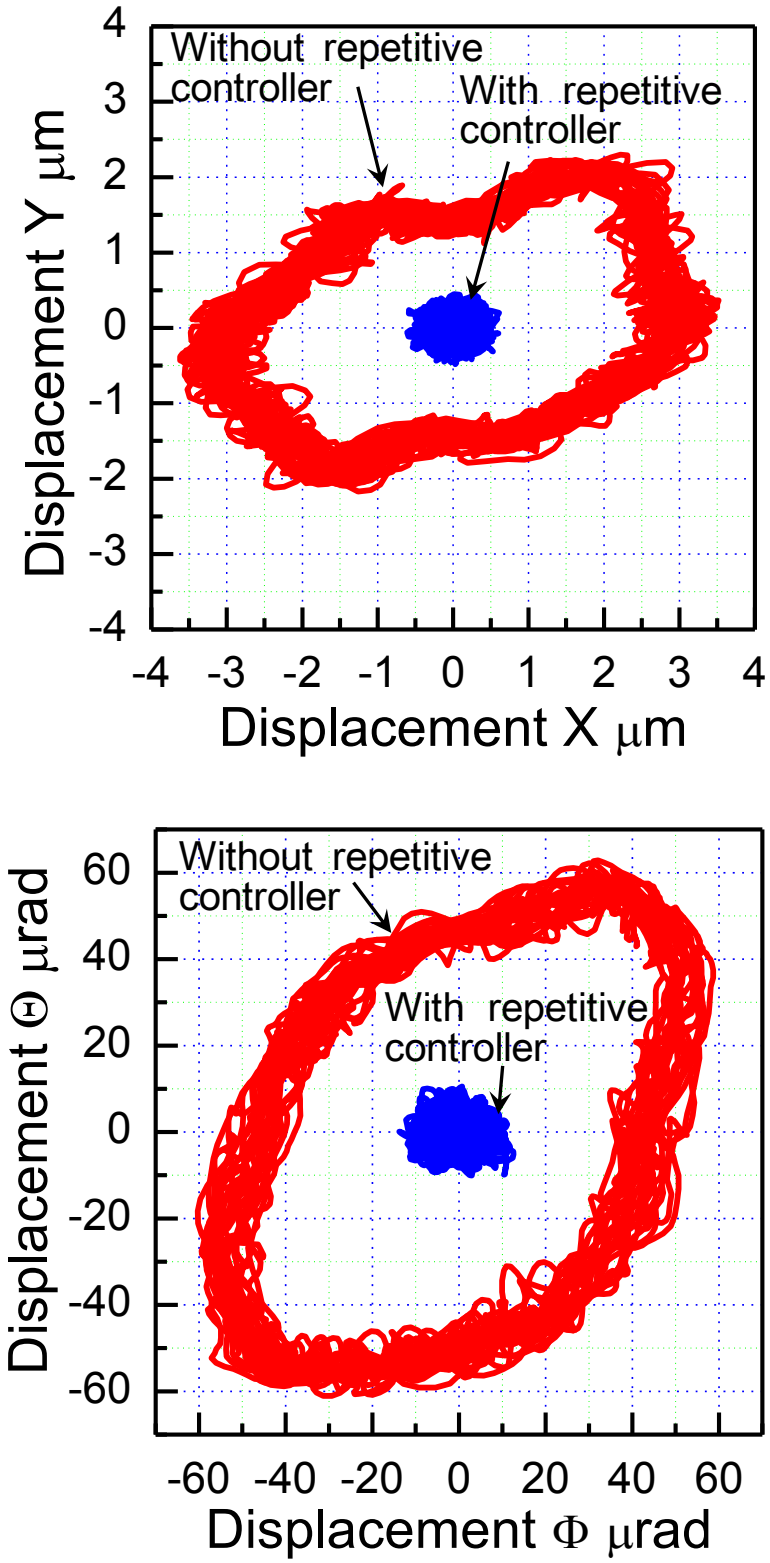

Fig. 2.19 Vibration of spindle shaft at 2000 rpm

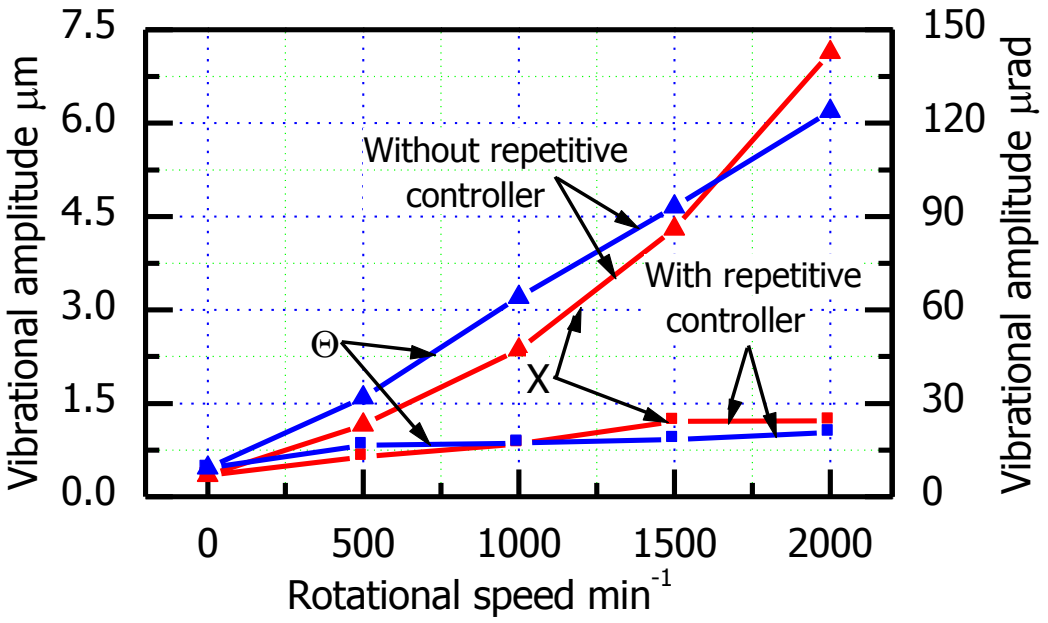

Fig. 2.20 Peak-to-peak rotational vibration of the spindle shaft at various rotational speeds

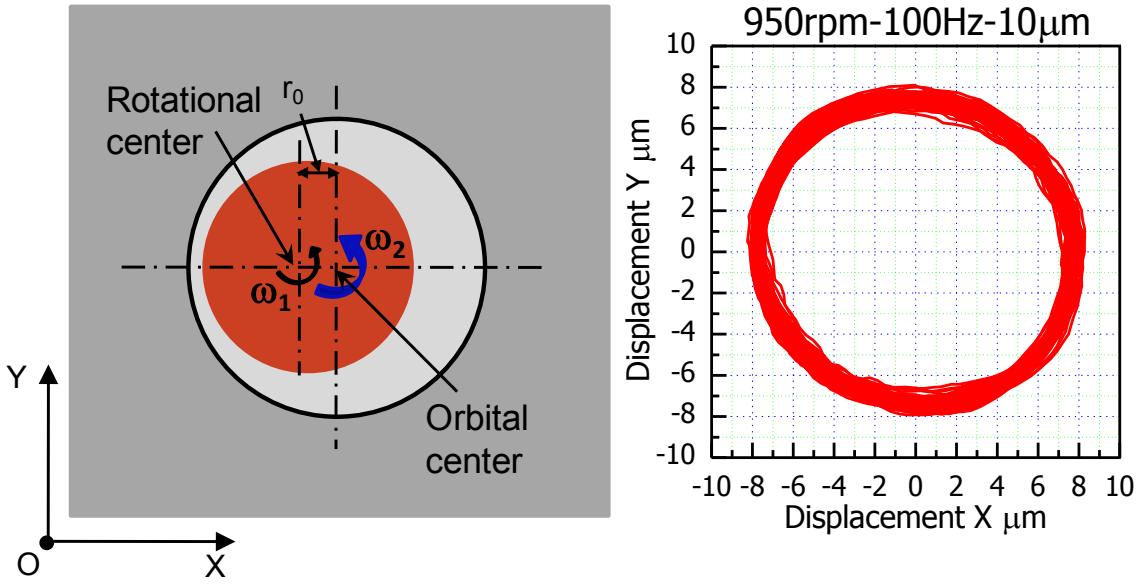

Fig. 2.21 Combination of rotation and orbital motion of spindle shaft

2.4.5 Gravity compensation of the spindle shaft

Fig 2.22 shows the dependence of the coil current on the thrust displacement. When the spindle shaft was positioned at 0.5mm in the Z direction, the measured average value of the coil current was 0A, under feedback control, which indicate that the restoring force balances the gravity of the spindle shaft. Then power consumption of the thrust magnetic bearing could be reduced. The current required for positioning the spindle shaft quasi-statically within the thrust stroke is less than 0.1A. Furthermore, there was a phase-reversal of the current when the spindle moved up by more than 0.4mm, which was caused by coupling effects between the radial magnetic bearing coils and the PMs attached on the spindle.

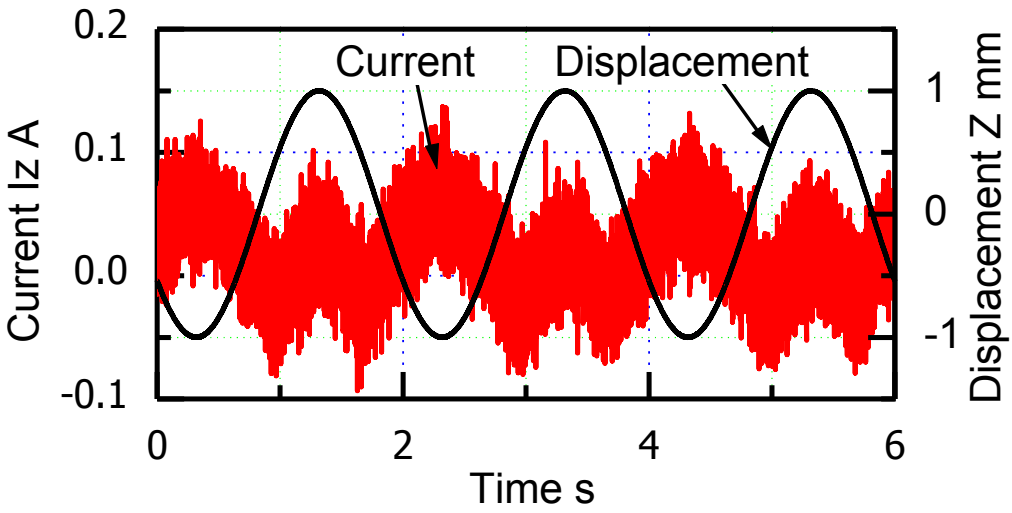

Fig. 2.22 Relationship between coil current and displacement of spindle shaft in the Z direction

2.4.6 Discharge current

To confirm whether a discharge current could be fed to the electrode when the spindle was rotating, a simulated experiment was carried out. One terminal of a voltage supply (5V) was connected to the brushes, and the other terminal was brought into contact with the electrode, via a copper leaf spring, through a resistance of 60Ω and a switch. The switch was activated at a rotational speed of 2,000min^{-1} and the current that was fed to the electrode was measured, as

shown in Fig 2.23. The experimental results confirmed that a simulated discharge current could be fed to the electrode whilst the spindle was rotating. The simulated discharge current was also measured at various rotational speeds, as shown in Fig 2.24, showing that the current did not depend on the rotational speed of the spindle.

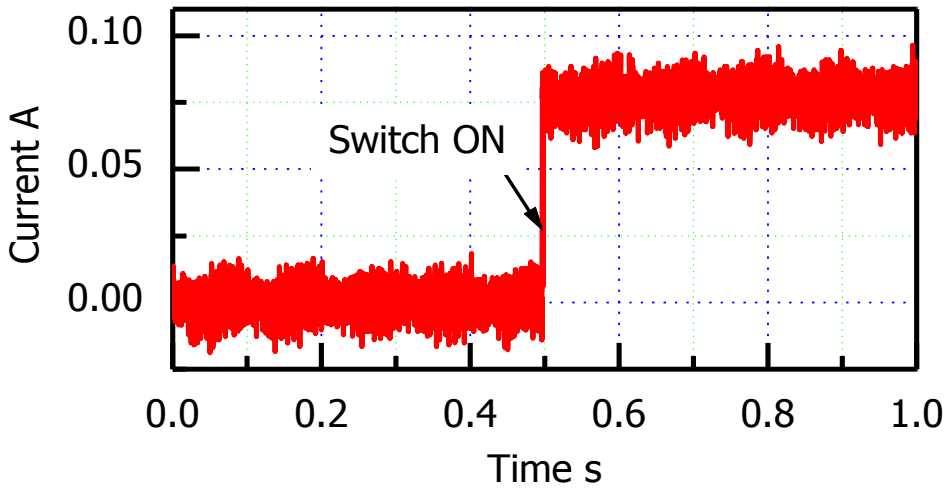

Fig. 2.23Experimental discharge current supply at 2000 rpm

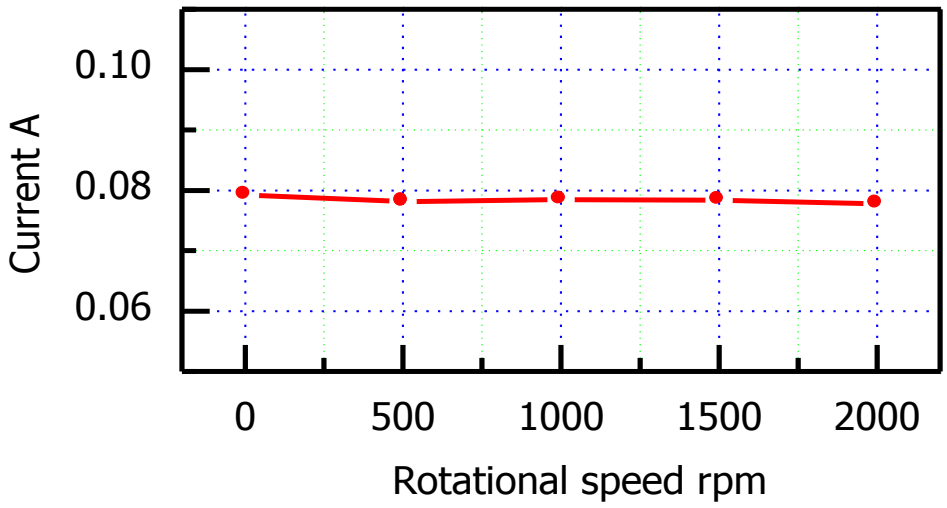

Fig. 2.24 Relationship between the rotational speed and the simulated discharge current

2.5 Conclusion

In order to realize a high speed multi-DOF motion of an electrode for high speed EDM, a compact 5-DOF controlled maglev electrode driving actuator was designed and fabricated. The new actuator primarily consists of a 5-DOF controlled magnetic bearing (MB) system, a novel magnetic coupling mechanism and a spindle shaft.

The novel magnetic coupling mechanism was proposed for not only transmitting rotational torque from a DC motor to a levitated spindle shaft, but also applying discharge voltage to an electrode which is attached to the levitated spindle shaft without direct contact between power supply brushes and the levitated spindle shaft. Furthermore, the magnetic coupling generated a restoring force to the spindle shaft in thrust direction, by which the gravity force of the spindle shaft was balanced.

The fabricated prototype maglev electrode driving actuator realized sub-micron positioning resolution with an angular resolution of several micro-radians, bandwidths greater than 200Hz in all the 5-DOF directions. It also realized positioning strokes of the spindle shaft of 2mm in the thrust direction, 180μm in the radial direction and 3.6mrad in tilt direction, respectively.

The prototype actuator could rotate the spindle shaft at up to 2,000rpm, within peak-to-peak rotational vibration amplitude of 1.5 μm, and the discharge current could be fed to the electrode while the spindle is rotating.

In the next step, the developed prototype actuator will be applied to experimental EDM, by which the effectiveness of the fast positioning response and the effectiveness of a combination of fast positioning and rotation of electrode on the machining speed will be investigated. The results of experimental EDM will be introduced in the next chapter.

Chapter 3 Experimental EDM using the maglev electrode driving actuator

3.1 Introduction

In previous research, the use of local actuators that possess faster positioning response than that of a conventional EDM machine has been studied [32-34]. These actuators increase the positioning response of the electrode to maintain a constant suitable gap to the work-piece, however, the stroke of these actuators is limited to from several tens to several hundreds of microns. Consequently, they are unable to realize neither high speed nor a long stroke jump of the electrode in the axial direction to flush the dielectric fluid away from the work-piece. The necessity for flushing the dielectric fluid for removing the debris and stabilizing the electrical discharge condition during small deep hole-EDM processes is well known.

Furthermore, related to the enhanced flushing, there have been many reports in the literatures that rotation of the electrode [35-38], orbital motion [39] and high speed jump motion [40, 41] of the electrode increase the machining speed and quality in small hole-EDM. However, there have been no reports on actuators that combine high speed positioning with rotation of the electrode.

A previously developed five degrees of freedom (5-DOF) controlled maglev electrode driving actuator enabled a rapid response to be combined with orbital motion of the electrode and a high speed stroke jump of several mm in the axial direction. The increase in machining speed using this set up has been experimentally confirmed [42-44]. However, the power supply brushes of the MLA were in direct contact with the spindle so that the electrode was unable to rotate smoothly and accurately. Kunieda et al. developed a non-contact power supply method using electrostatic induction feeding [48]; but the combination of rapid positioning, multi-DOF motion and non-contact power supply to the electrode has not been reported.

To realize rapid positioning in the axial and radial directions and long stroke positioning in the axial direction as well as high speed and accurate rotation of the electrode in small deep hole-EDM, a new compact 5-DOF controlled maglev electrode driving actuator was developed and was introduced in chapter 2. In order to evaluate the effectiveness of fast positioning response and the combination of fast positioning response and rotation of the electrode on the machining speed, experimental EDM was conducted using the new maglev electrode driving actuator.

Small through holes were machined using the conventional EDM machine, alone, without electrode rotation; and using the combination of the conventional EDM machine and the 5-DOF electrode driving actuator, with and without electrode rotation. Micro electrodes were on-machine fabricated and used to machine micro holes by using the conventional EDM machine, alone, without electrode rotation; and using the combination of the conventional EDM machine and the 5-DOF electrode driving actuator, with and without electrode rotation.

The effectiveness of fast positioning response on machining speed will be evaluated by comparing the machining rate using conventional EDM machine and the machining speed using the fast response maglev electrode driving actuator. The effectiveness of the combination of fast response and electrode rotation on machining speed will be evaluated by comparing the machining rate using the fast response maglev electrode driving actuator with and without electrode rotation.

3.2 Experimental EDM system

Before applying the actuator for experimental electrical discharge machining, there are some problems need to be solved. The first problem is to extending the fast response positioning range of the electrode; the second problem is to eliminate the clamping error of an electrode.

3.2.1 Co-operative EDM system

As the full thrust stroke of the 5-DOF maglev electrode driving actuator is limited to 2mm, when a hole with a depth larger than 2mm is machined, the feeding stroke is not enough using the maglev actuator alone. Therefore, in order not only to maintain the high response speed of the electrode, but also to have a feeding stroke much larger than 2mm during EDM, a co-operatively controlled EDM system was proposed.

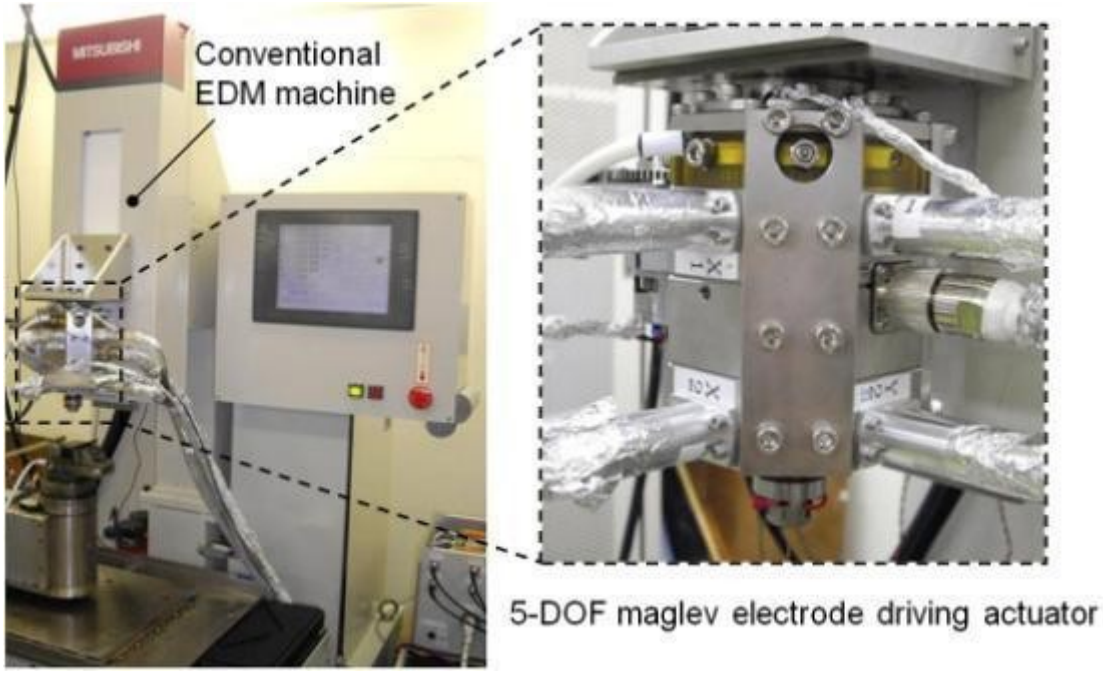

Fig. 3.1 Co-operative EDM system

Fig. 3.1 shows the experimental setup of a co-operative EDM system. In this system, the 5-DOF maglev electrode driving actuator plays as a local actuator, and is mentioned as a maglev local actuator (MLA) in this chapter [49]. The 5-DOF MLA is attached to a conventional EDM machine (MEMH8N, Mitsubishi Electric Corporation.), which has a large stroke (300×200×200mm), high positioning accuracy (1μm resolution) in three orthogonal directions, but low response speed (several Hz to dozen Hz), no tilt motion to the electrode, and cannot rotation the electrode.

In the process of EDM, in order to maintain the suitable gap distance between the electrode and the work-piece, the electrode is attached on the

spindle shaft of the MLA, the MLA adjusts the position of the electrode speedily and precisely. The conventional EDM machine plays as a coarse positioning stage, it is used to feed the MLA body slowly in the machining direction in order not to saturate the feeding stroke of the MLA and to supply the discharge power to the electrode.

3.2.2 EDM control system (Co-operative control)

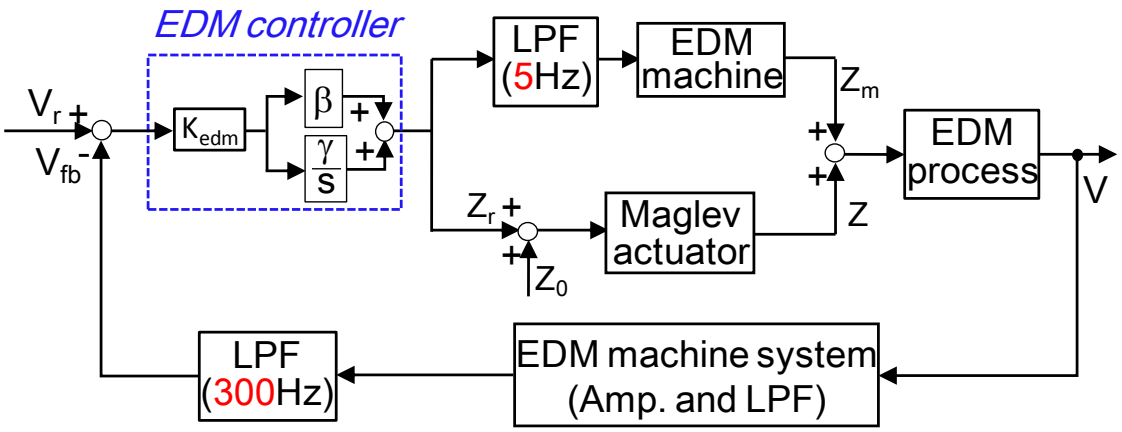

Fig. 3.2 Control system of co-operative EDM

Fig. 3.2 shows the co-operative control system in the Z-direction. During EDM, the discharge voltage V between the electrode and work-piece was monitored by the conventional EDM machine system through a LPF with a cut-off frequency of 300Hz and was used as a feedback signal.

The EDM controller consists of a gain K_{edm} of 1.0 and a PI controller, β is 1.29×10^{-6} and γ is 1.5×10^{-4}, which decided by trial and error. The EDM controller generated the reference position of the electrode in the thrust direction according to the feedback voltage V_{fb} and a reference EDM voltage V_r.

The reference position was entered into the maglev actuator system directly and into the conventional EDM machine through a LPF with a cut-off frequency of 5Hz. Following the reference position, the MLA adjusted the electrode speedily and precisely to maintain a suitable distance from the work-piece, and the conventional EDM machine fed the mounted MLA with the electrode, slowly

and continuously in the machining feed direction, for coarse positioning and for avoiding the saturation of the positioning stroke of the MLA. Therefore, the co-operative EDM system realized as large positioning stroke as that of the conventional EDM machine, and as fast positioning response as the MLA.

However, when using the conventional EDM machine only to feed the electrode during machining, the MLA levitaed the spindle shaft with an electrode, the reference Z_r was set to 0. The reference position calculated by the EDM controller was entered into the conventional EDM machine only.

3.2.3 Rotational accuracy improvement of the electrode

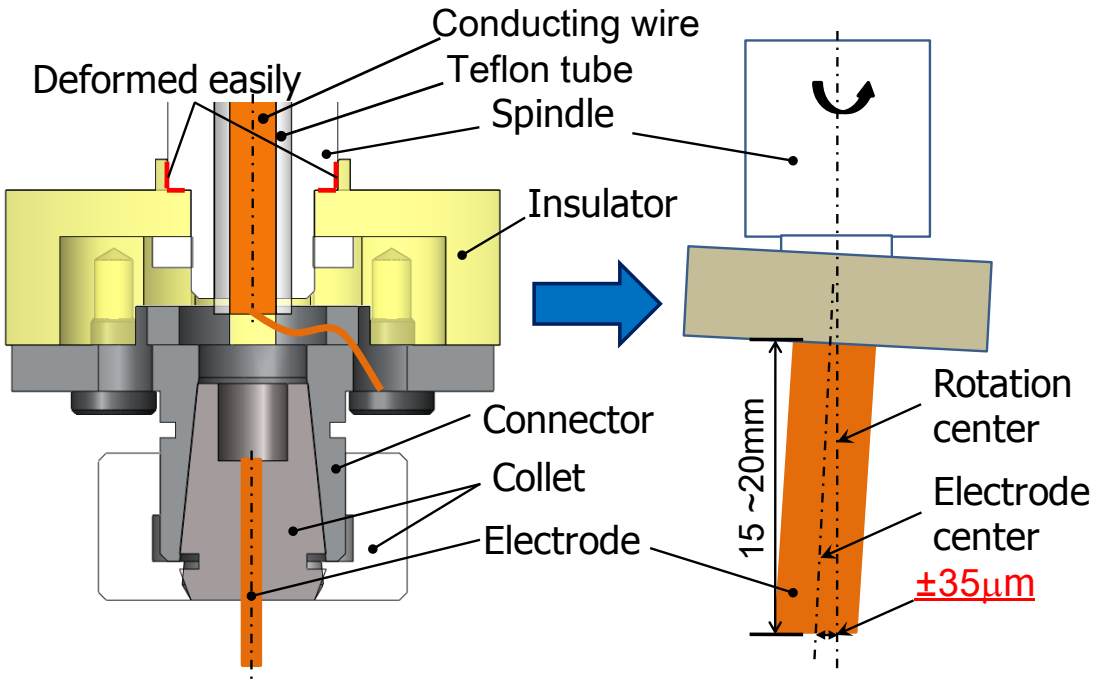

Fig. 3.3 Electrode attachment mechanism (initial type)

Before applying the MLA to experimental rotary machining, there is another problem, the insufficient rotational accuracy of the electrode. Fig 3.3 shows an initial designed electrode attachment mechanism, which consists of an insulator, a connector and a set of a collet. The insulator is used to insulate the spindle shaft from the discharge current, the collet is used to chuck an electrode for EDM, and the connector combined with the insulator are used to attach the collet and

the electrode to the spindle shaft.

In experiment, the direct contact part between the spindle and the insulator was too weak and deformed easily, therefore, when the electrode rotated together with the spindle shaft, there was an unacceptable coaxiality error between the electrode center and the rotational center. When the electrode length was 15-20mm, a peak-to-peak vibration amplitude of about 70μm (± 35μm) was observed at the end the of the electrode whereas this value of the spindle shaft was less than 1.5 μm.

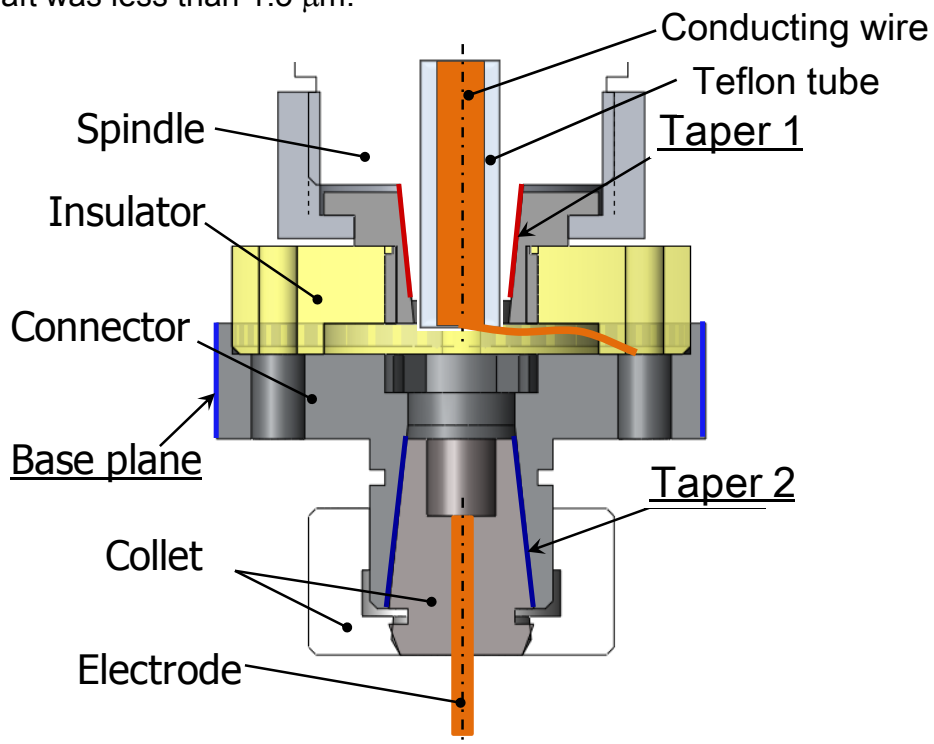

Fig. 3.4 New electrode attachment mechanism

In order to decrease the coaxiality error between the electrode center and the spindle shaft center, a new attachment mechanism and a new spindle shaft were designed and fabricated, as shown in Fig 3.4. In the new mechanism, there are two tapers, taper 1 is used to connect the attachment to the spindle shaft and taper 2 is used to attach the collet and the electrode. In order to assure the coaxiality, both tapers and the insulator were assembled together and then these two tapers were machined base on the same outer cylindrical surface of the connector.

Fig 3.5 shows the initially fabricated spindle shaft and a new one. The structure of the driving components of these two spindle shafts are the same. The length of the spindle shaft without the electrode attachment is enlarged from 123mm to 127.5mm, and the weight of the spindle shaft without the electrode attachment is increased from 0.35kg to 0.476kg.

Fig 3.6 shows the newly fabricated spindle shaft assembled with the new electrode attachment. The copper wire in the center of the spindle shaft is used for feeding the discharge current to the electrode during EDM, and a Teflon tube is used to insulate the spindle shaft from the copper wire. The weight of the spindle shaft with all attachments is 0.532 kg, and the length is 148mm.

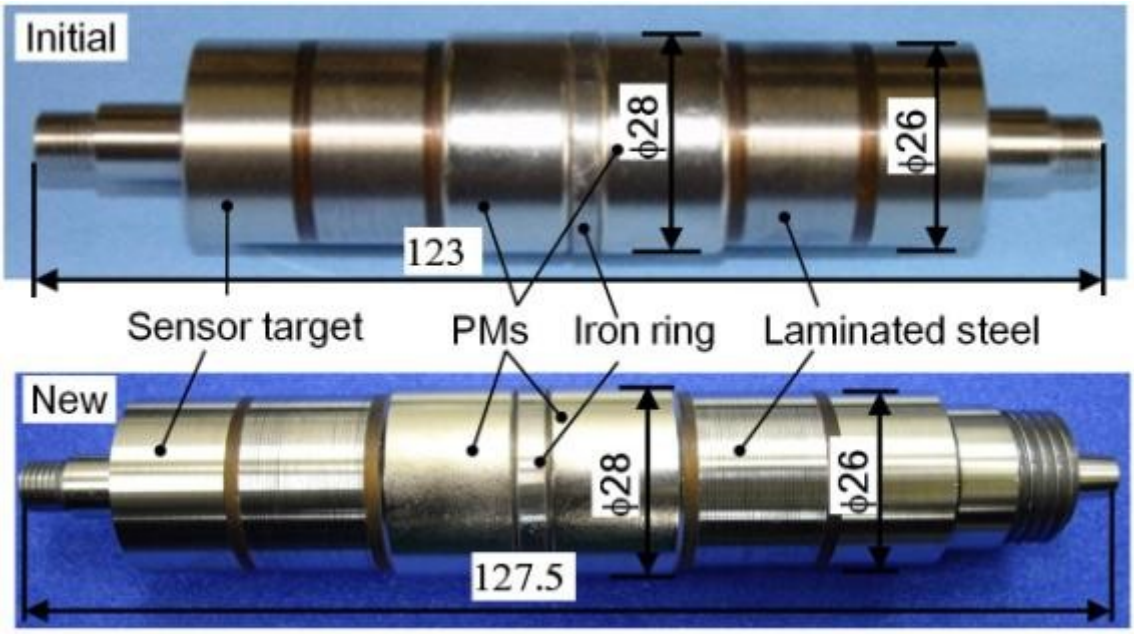

Fig. 3.5 Spindle shafts

Fig. 3.6 Spindle shaft and electrode attachment (new type)

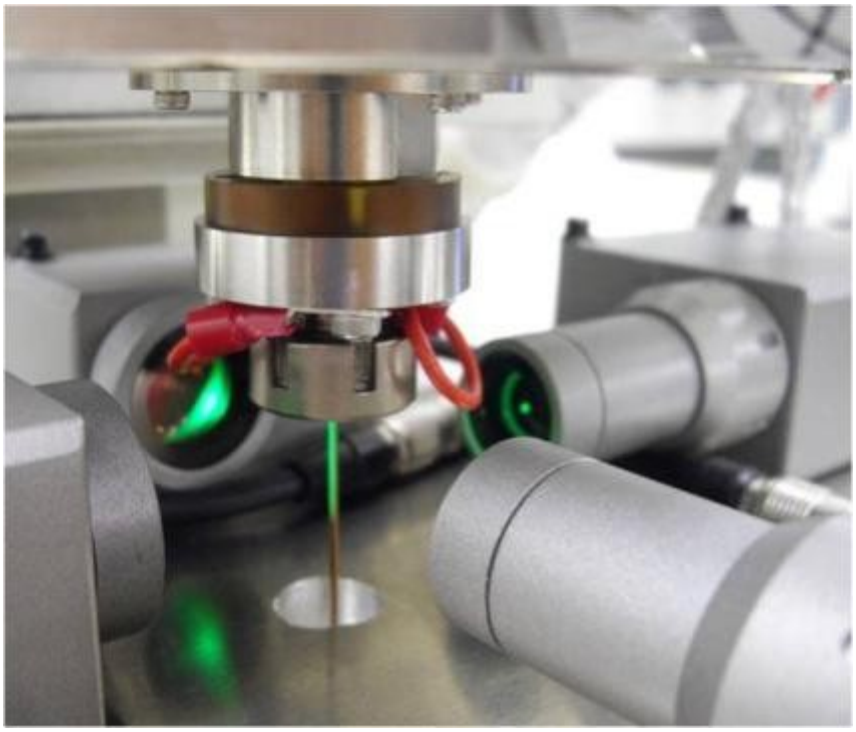

Fig. 3.7 Measurement of electrode rotational accuracy

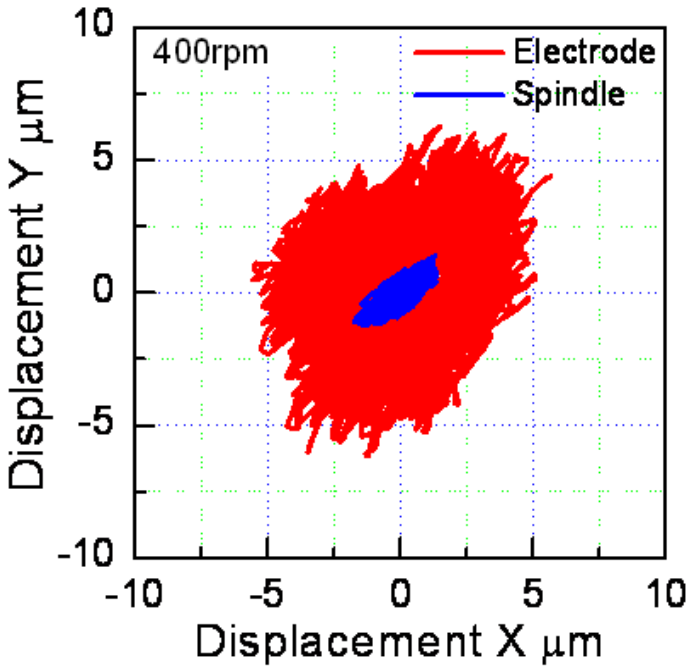

Fig. 3.8 Rotational vibration of electrode

After fabricated the new spindle shaft and electrode attachment, the

rotational accuracy of electrode was measured by a set of laser digital displacement sensor (Digital Laser Micrometer LS-7600 Series, KEYENCE CORPORATION, resolution: 0.5 μm), as shown in Fig 3.7.

Fig 3.8 shows the result of measured rotational vibration of an electrode at 400rpm, using the newly fabricated spindle shaft and electrode attachment. The electrode diameter was ϕ1mm, the length was 20mm and the measured position was the end of the electrode. The result indicates that the peak-to-peak vibration amplitude significantly decreased from about 70μm to 10μm, which is acceptable for stable EDM.

3.3 Experimental rotary EDM

3.3.1 Experimental machining conditions

In order to evaluate the effectiveness of fast response and high-accuracy positioning of the electrode by the MLA, and the effectiveness of combination of fast positioning response and electrode rotation on the machining speed, small-deep holes were experimentally machined. Three different machining methods were experimentally investigated.

Method 1, using the conventional EDM machine, alone, without electrode rotation; method 2, using the co-operative EDM system introduced in previous section, without electrode rotation, method 3, using co-operative EDM system with electrode rotating from 200rpm-1200rpm at intervals of 200rpm.

Cylindrical shaped copper electrodes with diameters of 1mm and 0.5mm were used and the machining was continued until the electrode penetrated a 4mm thick pre-hardened steel work-piece with a hardness of 40 HRc (NAK 80, Daido Steel Corp., Ltd.). Pure water was used as the dielectric machining fluid. The capacitor in the EDM power-supply was charged and discharged using a controllable high-frequency switching circuit.

Fig. 3.9 shows an output of the EDM power-supply, the polarity changes every 17μsec in order to avoid the electrical erosion of the EDM machine, and

the absolute open-circuit value is 190V. The displacement of the MLA body in machining direction Z_m, the thrust displacement of the electrode in the MLA Z, and the monitored feedback voltage V_{fb} during machining were recorded

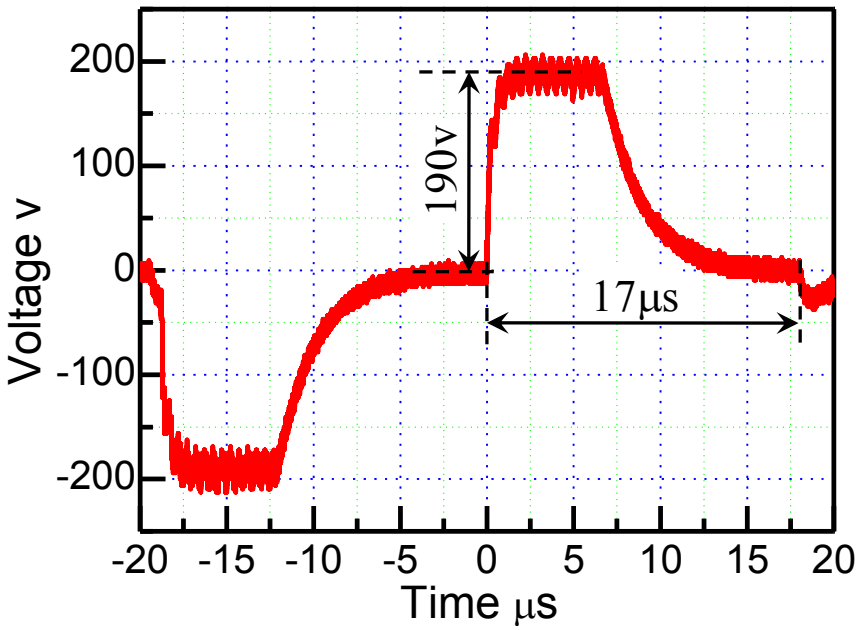

Fig. 3.9 Output of EDM power supply

3.3.2 Machining feeding process

In co-operative EDM, the MLA adjusted the position of the electrode for maintaining the suitable gap distance between the electrode and the work-piece, the conventional EDM machine fed the MLA in the machining direction. Since the adjusted range of the electrode by the MLA was just several-ten micrometers, which was much smaller than the feeding range of the MLA body, more than 6,000 micrometers, so we show the displacement of the EDM machine stage Z_m to explain the machining feed process.

Fig. 3.10 and Fig. 3.11 show the displacement of the conventional EDM machine stage Z_m, i.e. the displacement of the MLA body that attached on the stage. The feeding data was recorded by a data recorder (EZ7501, NF Corp., at a sampling frequency of 5 KHz). In the case of ϕ0.5mm, for machining a 4mm through hole, it took 4386 sec. by using the conventional EDM machine without

electrode rotation (0rpm); took 2075 sec. by using the co-operative EDM system without electrode rotation (0rpm); and took 974 sec. by using the co-operative EDM system with electrode rotating at 800rpm.

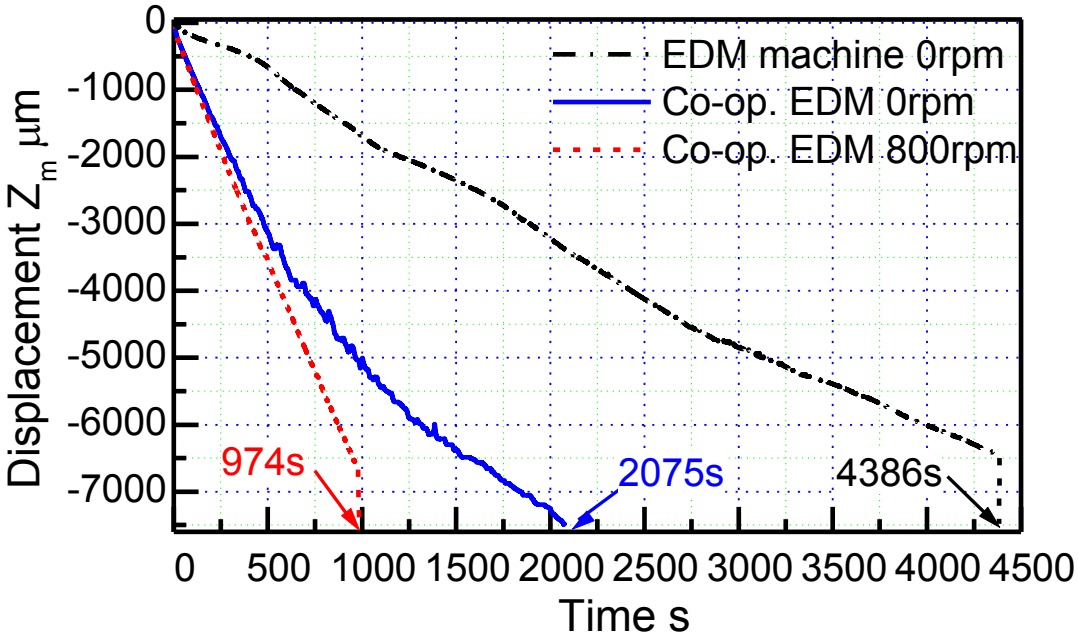

Fig. 3.10 Displacement of the MLA during machining (ϕ0.5mm×4mm)

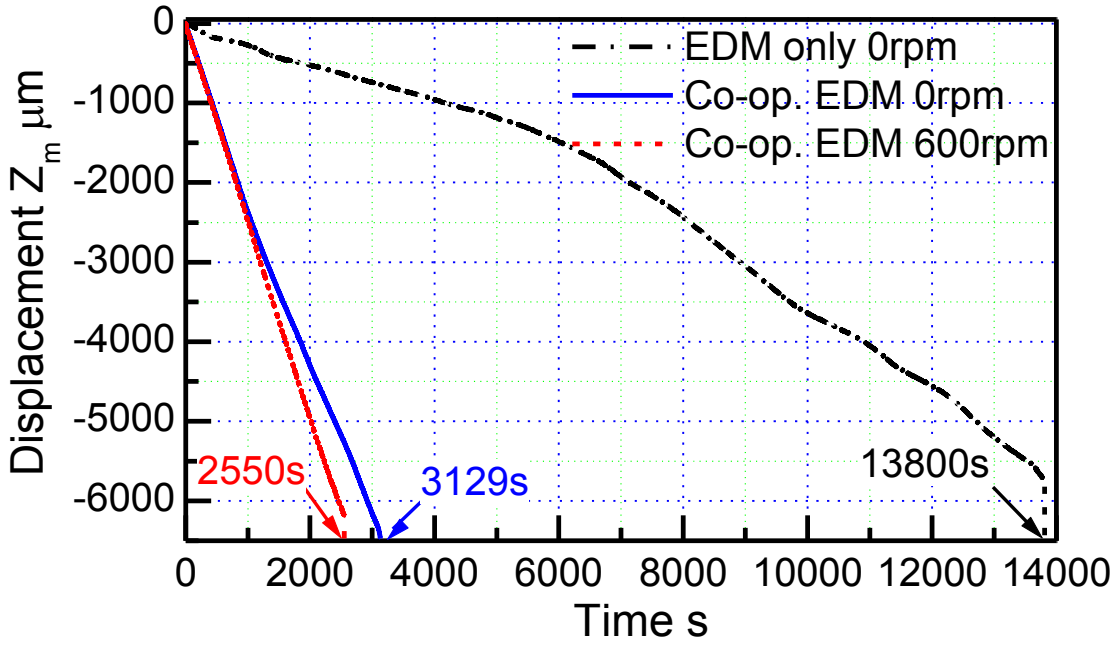

Fig. 3.11 Displacement of the MLA during machining (ϕ1 mm×4mm)

In the case of ϕ1mm, for machining a 4mm through hole, it took 13800 sec. by using the conventional EDM machine without electrode rotation (0rpm); took

3129sec. by using the co-operative EDM system without electrode rotation (0rpm); and took 2550 sec. by using the co-operative EDM system with electrode rotating at 600rpm.

According to the results, under the same machining conditions, to machine holes of the same diameter and depth, the co-operative EDM took less time than that of conventional EDM machine; in co-operative EDM, the rotary machining took less time than that of non-rotary machining.

3.3.3 Effectiveness of co-operative control

In order to analyze how the co-operative control affected the experimental small-deep holes machining, the feedback voltage V_{fb} between the electrode and the work-piece, and the displacement of the spindle shaft (electrode) Z in the MLA were analyzed. The case of ϕ0.5mm×4mm machining is taken as the example in this section.

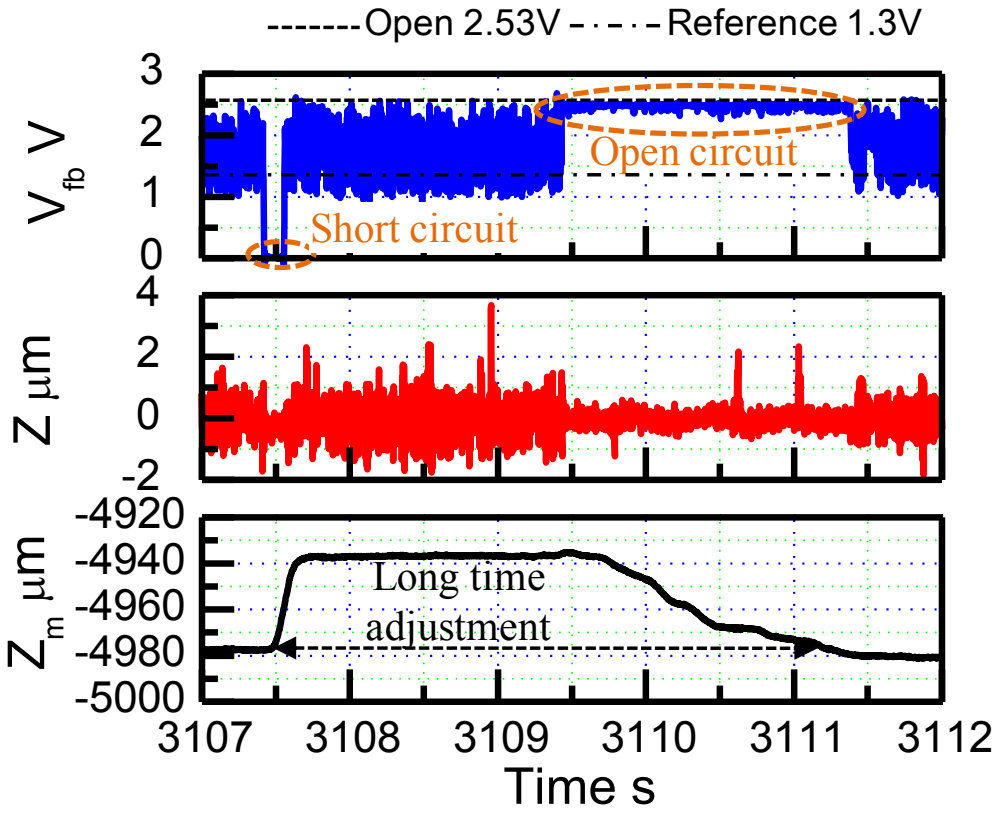

Fig. 3.12 EDM process of conventional EDM machine (ϕ0.5mm×4mm)

Fig. 3.12 shows the V_{fb}, Z and Z_m during experimental machining using the conventional EDM alone, without electrode rotation. Fig. 3.13 shows the V_{fb}, Z and Z_m of machining using the co-operative EDM system, without electrode rotation.

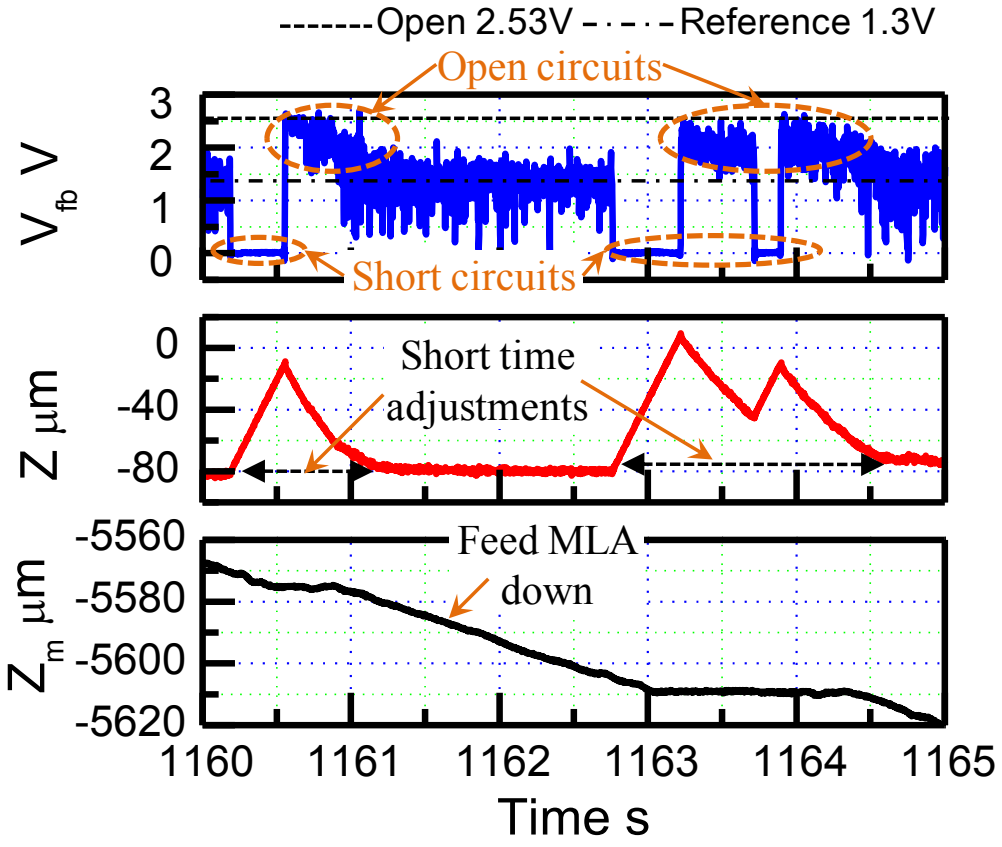

Fig. 3.13 EDM process of co-operative EDM (ϕ0.5mm×4mm)

The feedback voltage was monitored by the EDM machine system before feedback to the EDM controller, the signals do not show the open and short circuit conditions in the strict sense. Here a V_{fb} of 0V implies a short circuit condition, and a V_{fb} of 2.53V implies an open circuit, the voltage between the electrode and the work-piece was equal to the power-supply voltage (190V) at this time. The V_{fb} of 1.3V was the value of the reference voltage V_r which was used to control the position of the electrode during machining.

According to the result in Fig. 3.12, when a short circuit happened during

the machining, usually caused by the debris accumulating around the electrode, the EDM machine adjusted the position of the electrode by retracting the electrode together with MLA body to avoid short circuit, the MLA hold the electrode constantly in the initial position. After the electrode was retracted for several-ten microns together with the MLA body, the debris around the electrode caused abnormal electrical discharge between the side cylindrical surface of the electrode and the inner wall of machined hole, which would stop until all the debris be cleared. After that, an open circuit happened due to the large gap distance between the electrode and work-piece, therefore, the EDM machine fed the electrode together with the MLA body toward to the work-piece to restart machining. As the response speed of the conventional EDM machine is limited, it took more than 3 seconds to adjust the position of electrode when a short circuit occurred, the machining efficiency was relatively low.

In the case of co-operative EDM, as shown in Fig. 3.13, when a short or open circuit occurred, the MLA adjusted the electrode, which attached to the spindle shaft, in thrust direction, and the conventional EDM machine stopped feeding during the adjustment. Since the MLA possesses high-speed and high-accuracy in all the 5-DOF, it took much less time (about less than 1 second) to adjust the electrode than that of using the conventional EDM machine, thus, the co-operative EDM obtained higher machining efficiency.

Furthermore, when the feedback voltage V_{fb} was around 1.3V, the discharge was taken on stably and continuously, in this situation, the MLA adjusted the electrode in a range of several microns for maintaining the suitable gap distance and the EDM machine fed the electrode together with the MLA slowly in machining direction. Therefore, the co-operative EDM had a higher machining speed than that of the conventional EDM machine.

3.3.4 Effectiveness of electrode rotation

In order to evaluate the effectiveness of electrode rotation to the machining speed, we analyzed the variation of the displacement of the electrode in the MLA Z and the feedback voltage V_{fb} during the whole machining process. Fig. 3.14 shows the Z and V_{fb} of co-operative EDM without electrode rotation (0rpm) and with electrode rotating at 800rpm in the case of ϕ0.5mm×4mm machining; Fig. 3.15 shows the Z and V_{fb} of co-operative EDM without electrode rotation (0rpm) and with electrode rotating at 600rpm in the case of ϕ1mm×4mm machining.

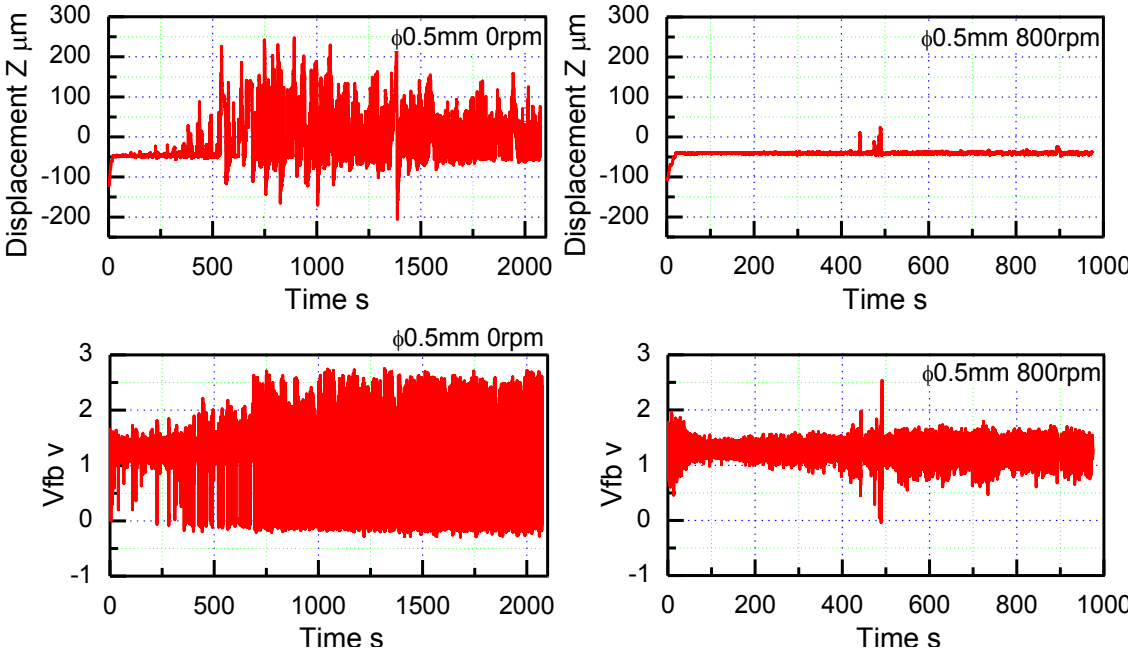

Fig. 3.14 Electrode vibration and feedback voltage variation of co-operative EDM (ϕ0.5mm×4mm)

According to the results, with the electrode rotation, the vibration amplitude of electrode in thrust direction was lower and the variation of feedback voltage was smaller compared to those of without electrode rotation.

The reason was that the electrode rotation increased the flushing of dielectric machining fluid, with the increased flushing of machining fluid, debris accumulating around the electrode were removed more efficiently, so there were less incidents of short or open circuit and abnormal electrical discharge happened during machining.

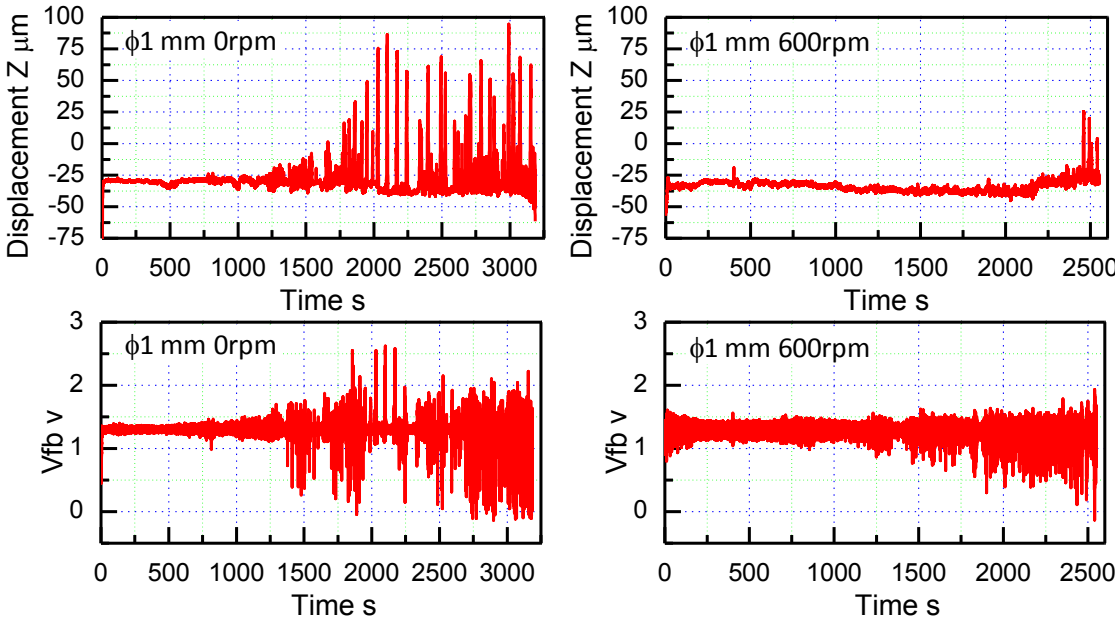

Fig. 3.15 Electrode vibration and feedback voltage variation of co-operative EDM (ϕ1mm×4mm)

3.3.5 Machining speed

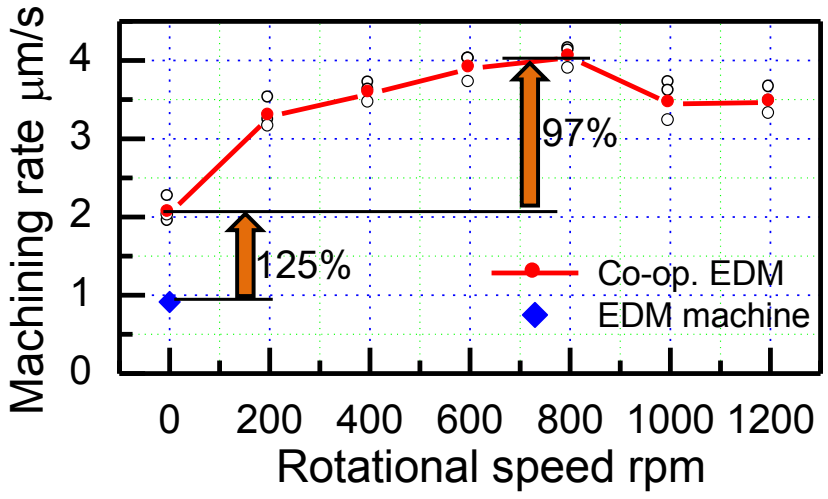

Fig. 3.16 Machining rate of ϕ0.5mm×4mm hole EDM

The machining speed of the experimental machining was evaluated by comparing the machining rate of each machining method. The machining rare is

defined as the ratio of the depth of machined hole to the machining time in this study. Fig. 3.16 and Fig. 3.17 show the machining rates of ϕ0.5mm×4mm machining and ϕ1mm×4mm machining in all cases.

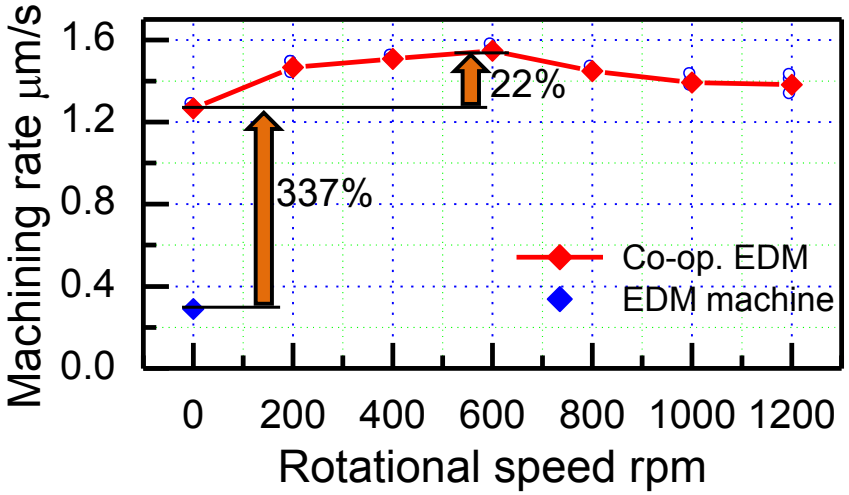

Fig. 3.17 Machining rate of ϕ1mm×4mm hole EDM

As the result in Fig. 3.16, in ϕ0.5mm×4mm machining, without electrode rotation, co-operative EDM increased the machining rate by 125% compared to that of conventional EDM machine, in the case of co-operative rotary EDM, the machining rate was increased by maximum 97% at 800rpm compared to that co-operative EDM without electrode rotation.

And in ϕ1mm×4mm machining, as the results shown in Fig. 3.17, without electrode rotation, cooperative EDM increased the machining rate by 337% compared to that of conventional EDM machine, in the case of co-operative rotary EDM, the machining rate was increased by maximum 22% at 600rpm compared to that co-operative EDM without electrode rotation.

In the experiment, debris accumulating around the electrode caused abnormal electrical discharge sparks between the side surface of the electrode and the inner surface of the machined hole. When the electrode was not rotating, the abnormal discharge continued for a relatively long time, lowering the

machining efficiency. However, when the electrode was rotating, the abnormal discharge seldom happened. The electrode rotation might help the efficient removal of the debris the increased flushing.

Since the machined holes had the same depth but different diameters. The smaller the diameter, i.e. the larger aspect ratio, the more difficult the ejection of the debris accumulating around the electrode became. Thus, a more noticeable effect on the machining rate occurred in ϕ0.5mm×4mm machining with electrode rotation.

3.3.6 Feedback voltage and electrical discharge probability

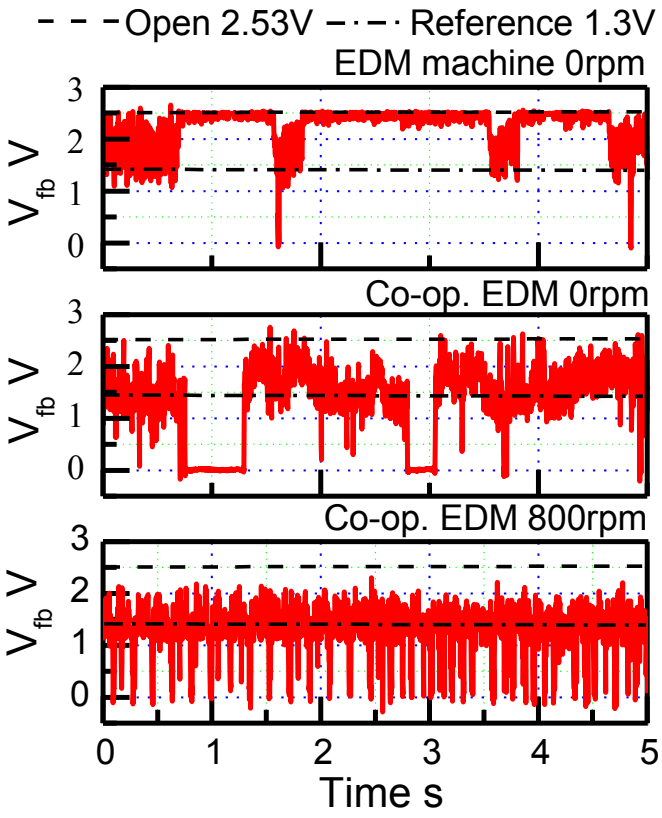

Fig. 3.18 Feedback voltage of co-operative EDM (ϕ0.5mm×4mm)

We noticed that, at the rotational speeds of electrode larger than 800rpm in ϕ0.5mm×4mm machining and 600rpm in ϕ1mm×4mm machining, the machining

speeds did not increase anymore, but started decreasing. To investigate the reason of this phenomenon, the electrical discharge probability was derived from the feedback voltage during machining.

Fig. 3.18 shows the real time feedback voltage of three different machining cases in ϕ0.5mm×4mm through hole machining by using conventional EDM machine without electrode rotation (0rpm), using co-operative EDM without electrode rotation (0rpm) and using co-operative EDM with electrode rotation at 800rpm.

According to the results, in the case of machining using conventional EDM machine without electrode rotation, there were long time open circuits; in the case of machining using co-operative EDM without electrode rotation, there were short time short circuits; in the case of machining using co-operative EDM with electrode rotation at 800rpm, there were seldom short and open circuits.

Assuming that stable electrical discharge takes place when the V_{fb} is between 20% (0.5v) and 80% (2.0v) of the open-circuit voltage, the total electrical discharge time could be calculated using the measured feedback voltage.

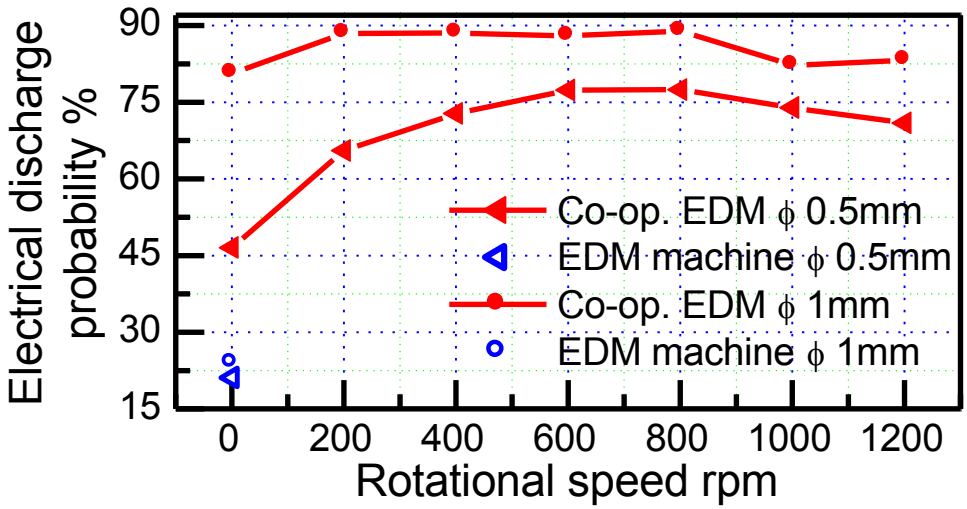

Fig. 3.19 Electrical discharge probability

In this study, the electrical discharge probability (EDP) is defined as the ratio of the total electrical discharge time to the machining time. Fig. 3.19 shows the EDP of ϕ0.5mm×4mm and ϕ1mm×4mm holes machined by using the conventional EDM machine only without electrode rotation and using the co-operative EDM at various electrode rotational speeds.

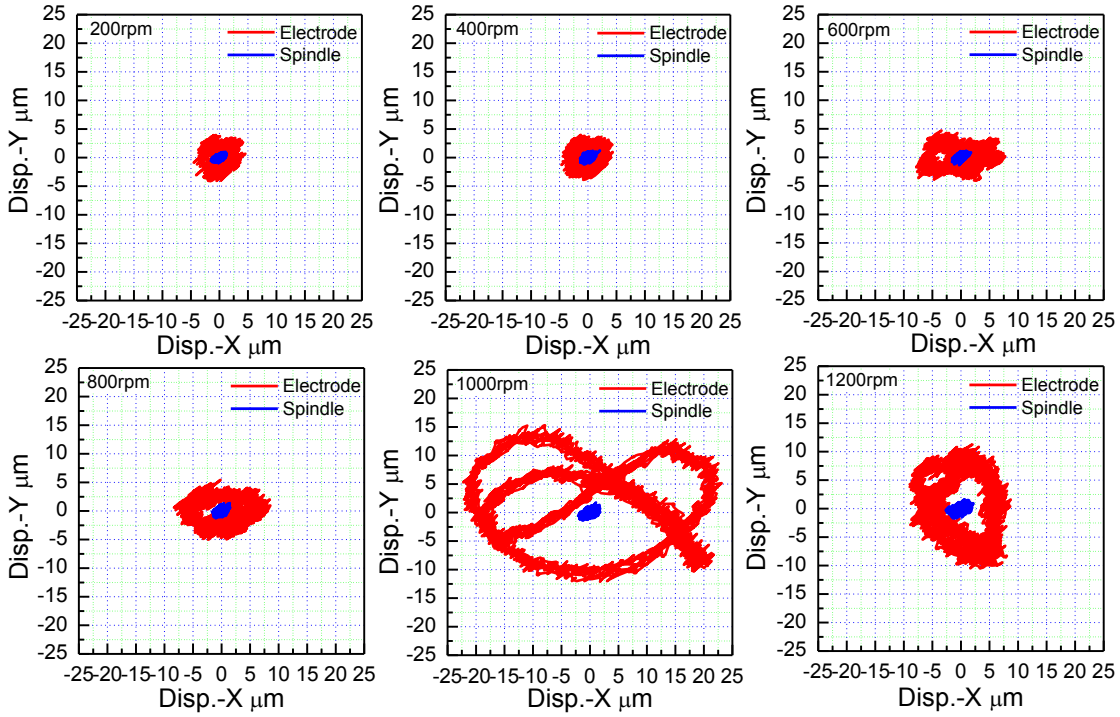

Fig. 3.20 Rotational vibration of electrode (ϕ0.5mm) and spindle shaft at various rational speeds

The co-operative EDM exhibited a much higher EDP than that of EDM machine, alone, due to the improved response speed. Furthermore, the co-operative EDM with the electrode rotation at 600-800rpm obtained a higher EDP than the value at the other rotational speeds, the results of EDP are coincide with the results of machining speeds. The decrease of both machining speeds and EDP at more than 800rpm might because the increased rotational speed would increase the vibration of electrode. Fig. 3.20 shows the rotational vibration of ϕ0.5mm electrode at various rotational speeds. Due to the limited

stiffness of the positioning stage of the EDM machine tool, which was used to attach the maglev electrode driving actuator to the machine tool, after rotational speed larger than 800rpm, the vibration of actuator body happened, which made the electrode vibration increased, and the increased electrode vibration would increase the abnormal discharge and make the gap voltage between the electrode and work-piece unstable.

3.4 Micro EDM

3.4.1 Fabrication of micro electrode

In this section, micro EDM utilizing the prototype MLA is examined. The target of the micro EDM is to machine micro holes with diameter less than 100μm and aspect ratio larger than 10.

For machining the micro holes, micro electrodes are required and should be attached to the MLA accurately. However, in experiments, the positioning accuracy of micro electrodes is greatly affected by the clamping error. To solve the problems, there are two possible methods: one is to compensate the attitude of the spindle shaft of the MLA depending on the clamping error; the other one is on-machine fabrication of the electrode. The on-machine fabrication was tested in this study.

3.4.2 Fabrication concept of micro electrode

In order to fabricate a micro cylindrical electrode without any clamping error, the basic concept is as follows:

The first step is to clamp a rod tool electrode with a relatively large diameter than the target electrode on the MLA spindle shaft.

The second step is to clamp a bulk work-piece on the EDM machine as a sacrificial electrode.

Final step is to machine the side cylindrical surface of the tool electrode using the plane side surface of the sacrificial electrode by rotary electrical discharge, until the diameter of the tool electrode reaches the desired value.

3.4.3 Fabrication method of micro electrode

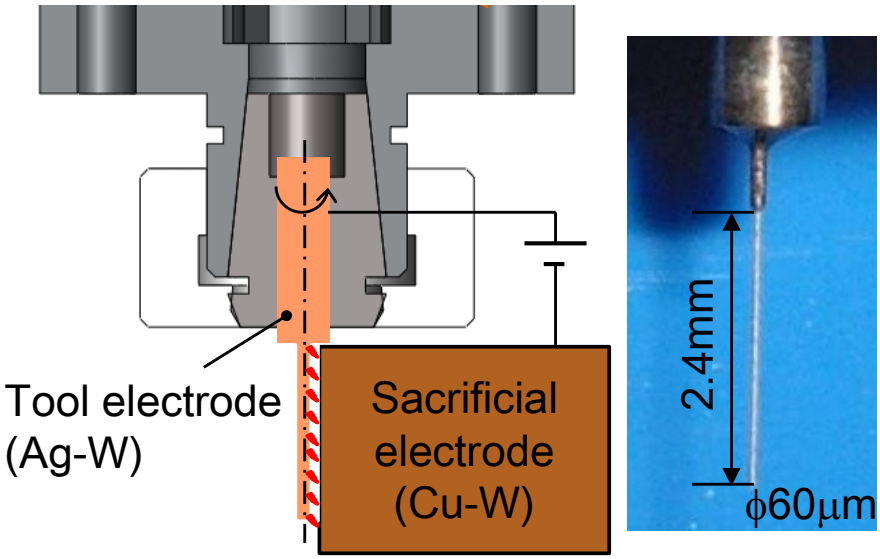

Fig. 3.21 On-machine fabrication of micro electrode and a fabricated micro electrode

In the on-machine fabrication, cylindrical shaped Ag-W electrodes with a diameter of 1mm were used as tool electrode, a bulk Cu-W work-piece was used as a sacrificial electrode. The machining fluid was oil (EDF-K, Nippon Oil Corp.).

Fig. 3.21 shows the image of on-machine fabrication setup. During fabrication, the tool electrode was attached to the spindle shaft of the prototype MLA, and was levitated by the prototype MLA and rotated at 800rpm. The conventional EDM machine tool was used to feed the electrode together with the MLA body, and to supply the discharge voltage between the tool electrode and sacrificial electrode.

3.4.4 Fabrication results of micro electrode

Fig. 3.21 also shows an example of fabricated micro electrode. A set of laser

digital displacement sensor (Digital Laser Micrometer LS-7600 Series, KEYENCE CORPORATION, resolution: 0.5 μm) measured the diameter and rotational vibration of the on-machine fabricated micro electrode, as shown in Fig 3.22.

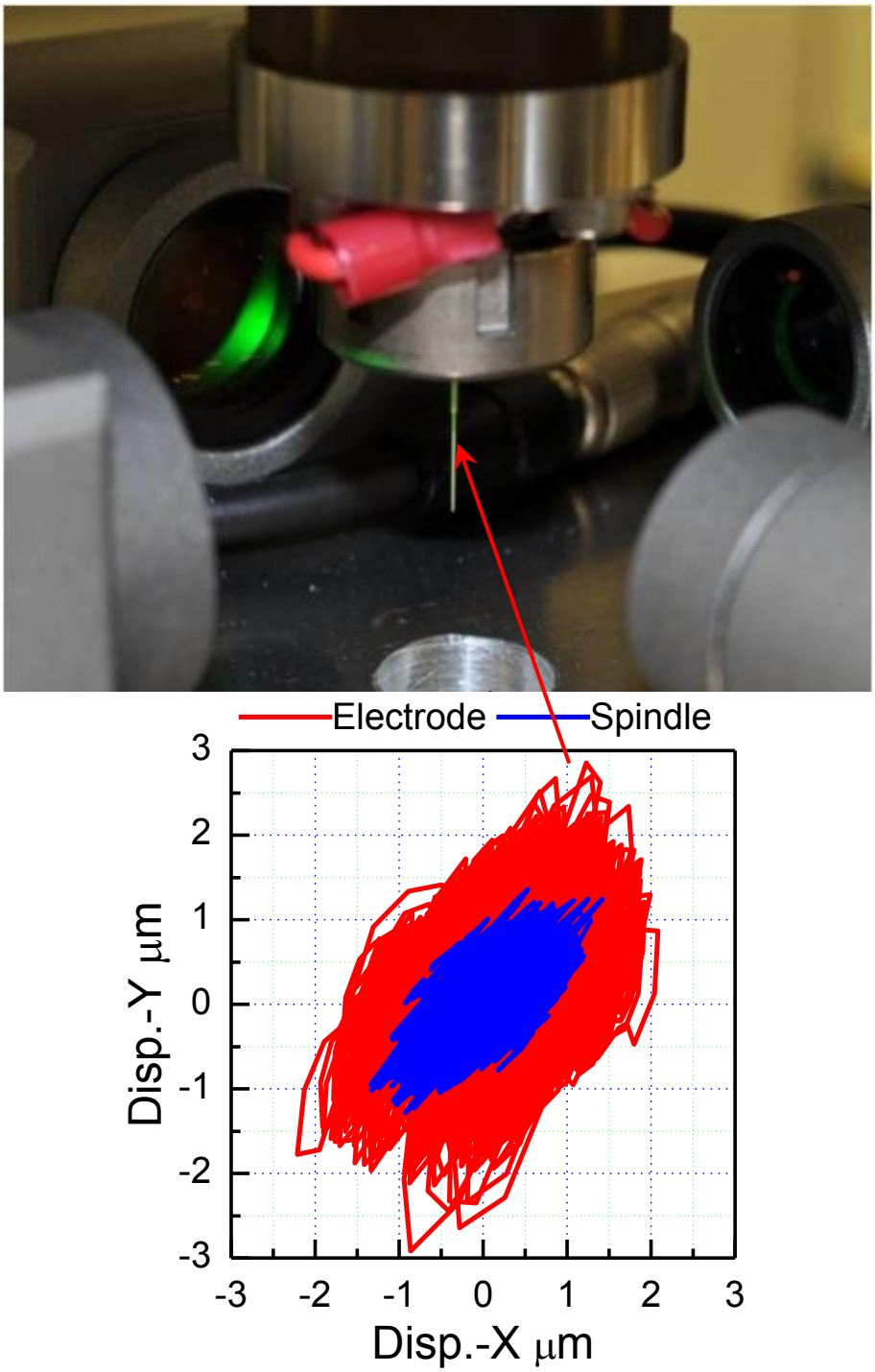

Fig. 3.22 Rotational accuracy of on-machine fabricated micro electrode

For maintaining sufficient stiffness and avoiding tapper error of the electrode, the length and diameter of the on-machine fabricated electrode was limited to 2.4mm and ϕ60μm, respectively. The rotational vibration of the on-machine fabricated micro electrode was measured at the electrode end under 200rpm, the value is less than $\pm$3μm, and is acceptable for conducting stable micro hole EDM.

3.4.5 Micro hole EDM

Using the on-machine fabricated micro electrodes, the micro-hole EDM was experimentally tested. Micro holes were machined on 1 mm thick pre-hardened steel work-piece with a hardness of 40 HRc (NAK 80, Daido Steel Corp., Ltd.). The machining fluid was oil.

Three different machining methods were conducted: using the conventional EDM machine alone, without electrode rotation; the co-operative EDM without electrode rotation and co-operative EDM with electrode rotating at 800rpm. The machining was continued until the electrode penetrate the 1mm thick work-piece or stopped after feeding 2.3mm due to the limited electrode length of 2.4mm

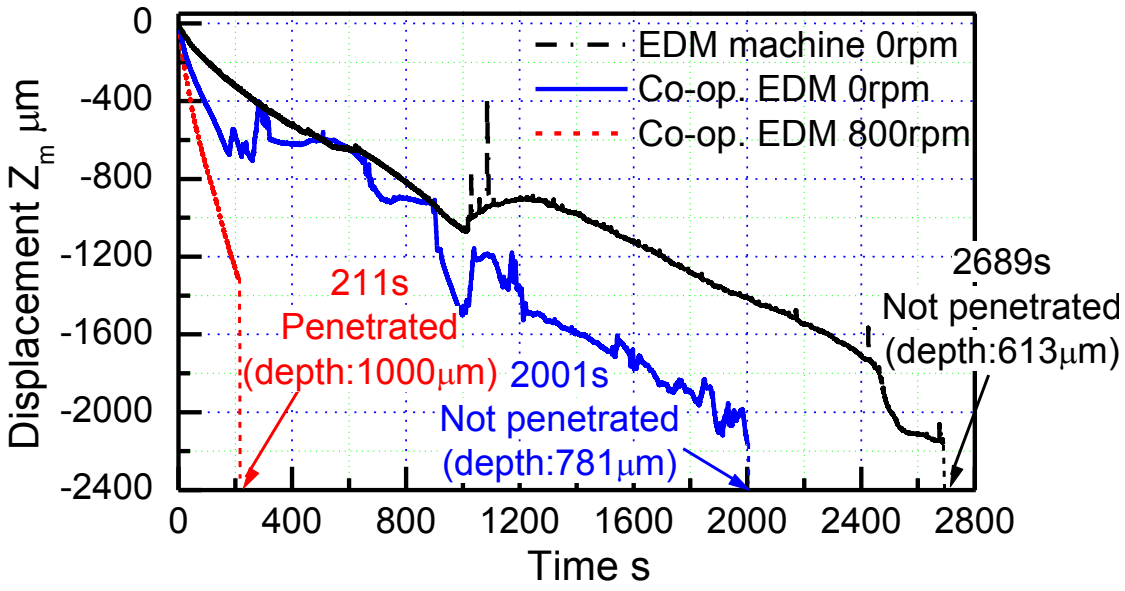

Fig.3.23 Machining feeding processes of micro holes machining

Fig. 3.23 shows the machining feeding process of each machining case. According to the results, the co-operative EDM with electrode rotating at 800rpm penetrated the work-piece, however, without an electrode rotation, both conventional EDM machine and co-operative EDM failed to penetrate the work-piece until feeding the electrode by 2.3mm. A laser microscope (VK-8700/9700 Generation II, KEYENCE CORPORATION) measured the depth of machined micro blind holes.

According to the measured depth of holes machined by conventional EDM machine and by co-operative EDM system without electrode rotation, within the same feeding range of 2.3mm, the co-operative EDM without electrode rotation machined deeper in a shorter time compared to that of the conventional EDM.

The machining rate of each machining case was calculated, which is defined as the depth of each machined hole divided by its machining time. The co-operative EDM with electrode rotating at 800rpm obtained a machining rate of 4.74μm/s, which is about 12 times as that of the co-operative EDM without electrode rotation, 0.39μm/s, and about 22 times as that of conventional EDM without electrode rotation, 0.22μm/s.

Comparing the increases of machining speeds in experimental small-holes and micro-holes machining, the reduction of electrode diameter could enhance the effectiveness of electrode rotation to the machining speed.

3.4.6 Machined micro holes

Fig. 3.24 shows the view of entrance and exit of a 1mm micro through hole machined by co-operative EDM with electrode rotating at 800rpm. The entrance diameter was ϕ98μm and the exit one was ϕ82μm, the aspect ratio was 10.2. However, tapper shape error also observed. The prototype MLA realized multi-DOF motion of the electrode in three orthogonal directions and two tilt directions, the elimination of tapper error by applying tilt and radial compensation of the electrode using the MLA during machining will be experimentally

investigated in future work.

Fig. 3.25 shows the view of entrance of micro blind holes machined by conventional EDM machine and co-operative EDM system, without electrode rotation. The entrance diameters of machined micro holes were large than that of hole machined with electrode rotation, furthermore, roundness error also observed.

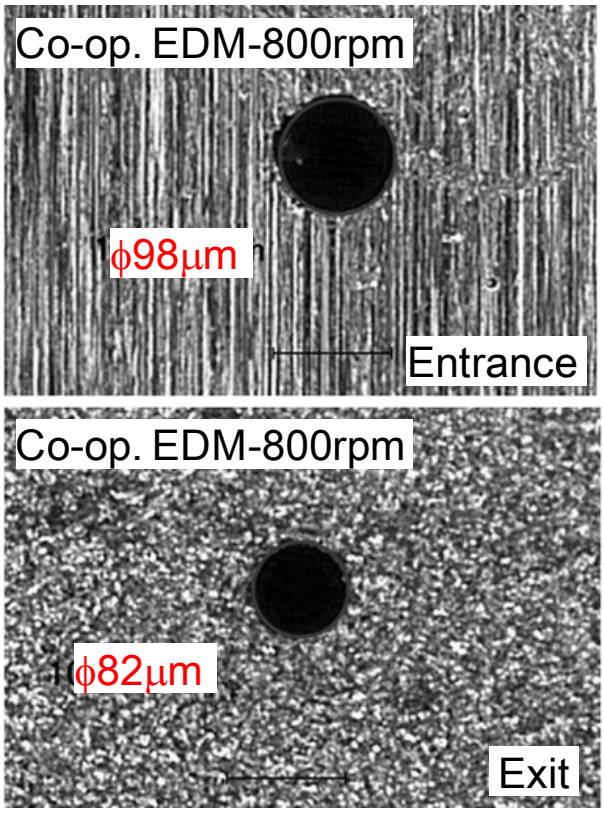

Fig. 3.24 Micro through hole (depth: 1mm)

It is considered that, the debris formed by removed material from both electrode and work-piece accumulated around the electrode, and caused abnormal electrical discharge between the outer cylindrical surface of the electrode and the inner wall surface of machined hole, which removed material from the outer cylindrical surface of electrode and inner wall surface of machine hole.

Without the electrode rotation, the debris was harder to be removed from the machined hole, which made more material to be removed from the inner wall

of machined hole by abnormal electrical discharge caused by debris. Therefore, the diameter of the machined hole without electrode rotation was larger than that the diameter of machined hole with electrode rotation.

On the other hand, at the bottom of machined hole, abnormal electrical discharge would happen between the accumulated debris and the bottom surface of the electrode, which would increase the tool wear. Therefore, in machining methods without electrode rotation, the electrode failed to penetrate the work-piece with even much larger feeding range, as shown in Fig. 3.23.

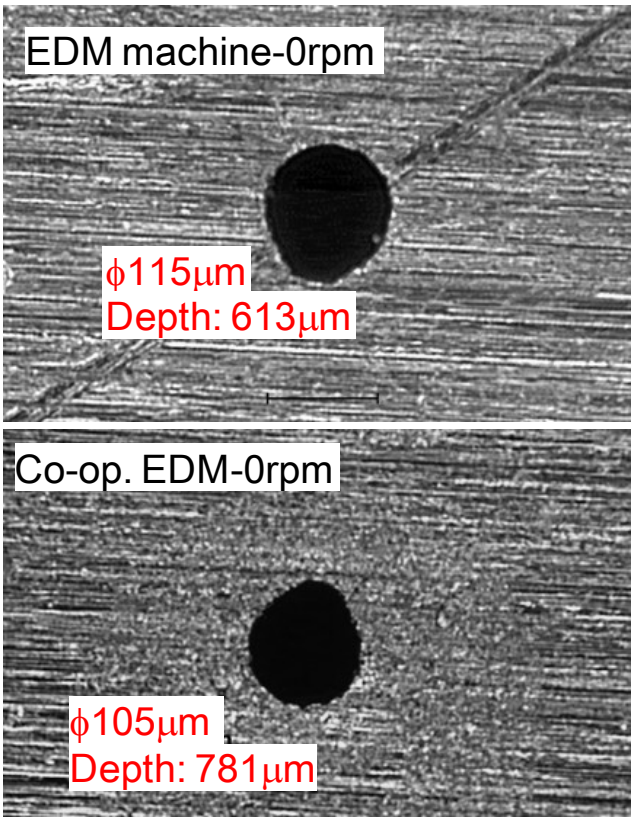

Fig. 3.25 Micro blind holes

3.5 Conclusion

In this chapter, in order to evaluated the effectiveness of fast positioning response of electrode, electrode rotation and their combination to the machining speed and accuracy in EDM, the developed maglev electrode driving actuator was applied to machine holes with various diameters and depths by EDM.

Before experimental machining, a co-operatively controlled EDM system was built for extending the positioning range of the electrode. In the co-operative EDM system, the prototype maglev electrode driving actuator was attached to a conventional EDM machine, and worked as a maglev local actuator (MLA). During machining, the MLA adjusted the light electrode speedily and accurately in a short range for maintaining a suitable gap between electrode and work-piece; the EDM machine fed the MLA in the machining direction in a large range for coarse positioning and for avoiding the saturation of the positioning stroke of the MLA. The co-operative EDM system realized as large positioning range as the conventional EDM machine, and as fast positioning response as the MLA.

A new attachment mechanism was design and fabricated for improve the clamping error of the electrode. With the new attachment mechanism, the rotational vibration of the electrode was decrease from more than 70μm to less than 10μm.

For machining ϕ0.5mm×4mm through holes, the co-operative EDM increased machining rate by 125% compared to conventional EDM machine, both without electrode rotation. In co-operative EDM, electrode rotating at 800rpm obtained the maximum machining rate, which was increased by 97% compared to co-operative EDM without electrode rotation.

For machining ϕ1mm×4mm through holes, the co-operative EDM increased machining rate by 337% compared to conventional EDM machine, both without electrode rotation. In co-operative EDM, electrode rotating at 600rpm obtained the maximum machining rate, which was increased by 22% compared to co-operative EDM without electrode rotation.

In order to machining micro hole with diameter less than 100μm and aspect ratio larger than 10, Ag-W micro electrodes were on-machined fabricated, with diameter of ϕ60μm and length of 2.4mm. Co-operative EDM system with electrode rotating at 800rpm succeeded in machining a 1mm deep micro through hole with diameter less than 100μm.

However, without electrode rotation, both conventional EDM machine and co-operative EDM system failed to machine a though hole on 1mm thick work-piece with the on-machine fabricated micro electrodes. The machining stopped after feeding 2.3mm, which was limited by the length of the on-machine fabricated electrode, 2.4mm.

Within the same feeding range of 2.3mm, the co-operative EDM without electrode rotation machined deeper hole in a shorter time compared to that of the conventional EDM. This indicated that the c-operative EDM obtained higher machining efficiency due to the faster positioning response compared to the conventional EDM machine.

In future work, attitude compensation of the electrode in radial and tilt directions for eliminating electrode clamping error and tapper error of machined hole will be experimentally investigated. The evaluation of jump motion, combination of rotation and orbital motion of electrode to the machining speed and accuracy will also be conducted.

Finally, the author will design and fabricate a new maglev actuator for another non-contact machining--laser beam machining. The development of the new maglev actuator will be introduced in the next chapter.

Chapter 4 Maglev lens driving actuator for LBM

4.1 Introduction

In laser beam machining, the machining speed and quality are very sensitive to the flow of the assist gas and the position of the focal point of the laser beam. Laser beam cutting is the most frequently performed material removal process in laser beam machining. In order to improve the cutting speed and the capability to remove molten material, as well as to save on the consumption of assist gas, a machining method that applies a suitable eccentricity between the axis of the laser beam (i.e. lens axis) and the axis of a convergent assist gas supply nozzle, which called off-axis control, was proposed for straight laser beam cutting, as shown in Fig. 4.1(a).

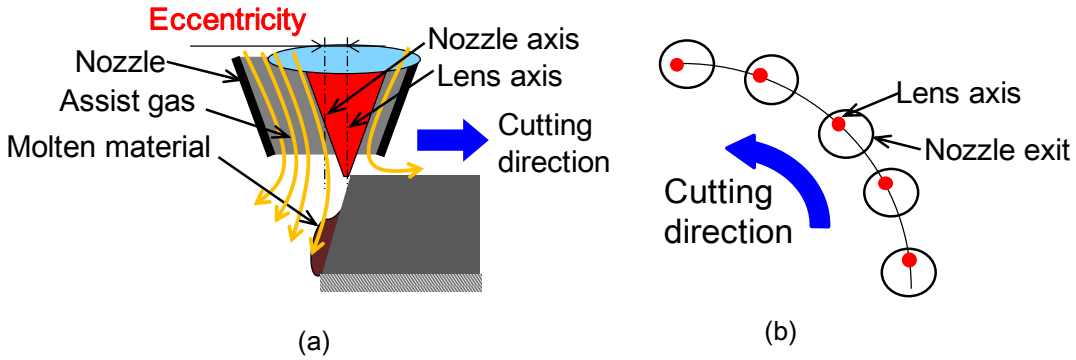

Fig. 4.1 Off-axis laser beam cutting realized by radial motion of the lens

The eccentricity between the laser beam axis and the convergent nozzle axis was manually adjusted for previous experiment [12]. However, real-time off-axis control of the lens has not been realized by a conventional LBM machine tool, which is required in two-dimensional laser beam cutting, as shown in Fig. 4.1(b), a relative displacement between the nozzle and the laser beam following the two-dimensional reference cutting trajectory should be generated.

On the other hand, the adjustment of the focal point of the laser beam, which can be realized by axial motion of the lens, is another of the more critical process parameters. The laser beam focal point, as shown in Fig. 4.2 (a. focused above, b. focused on and c. focused below the surface of the work-piece), can be

optimized according to the material and thickness of the work-piece to achieve the desired machining accuracy, speed and surface quality in various laser beam machining processes [15-19]. In previous researches, the focal point was manually adjusted and fixed during the machining process; however, high speed real-time adjustment of the focal point responding to changes in the thickness and material of the work-piece has not, so far, been reported.

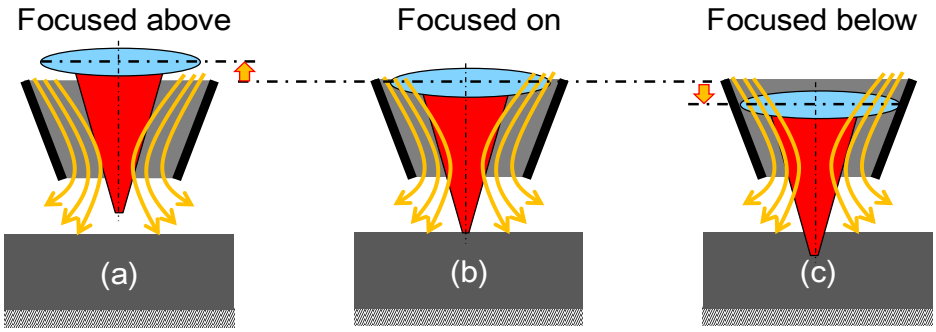

Fig. 4.2 Focal point adjustment realized by axial motion of the lens

Morimoto et al. developed a 2-DOF lens driving actuator, which realized maximum relative positioning range of ±0.5mm between a lens and a nozzle in two radial directions. The actuator was applied to two-dimensional off-axis laser beam cutting. Both the machining speed and quality were improved with the off-axis control [31]. However, the ±0.5mm positioning range of lens was not enough for further higher machining speed, and the laser beam focal point adjustment in axial direction could not be realized by the actuator.

In order to realize two-dimensional off-axis cutting and adjust the focal point speedily during various laser machining processes, a supplementary actuator which can drive the lens in three orthogonal directions is needed. The objective of this chapter is the realization of a compact maglev lens driving actuator which can drive the lens in both the axial and radial directions, and can be accommodated in the laser head of a conventional laser machine tool.

4.2 Principle and design of maglev lens driving actuator

4.2.1 Design specifications

Considering the future applications and the parameter settings used in preliminary laser beam machining experiments [31], the maximum displacements of the lens in the radial and axial directions were set to be no less than ±1mm and ±5mm, respectively; the tracking error was set to be less than 15μm and the bandwidths greater than 100Hz in all three orthogonal directions. Furthermore, sufficient positioning accuracy of the lens should be maintained under laser head acceleration of 20~40m/s^2 (2G~4G).

Due to the space restriction within the specified high power laser beam machine tool, within which the actuator will be accommodated in the laser head, the size of the actuator should be less than 125mm×125mm×125mm. The diameter and mass of the lens are 50.8mm (2 inch) and 50~100g, respectively.

4.2.2 Principle of actuator mechanism

For a maglev lens driving actuator, in order to realize a positioning range of ±1mm in radial direction and a positioning range of ±5mm in axial direction of the lens, the initial air gap of electromagnets should be no less than 1mm. During the full stroke reciprocating motion, the air gap would vary from 0mm to 2mm.

For a traditional core type electromagnet, the coil core made of magnetic material can concentrate the magnetic flux generated by coil, by that the generated attractive force to the target can be significantly increased. However, the repulsive force is hard to be generated.

Furthermore, the nonlinearity between the generated force, and the applied coil current and air gap is large for the traditional core type electromagnet, which makes the motion control become difficult, and a large current variation during reciprocating motion is required, this would increase power consumption and generate heat [50].

In order to realize a sufficiently large range of travel in three orthogonal directions and decrease the nonlinearity between input current and driving force, as well as generate sufficient driving force, a novel air core type

electro-magnetic driving unit was proposed for this work. Fig. 4.3 shows the proposed lens driving actuator. The lens for focusing the high energy laser beam is mounted in a large aperture in the center of the lens holder. Four electro-magnetic driving units are used to levitate and actuate the lens holder together with the attached lens.

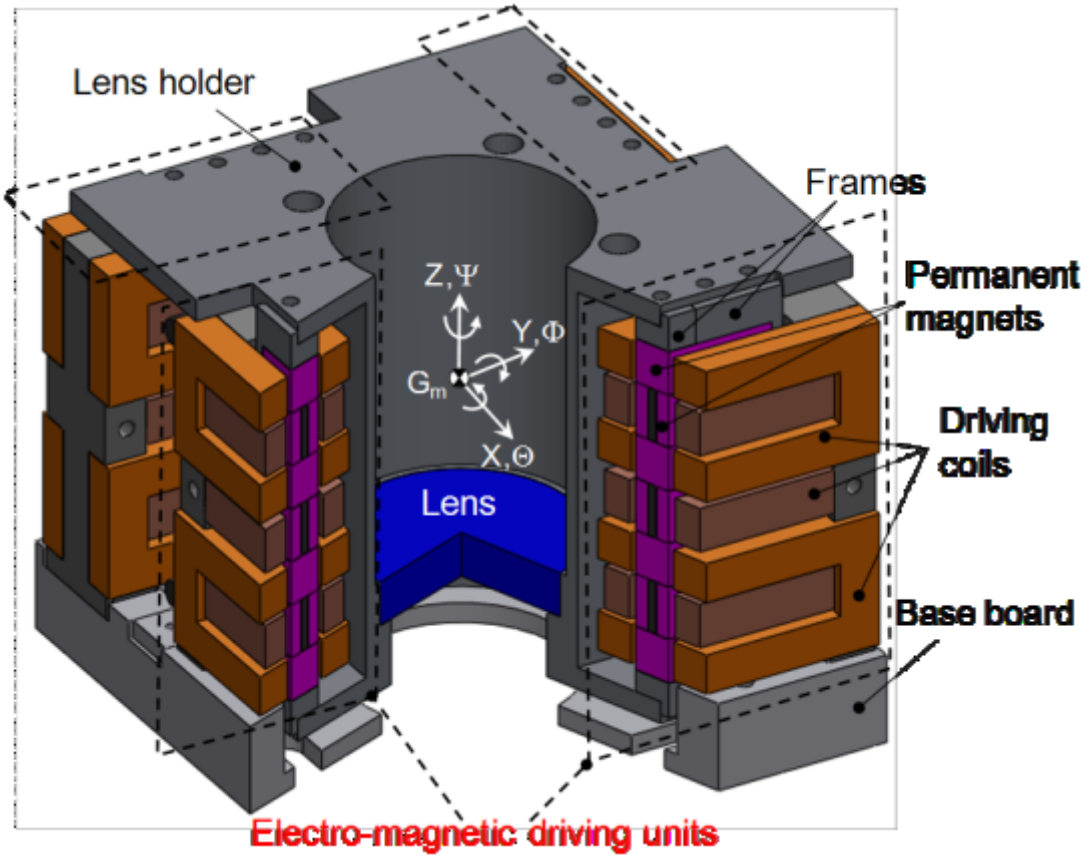

Fig. 4.3 Configuration of maglev lens driving actuator

4.2.3 Electro-magnetic driving unit

Fig. 4.4(a) shows the configuration of one electro-magnetic driving unit. The driven target of the unit consists of four permanent magnet (PM) blocks and six small PM plates, with three pieces of pure iron sandwiched between the three pairs of oppositely magnetized PM plates. The magnetization directions of the PMs were designed according to the Halbach PM array [51], as shown in Fig. 4.4(a). Compared to traditional Halbach PM array, the modified PM array can generate enhanced magnetic fields at both sides of the driven target, Fig. 4.4(b)

shows the magnetic flux generated by the PM array.

Four serially-connected rectangular air core radial coils and three serially-connected rectangular air core thrust coils are fixed on the actuator base board and are used to actuate the driven target in both the radial and thrust directions. Coreless rectangular type coils were chosen for the following reasons: both attractive and repulsive forces can be generated; the nonlinearity of the force generated, which depends on the applied current and the gap between the coils and the PMs, is small; the air core part of the coils can be effectively utilized to realize a spatial-cross-arrangement of the driven target and the coils, therefore, a very compact size of the unit can be realized, as shown in Fig. 4.4(a).

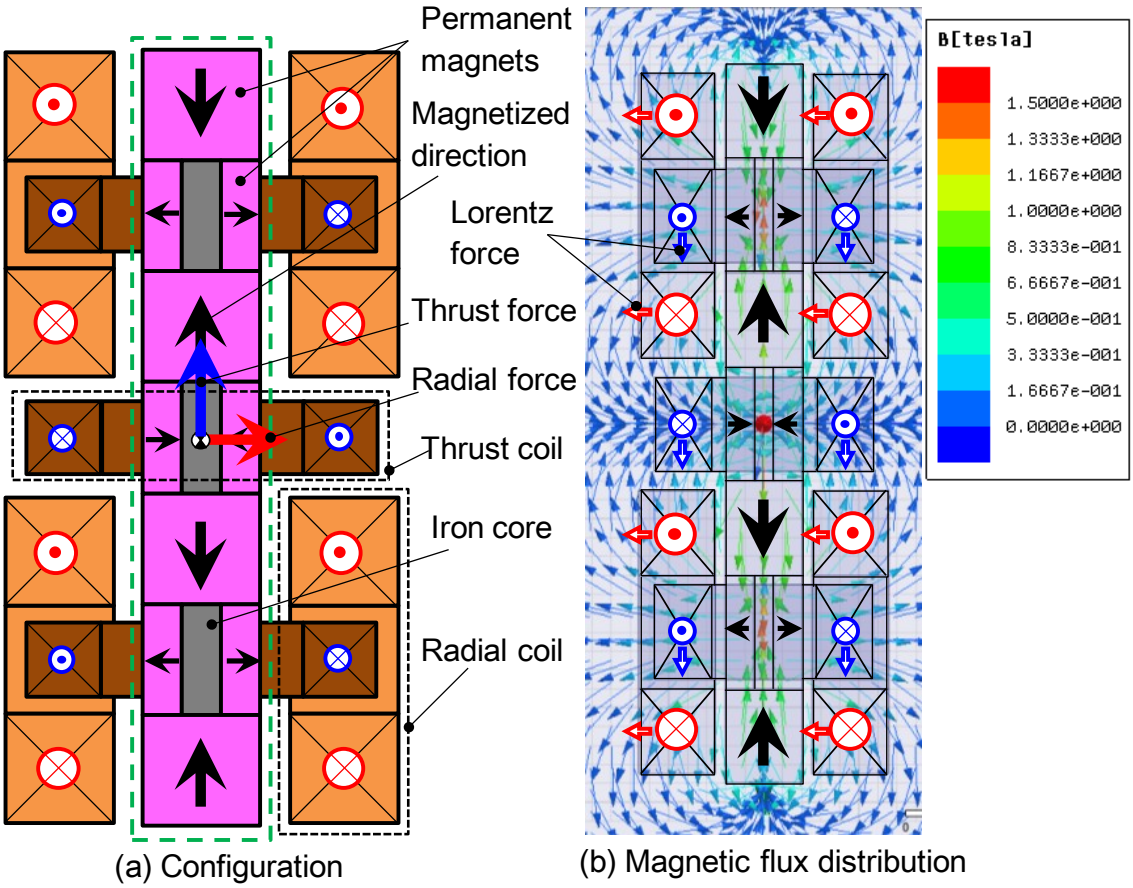

Fig. 4.4 Electro-magnetic driving unit

When applying current to the fixed radial and thrust coils, as shown in Fig. 4.4(b), according to the direction of the magnetic flux flow generated by the PM

array and the direction of the applied current flow, leftward Lorentz force will be generated on radial coils and downward Lorentz force will be generated on thrust coils. Since the coils are fixed on the base board, resultant radial and thrust reaction forces will be generated to the target, and act on the gravity center, as shown in Fig. 4.4 (a). By reversing the direction of applied current, the direction of generated driving force can be reversed consequently.

4.2.4 Displacement measuring system

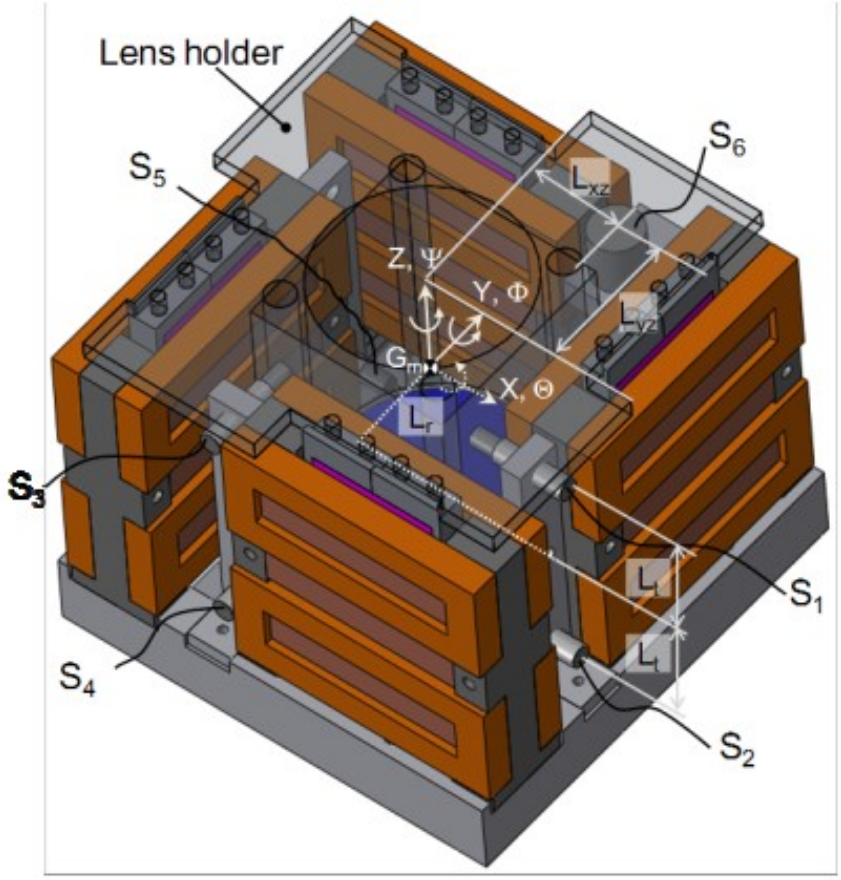

Fig. 4.5 Arrangement of displacement sensors

The displacement of the lens holder in the X-, Y-, Θ-, Φ- Ψ- and Z-directions are measured by six non-contact displacement sensors (S_1~S_6), the sensor number is minimum for measuring the displacement of the lens holder in 6-DOF. Considering the space limitations of the lens holder, S_1~S_6 were offset from the orthogonal axis, as shown in Fig. 4.5. Such an arrangement realized sufficiently

compact of the actuator, however, the displacement of the lens holder could not be measured directly, so that the measurement accuracy may be affected by the assembly error.

According to the arrangement of the sensors shown in Fig. 4.5, the relationship between the displacement measured by each sensor (D_1~D_6) and the displacement of the center of gravity of the lens holder G_m (x, y, z, θ, ϕ, ψ) from the origin can be expressed as follows:

$$\begin{bmatrix} D_1 \\ D_2 \\ D_3 \\ D_4 \\ D_5 \\ D_6 \end{bmatrix} = \begin{bmatrix} -1 & 0 & 0 & 0 & -L_t & -L_r \\ -1 & 0 & 0 & 0 & L_t & -L_r \\ 0 & 1 & 0 & -L_t & 0 & -L_r \\ 0 & 1 & 0 & L_t & 0 & -L_r \\ 1 & 0 & 0 & 0 & -L_t & -L_r \\ 0 & 0 & 1 & -L_{yz} & -L_{xz} & 0 \end{bmatrix} \begin{bmatrix} x \\ y \\ z \\ \theta \\ \varphi \\ \psi \end{bmatrix} \quad \cdots\cdots(4.1)$$

Where, L_t, L_r, L_{xz}, and L_{yz} are the distances from each sensor to the center of gravity of the lens holder; therefore, the displacement of the center of gravity of the lens holder in each direction can be calculated from:

$$\begin{bmatrix} x \\ y \\ z \\ \theta \\ \varphi \\ \psi \end{bmatrix} = \begin{bmatrix} -0.5 & 0 & 0 & 0 & 0.5 & 0 \\ 0 & -0.5 & 0.5 & 0.5 & -0.5 & 0 \\ -L_{xz}/2L_t & L_{xz}/2L_t & L_{yz}/2L_t & -L_{yz}/2L_t & 0 & 1 \\ 0 & 0 & -1/2L_t & -1/2L_t & 0 & 0 \\ -1/2L_t & -1/2L_t & 0 & 0 & 0 & 0 \\ 0 & -1/2L_r & 0 & 0 & -1/2L_r & 0 \end{bmatrix} \begin{bmatrix} D_1 \\ D_2 \\ D_3 \\ D_4 \\ D_5 \\ D_6 \end{bmatrix} \quad \cdots(4.2)$$

4.3 Fabricated maglev lens driving actuator

4.3.1 Prototype maglev lens driving actuator

Fig. 4.6 shows one assembled driving coil unit. Each radial coil is 252 turns and each thrust coil is 216 turns, the full size of one driving coil set is 74mm×33mm×79mm. The driven coil unit will be fixed to a base board for driving the target. Fig. 4.7 shows one assembled driven target. The sizes of the PM blocks and PM plates are 8mm×10mm×35mm and 3mm×12mm×35mm, respectively, the red arrows indicate the magnetized direction. The driven target will be assembled into the center slot of the coil unit, and then amounted to a lens holder; the initial gap between the driven target and the coils is 1.1mm.

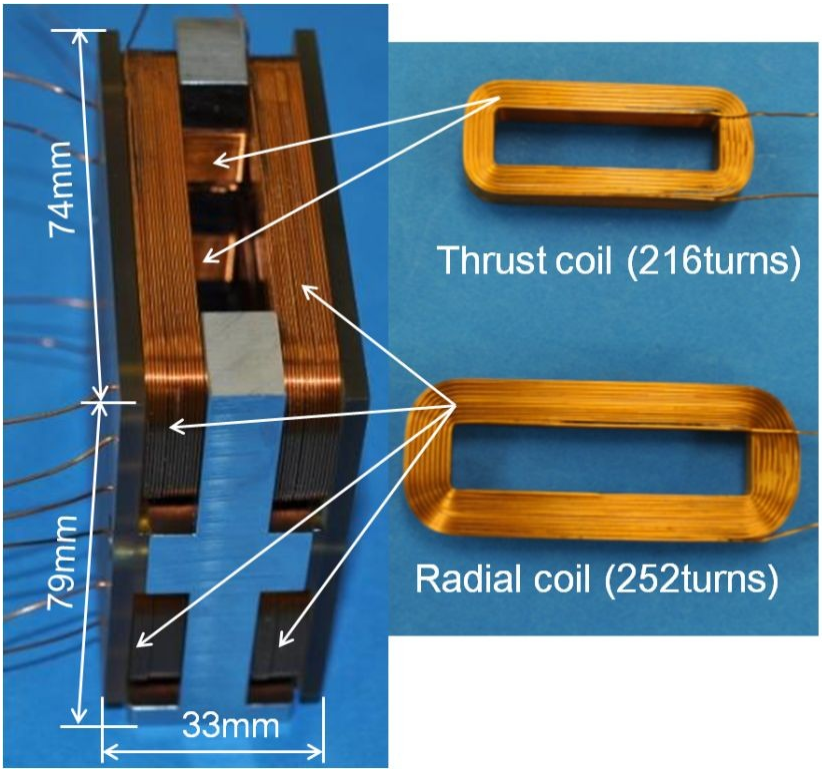

Fig. 4.6 Assembled driving coil unit

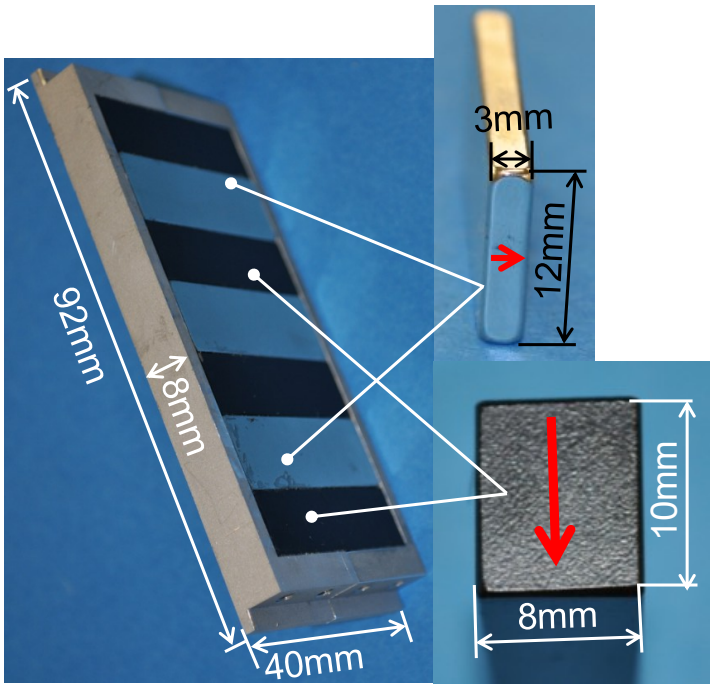

Fig. 4.7 Assembled driven target

Fig. 4.8(a) shows the assembled prototype maglev lens driving actuator, the

full size is 124mm×124mm×101mm, and the total mass is 6kg including all the attachments. Fig. 4.8(b) shows the lens holder with one driven target. In order to obtain sufficient stiffness and light weight, the lens holder was made of duralumin. The mass of the moving part (including the lens holder, the lens and the four driven targets, etc.) is 1.12kg. The travel range of the lens holder is ±1mm in the X- and Y-directions, and ±5mm in the Z-direction.

For avoiding positioning error of laser beam focal point in three orthogonal directions and for realizing stable levitation of lens holder, the rotary and tile motions of the lens holder should be controlled. In order to control the rotary motion of the lens in the Ψ-direction, the four driving units are offset from the X- and Y-axes and arranged symmetrically around the Z-axis, as shown in Fig. 4.8. The radial and thrust forces imparted to the lens holder from each driving unit are represented by F_{r1}, F_{t1}, F_{r2}, F_{t2}, F_{r3}, F_{t3}, F_{r4}, F_{t4}, respectively.

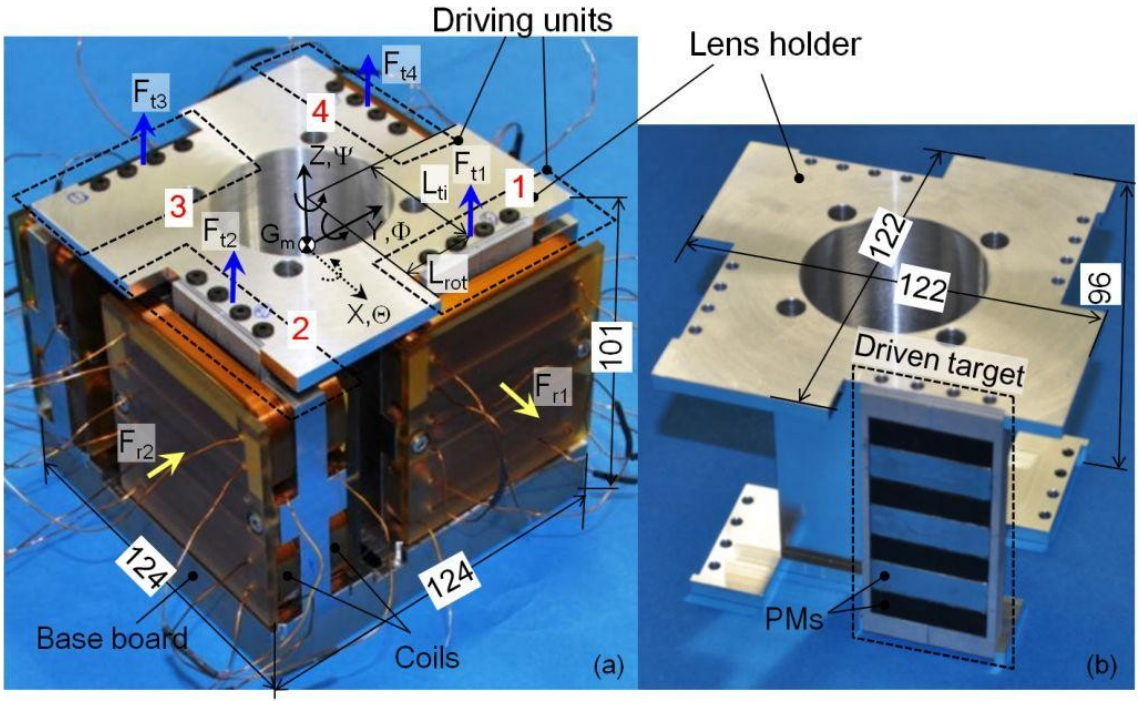

Fig. 4.8 Prototype maglev lens driving actuator

4.3.2 Driving force measurement

The relationship between the applied current and the forces generated in the

radial and thrust directions of an electro-driving unit were both simulated and experimentally measured. The simulation was done using FEM (Finite element method) software (Ansoft Maxwell 3D, Ver.12.0), and the experimental results were measured using a load cell (LUR-A-500NSA1, KYOWA Electronic Instruments CO., LTD.).

Fig. 4.9 shows the experimental setup for measuring the radial driving force generated to one driven target. The driving coil unit was fixed on a table, the driving target was connected to the load cell and hanging in the slot of the driving coil unit, the load cell together with the driven target was supported by a positioning stage.

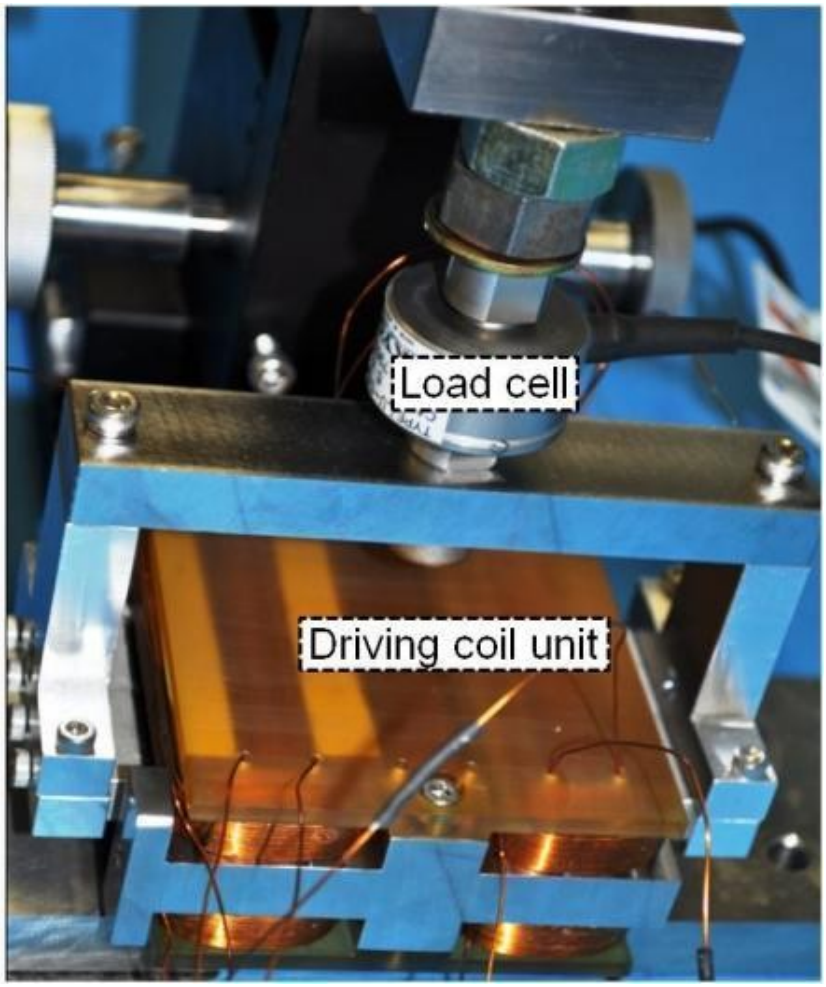

Fig. 4.9 Driving force measurement setup

By applying different current into the radial coils, the generated radial force to the driven target was measured by the load cell and the results were recorded. By changing the arrangement of the components, the thrust force also was measured.

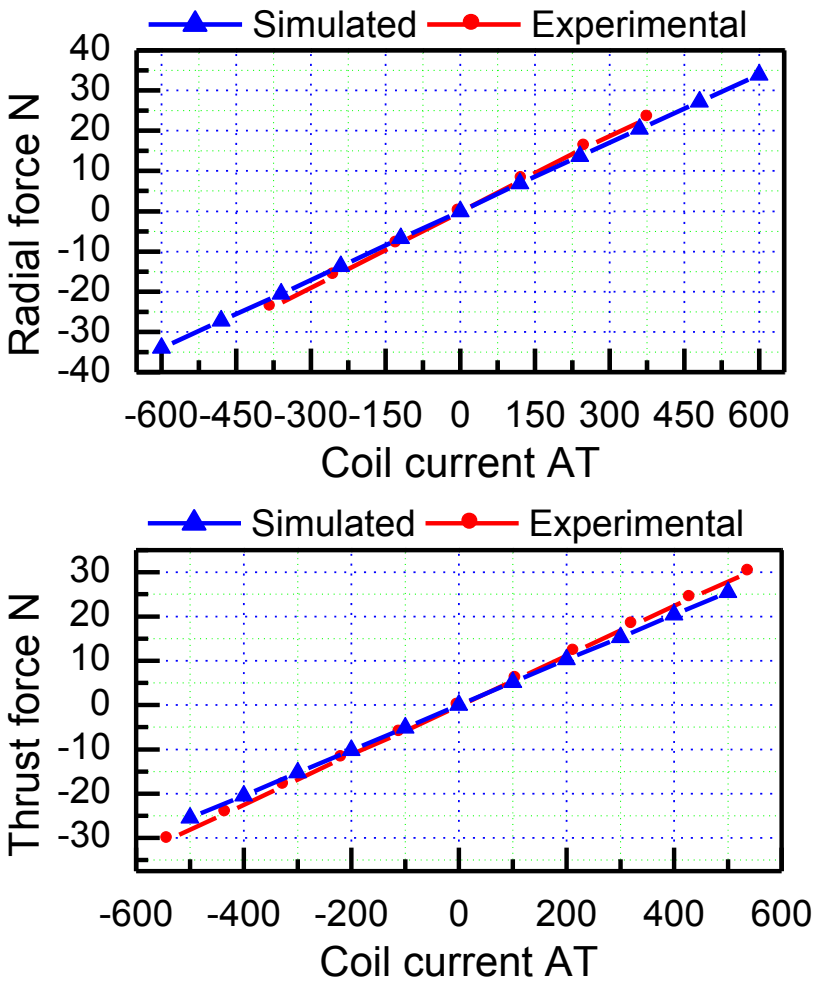

Fig. 4.10 Relationship between applied current and generated force

Fig. 4.10 shows the relationship between the applied current and generated force in both radial and thrust directions. The results show good agreement between the simulated and experimental results, and the relationships between the forces generated and the applied current are fairly linear.

Since the range of travel of the driven target in the thrust direction is much larger than that in the radial direction, the dependency of the force generated on the thrust bias displacement of the target was investigated. Fig. 4.11 shows the relationship between the bias displacement of the target and the magnetic

driving force generated in the thrust direction. Since the force generated depends on the thrust bias displacement of the target, compensation for this was implemented in the control system.

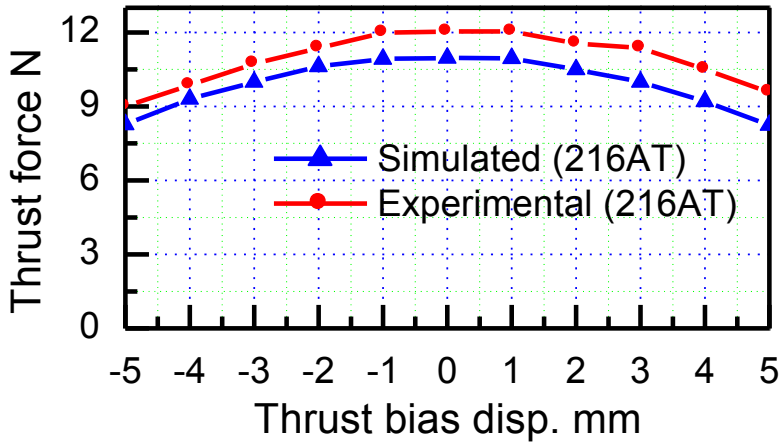

Fig. 4.11 Driving force variation depending on thrust bias displacement

4.3.3 Driving scheme

According to the results in Fig. 4.10 and Fig. 4.11, the radial and thrust driving forces imparted to the moving parts of each electro-magnetic driving unit can be calculated as:

$$F_{ri}=K_{Ir}\times I_{ri}\ (i=1,2,3,4) \quad \cdots\cdots (4.3)$$

$$F_{tj}=K_{It}(z)\times I_{tj}\ (j=1,2,3,4) \quad \cdots\cdots (4.4)$$

Where, K_{Ir} (15.81, N/A) and K_{It}(z) (12.10-0.13z^2, N/A) are the current-force coefficients in the radial and thrust directions, respectively, z is the thrust bias displacement of the lens holder from the origin, I_{ri} and I_{ti} are the respective currents applied to the radial and thrust coils of each unit, and i and j are the subscripts for the electro-magnetic driving units indicated in Fig. 4. 8.

The radial force F_{ri} is used to drive the lens holder in the X-, Y- and Ψ-directions, and the thrust force F_{tj} is used to drive the lens holder in the Θ-, Φ-, Z-directions. The points in the x-y plane at which the thrust forces act are at L_{rot} (25mm) and L_{ti} (45mm), as shown in Fig. 4.8, therefore, the resultant driving

forces and driving torques in each direction can be calculated as follows:

$$\begin{bmatrix} F_x \\ F_y \\ T_\psi \end{bmatrix} = K_{Ir} \begin{bmatrix} 1 & 0 & 1 & 0 \\ 0 & 1 & 0 & 1 \\ -L_{rot} & L_{rot} & L_{rot} & -L_{rot} \end{bmatrix} \begin{bmatrix} I_{r1} \\ I_{r2} \\ I_{r3} \\ I_{r4} \end{bmatrix} \quad \text{(4.5)}$$

$$\begin{bmatrix} F_z \\ T_\theta \\ T_\varphi \end{bmatrix} = K_{It}(z) \begin{bmatrix} 1 & 1 & 1 & 1 \\ L_{rot} & -L_{ti} & -L_{rot} & L_{ti} \\ -L_{ti} & -L_{rot} & L_{ti} & L_{rot} \end{bmatrix} \begin{bmatrix} I_{t1} \\ I_{t2} \\ I_{t3} \\ I_{t4} \end{bmatrix} \quad \text{(4.6)}$$

Compensation for interference between the movements in the X-, Y- and Ψ-directions was implemented by applying suitable coil currents to each electro-magnetic driving unit. Similarly, compensation was applied for the interference between the movements in the Θ-, Φ- and Z-directions. For example, for the interference between the movement generated by the thrust forces (Θ-, Φ- and Z-directions), when the lens holder is driven to move in the Θ-direction only, the currents applied to the thrust coil of each unit are set as:

$$\begin{bmatrix} I_{t1} \\ I_{t2} \\ I_{t3} \\ I_{t4} \end{bmatrix} = \begin{bmatrix} L_{rot}/L_{ti} \\ -1 \\ -L_{rot}/L_{ti} \\ 1 \end{bmatrix} i_\theta \quad \text{(4.7)}$$

Then the resultant torques and force generated by the applied currents in the Θ-, Φ- and Z-directions are:

$$\begin{bmatrix} F'_z \\ T'_\theta \\ T'_\varphi \end{bmatrix} = K_{It}(z) \begin{bmatrix} 1 & 1 & 1 & 1 \\ L_{rot} & -L_{ti} & -L_{rot} & L_{ti} \\ -L_{ti} & -L_{rot} & L_{ti} & L_{rot} \end{bmatrix} \begin{bmatrix} \frac{L_{rot}}{L_{ti}} \\ -1 \\ -\frac{L_{rot}}{L_{ti}} \\ 1 \end{bmatrix} i_\theta = 2K_{It}(z) i_\theta \begin{bmatrix} 0 \\ \frac{L_{rot}^2 + L_{ti}^2}{L_{ti}} \\ 0 \end{bmatrix} \quad \text{(4.8)}$$

The resultant torque in the Φ-direction T'_ϕ and resultant force in the Z-direction F'_z are 0; thus, there is no interference with the positioning in the Φ- and Z-directions.

4.3.4 Control system

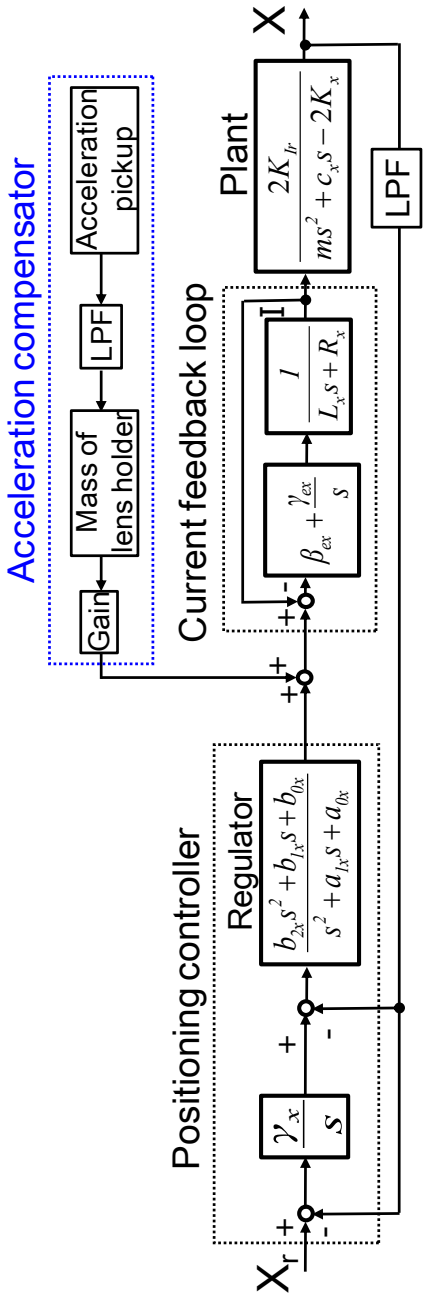

Fig. 4.12 Control system in the X-direction

In the prototype maglev lens driving actuator, the displacement of the lens holder in each direction was independently controlled. The controller algorithm was almost the same as that adopted in the maglev electrode driving actuator explained in chapter 2. Fig. 4.12 shows a control system block diagram in the X-direction, controllers in Y-, Z-, Θ-, Φ- and Ψ-directions are almost the same as

that of the X-direction.

The acceleration compensator was only adopted in the X- and Y-directions, which was used for compensating the disturbance force generated by external acceleration to the maglev lens driving actuator in radial direction during 2-DOF high speed laser cutting machining. The effectiveness of the acceleration compensator will be introduced in section 4.4.4.

Table 4.1 Controller parameters in the X-, Θ-, Z- and Ψ-directions

X – direction		Θ – direction		Z – direction		Ψ – direction	
γ_x	$3.5\text{x}10^2$	γ_θ	$2.5\text{x}10^2$	γ_z	$2.0\text{x}10^2$	γ_ψ	$1.6\text{x}10^2$
a_{1x}	$4.2\text{x}10^3$	$a_{1\theta}$	$3.3\text{x}10^3$	a_{1z}	$1.4\text{x}10^3$	$a_{1\psi}$	$2.5\text{x}10^3$
a_{0x}	$7.2\text{x}10^6$	$a_{0\theta}$	$4.5\text{x}10^6$	a_{0z}	$1.7\text{x}10^6$	$a_{0\psi}$	$3.4\text{x}10^6$
b_{2x}	$1.1\text{x}10^5$	$b_{2\theta}$	$2.3\text{x}10^3$	b_{2z}	$-4.1\text{x}10^3$	$b_{2\psi}$	$1.0\text{x}10^3$
b_{1x}	$2.6\text{x}10^8$	$b_{1\theta}$	$5.2\text{x}10^6$	b_{1z}	$1.7\text{x}10^7$	$b_{1\psi}$	$3.6\text{x}10^6$
b_{0x}	$6.7\text{x}10^{10}$	$b_{0\theta}$	$1.1\text{x}10^9$	b_{0z}	$1.6\text{x}10^9$	$b_{0\psi}$	$7.1\text{x}10^8$
γ_{ex}	50.0	$\gamma_{e\theta}$	20.0	γ_{ez}	20.0	$\gamma_{e\psi}$	50.0
β_{ex}	$6.0\text{x}10^3$	$\beta_{e\theta}$	$6.0\text{x}10^3$	β_{ez}	$6.0\text{x}10^3$	$\beta_{e\psi}$	$6.0\text{x}10^3$

Table 4.2 Identified model parameters in the X-, Θ-, Z- and Ψ-directions

X – direction			Θ – direction			Z – direction			Ψ – direction		
L_x	$1.5\text{x}10^{-3}$	H	L_θ	$5.2\text{x}10^{-3}$	H	L_z	$5.2\text{x}10^{-2}$	H	L_ψ	$1.5\text{x}10^{-3}$	H
R_x	14.8	Ω	R_θ	7.6	Ω	R_z	7.6	Ω	R_ψ	14.8	Ω
m	1.12	kg	J_θ	$2.3\text{x}10^{-3}$	Kg. m²	m	1.12	kg	J_ψ	$2.7\text{x}10^{-3}$	Kg. m²
c_x	10	N/(m/s)	c_θ	0	N.m/(rad/s)	c_z	10	N/(m/s)	c_ψ	0	N.m/(rad/s)
k_{Ix}	28.7	N/A	$k_{I\theta}$	1.4	N.m/A	k_{Iz}	46.7	N/A	$k_{I\psi}$	5.5	N.m/A
k_x	$4.4\text{x}10^3$	N/m	k_θ	$3.9\text{x}10^{-2}$	N.m/rad	k_z	0	N/m	k_ψ	$3.9\text{x}10^{-2}$	N.m/rad

The control parameters in the X-, Θ-, Z- and Ψ- directions, as shown in Table 4.1, were set through trial and error using simulation and experiments, and Table 4.2 shows the model parameters in the X-, Θ-, Z- and Ψ- directions. Here, the inductance and resistance of the coil *L* and *R*, and the mass of the moving parts *m* were measured directly. The inertia *J* was calculated by model software (SolidWorks). The damping *c*, stiffness *K* and current-force coefficient K_I of the

magnetic bearing were identified using the measured frequency responses of the maglev lens driving actuator. Moreover, the parameter values in the Y- and Φ-directions, which are not shown in the tables, are almost the same as those in the X- and Θ-directions.

4.4 Experimental results

4.4.1 Experiment setup

The displacement of the lens holder in the X-, Y-, Θ-, Φ- and Ψ-directions were measured using five eddy current displacement sensors (S_1~S_5, PU-05, AEC Corp., measurement range 2mm, resolution 0.5μm). The displacement of the lens holder in the Z-direction was measured by another type of eddy current displacement sensor (S_6, PU-14, AEC Corp.), as shown in Fig. 4.5. In order to extend the measurement range of S_6 from the nominal value of 6mm to the required one of 10mm, the nonlinear region of the sensor output is used. Fig. 4.13 shows the calibration curve of the displacement sensor. When the gap between the probe and the sensor target is larger than 6mm the sensitivity decreases, consequently decreasing the resolution.

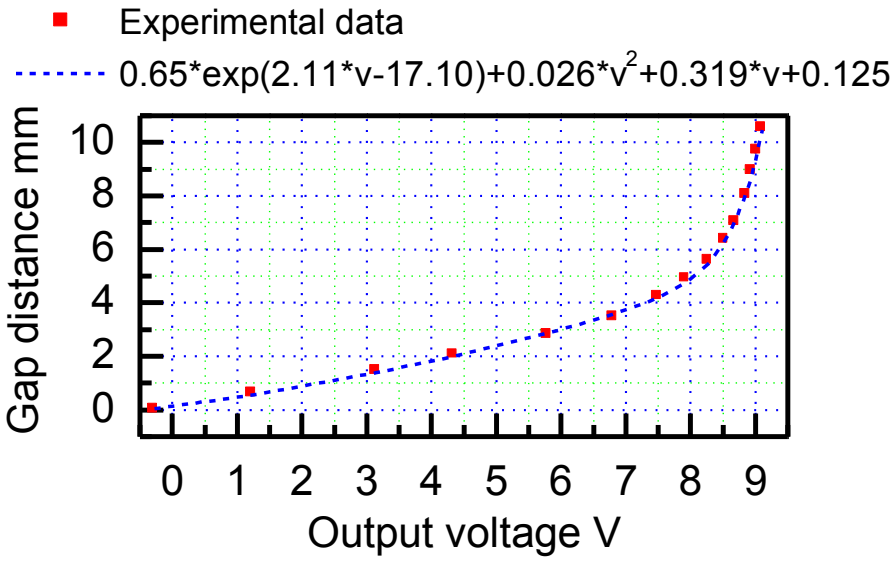

Fig. 4.13 Calibration of the PU-14 eddy current sensor

A digital signal processor (DS1103, dSPACE Japan Corp. sampling rate 10kHz) was used to realize a digital controller for the displacement and motion of the lens holder, and the frequency response characteristics of the lens holder were measured using a frequency response analyzer (FRA 5095, NF Corp.). Eight power operational amplifiers were used to supply the driving voltage to the radial and thrust coils (PA12, APEX Microtechnology Corp., voltage supply range ±10V to ±50V, output current ±15A peak).

4.4.2 Full positioning stroke, resolution and bandwidth

Without supplying power to the actuator, the lens holder was located on the base board, which is more than 5mm below the origin of the coordinate system. The lens holder could be easily and steadily levitated by the controller.

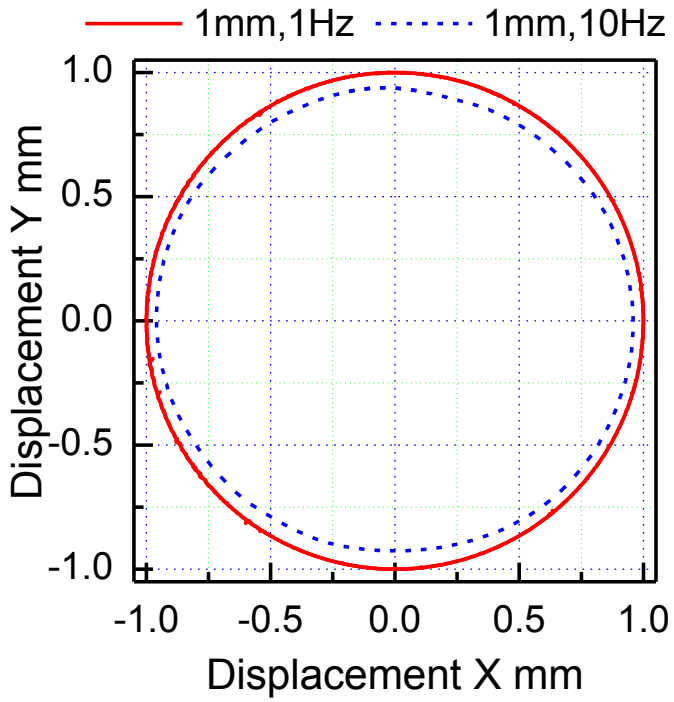

Fig. 4.14 Full stroke circular motion in the X-Y plane

Fig. 4.14 shows the movement, driven by the maglev actuator, of the lens holder in a full stroke (±1mm) circular motion in the X-Y plane at frequencies of 1Hz and 10Hz. Fig. 4.15 shows the full stroke of the lens holder of ±5mm in the axial direction at 1Hz.

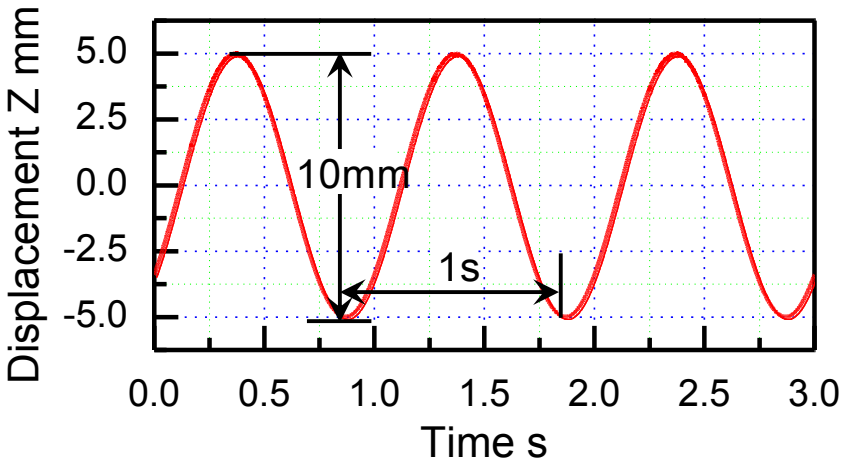

Fig. 4.15 Full stroke in the Z-direction

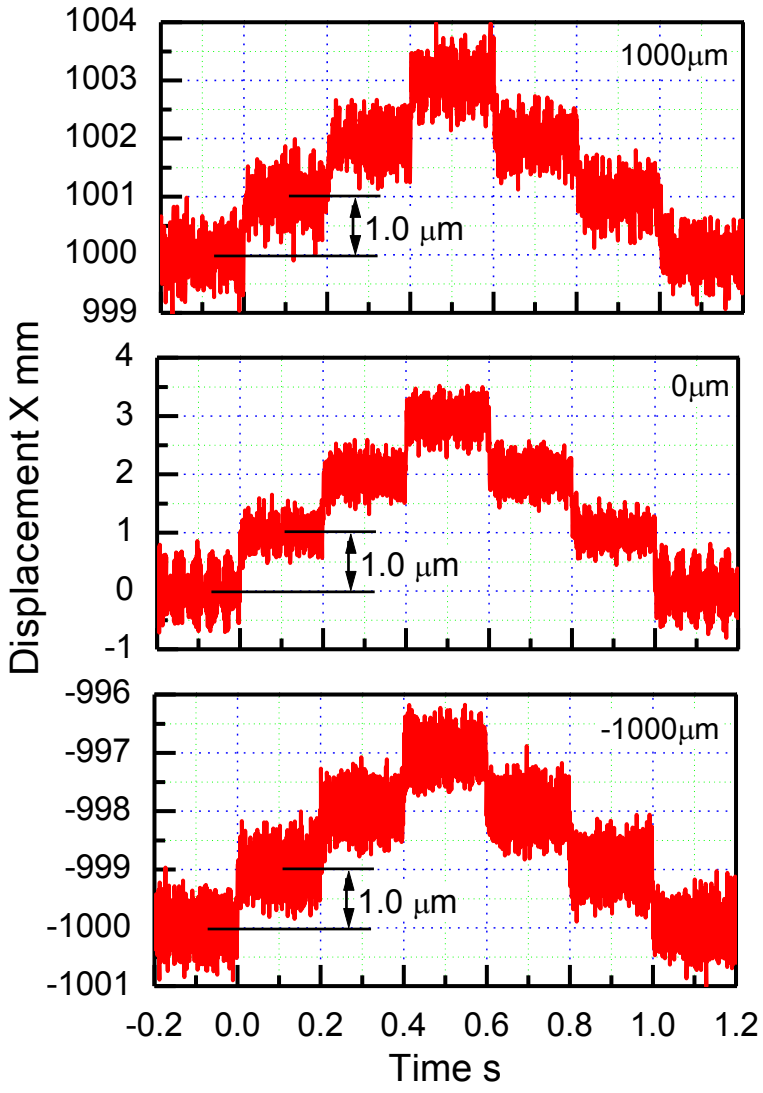

Fig. 4.16 Positioning resolution in the X-direction

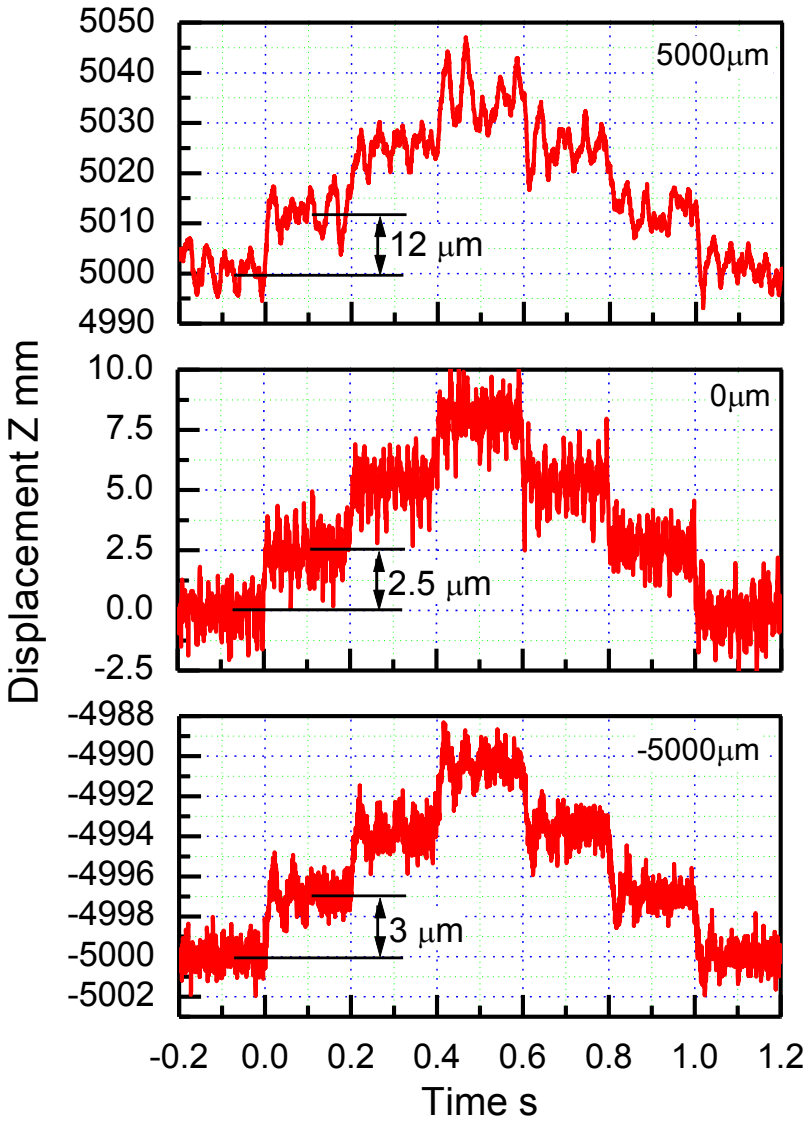

Fig. 4.17 Positioning resolution in the Z-direction

Fig. 4.16 shows the positioning resolution of the lens holder in the X-direction at the 1mm, 0mm and -1mm positions, respectively. The results indicate that the actuator has a positioning resolution of 1μm over the whole range.

Fig. 4.17 shows the positioning resolution of the lens holder in the Z-direction to be 3.0μm at -5mm, 2.5μm at 0mm and 12μm at 5mm. The decrease in resolution at 5mm is due to the increased distance from the sensor to the target.

The bandwidth of the actuator was measured when the lens holder was levitated at the initial position, the amplitude of the input signal was 10μm. Fig. 4.18 shows the results of measurements of the bandwidths of the actuator in the X- and Z-directions, which are 160Hz, and 105Hz, respectively. The results for the Y-direction, which are not shown, are almost identical to those for the X-direction.

According to the experimental results, the prototype maglev lens actuator achieved the design specifications. It realized full positioning stroke of ±1mm in two radial directions and full positioning stroke of ±5mm in the axial direction, with tracking error less than 15μm in the whole positioning range and bandwidth greater than 100Hz in all the three orthogonal directions.

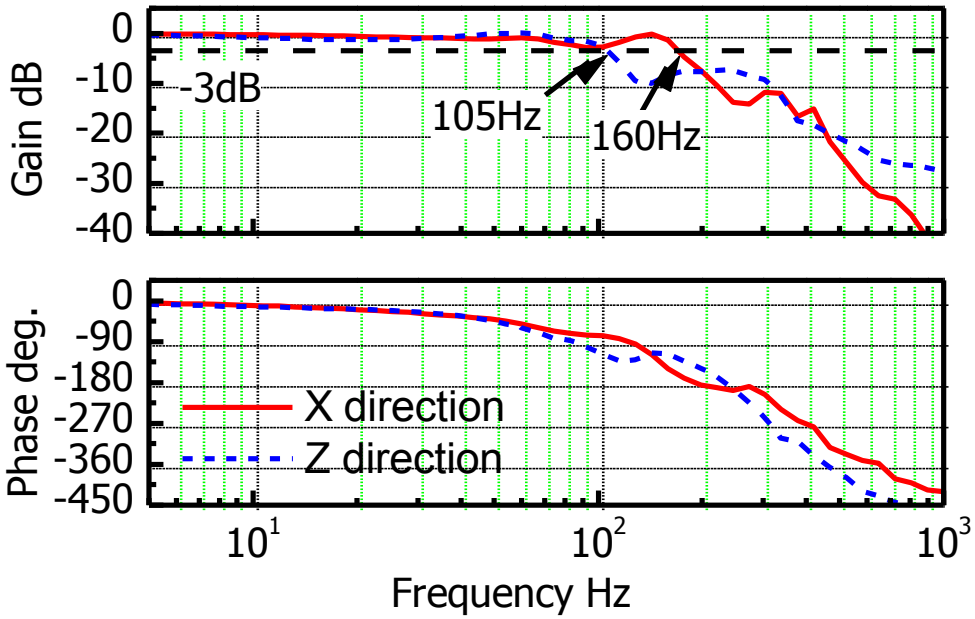

Fig. 4.18 Bandwidth in the X- and Z-directions

4.4.3 Motion interference

Step response experiments were conducted to evaluate the effectiveness of compensation for the interference between the movements in different directions. In the experiments, a step signal was input into one direction, positioning errors in the other directions during the step operation were recorded.

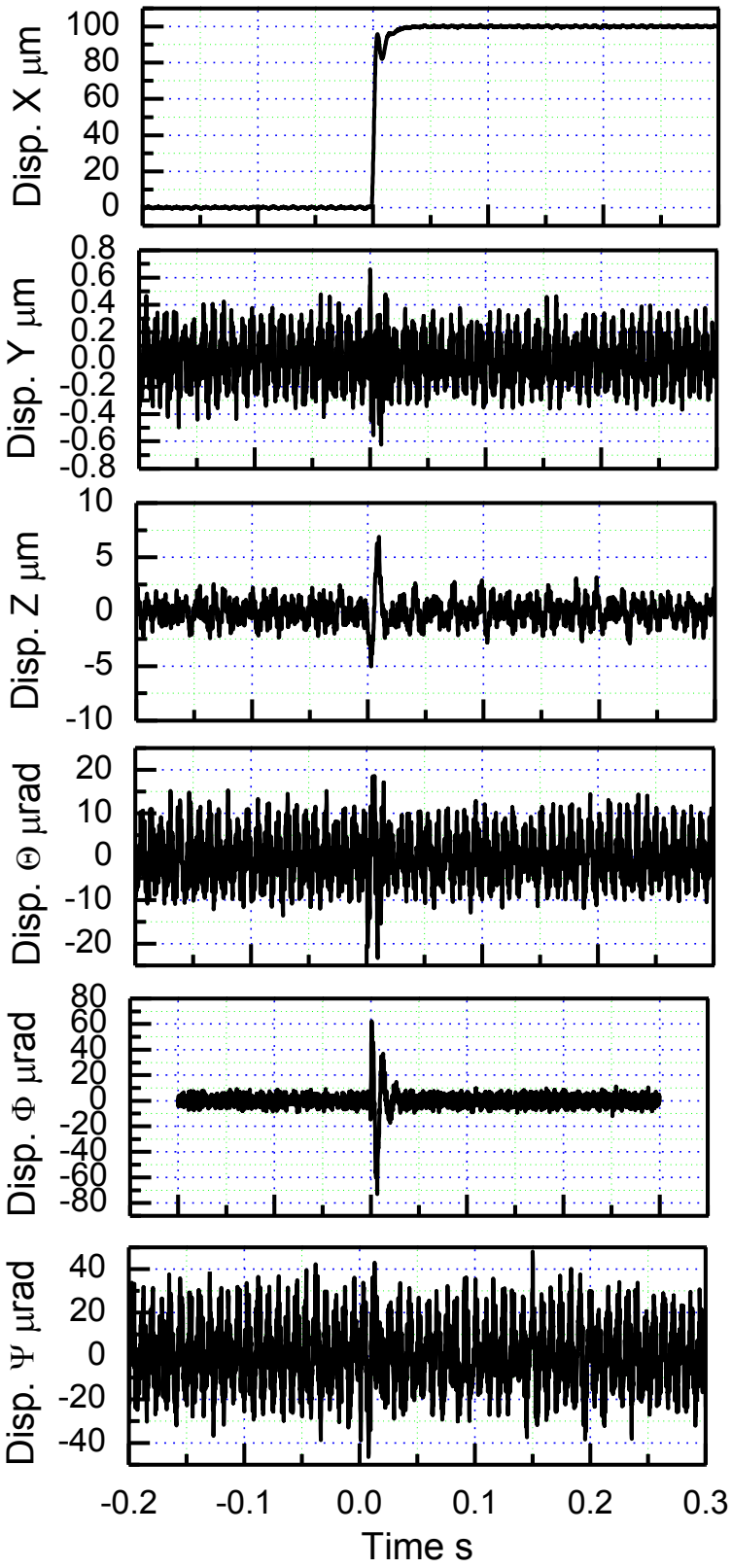

Fig. 4.19 Interference from step response in the X-direction

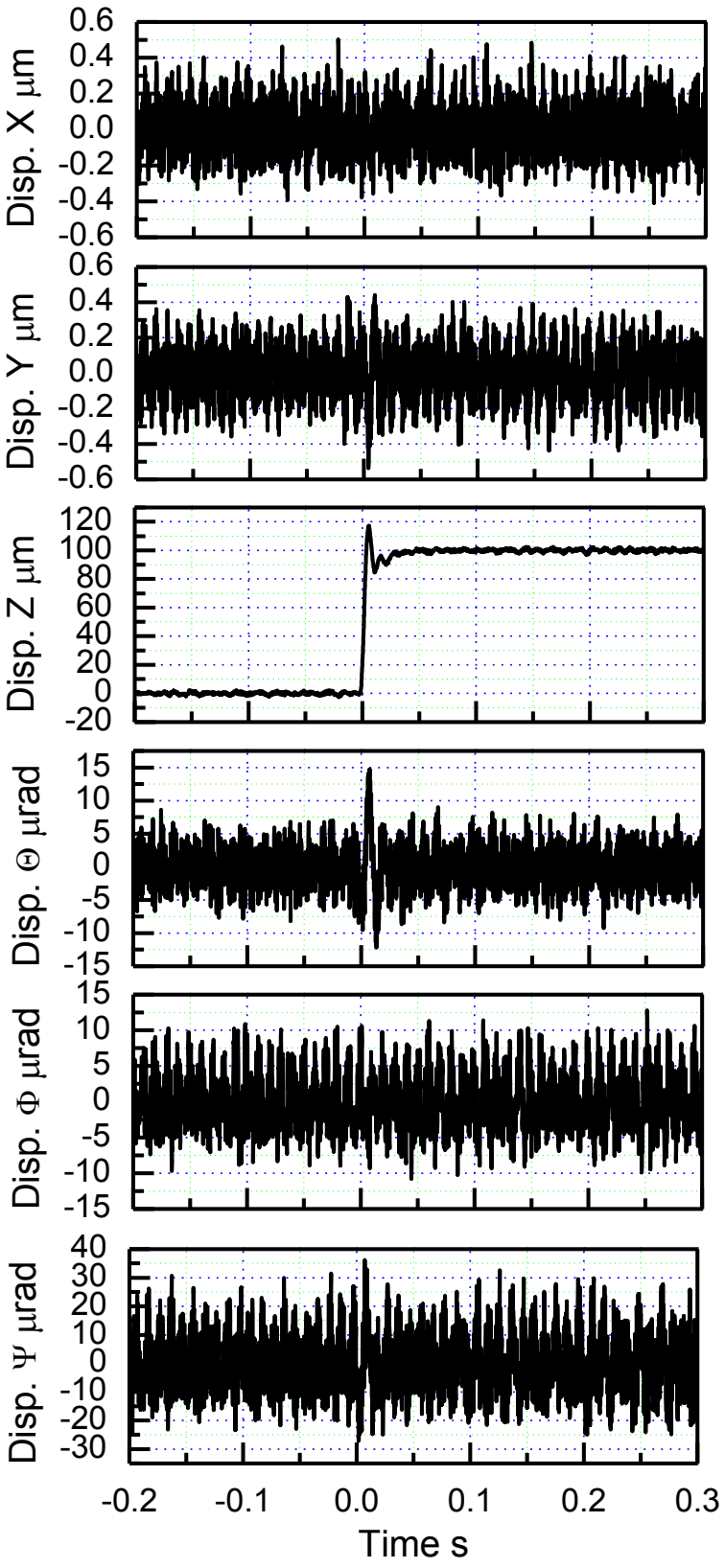

Fig. 4.20 Interference from step response in the Z-direction

Fig. 4.19 and Fig. 4.20 show the experimental results. When a 100μm step was applied to the holder in the X-direction, a positioning error of just ±60μrad was observed in the Φ-direction, as shown in Fig. 4.19. The displacement of the lens holder in the Φ-direction is measured by sensors S_1 and S_2, and the distance between these is 60mm ($2\times L_t$), as shown in Fig. 4.5. According to Eq. 4.2, a positioning error of ±60μrad in the Φ-direction is equivalent to positioning errors of ±1.8μm at S_1 and S_2, which is acceptable considering the positioning accuracy in the radial direction. When a 100μm step was applied to the holder in the Z-direction, no obvious positioning error was observed in all the other five directions, as shown in Fig. 4.20.

The results for the Y-direction, which are not shown, are almost identical to those for the X-direction. The experimental results indicate that compensation for the interference between movements in the different directions was successfully accomplished.

4.4.4 Vibration test

During high speed laser plate cutting machining [42], the lens driving actuator was accelerated to 20~40m/s^2 in the radial direction. The external acceleration would generate disturbance force to the levitated lens holder. Vibration test was conducted in order to verify the positioning performance of the actuator in the radial direction under high acceleration conditions.

Fig. 4.21 shows the experiment setup for vibration test in the X-direction. The maglev lens driving actuator was attached to the load table of a vibration machine (230/SA2M, IMV Corporation). During the test, the lens holder was levitated, and then the actuator was vibrated in the X-direction with high acceleration. This introduced a positioning error into the lens holder.

The acceleration of the load table was measured using an acceleration pickup, and this information was used in calculating the disturbance force imparted to the lens holder by the vibration. Compensation for this force was applied by a proportional controller to reduce the positioning error, as shown in

Fig. 4.12. After testing the positioning performance of the actuator under vibration in the X-direction, the actuator was re-attached to the load table after rotation through 90°, so that the positioning performance of the actuator under vibration in the Y-direction could also be tested.

During the test, two different types of vibration were applied to the maglev lens driving actuator. Fig. 4.22 shows a half sine wave type acceleration applied to the actuator measured by the accelerometer, the actuator was accelerated to more than 40m/s^2 (4G) and then returned to 0m/s^2 within 10ms; Fig. 4.23 shows a sine wave type acceleration applied to the actuator measured by the accelerometer, the actuator was vibrated continuously under a pick acceleration amplitude of ±20m/s^2 (2G) at 50Hz.

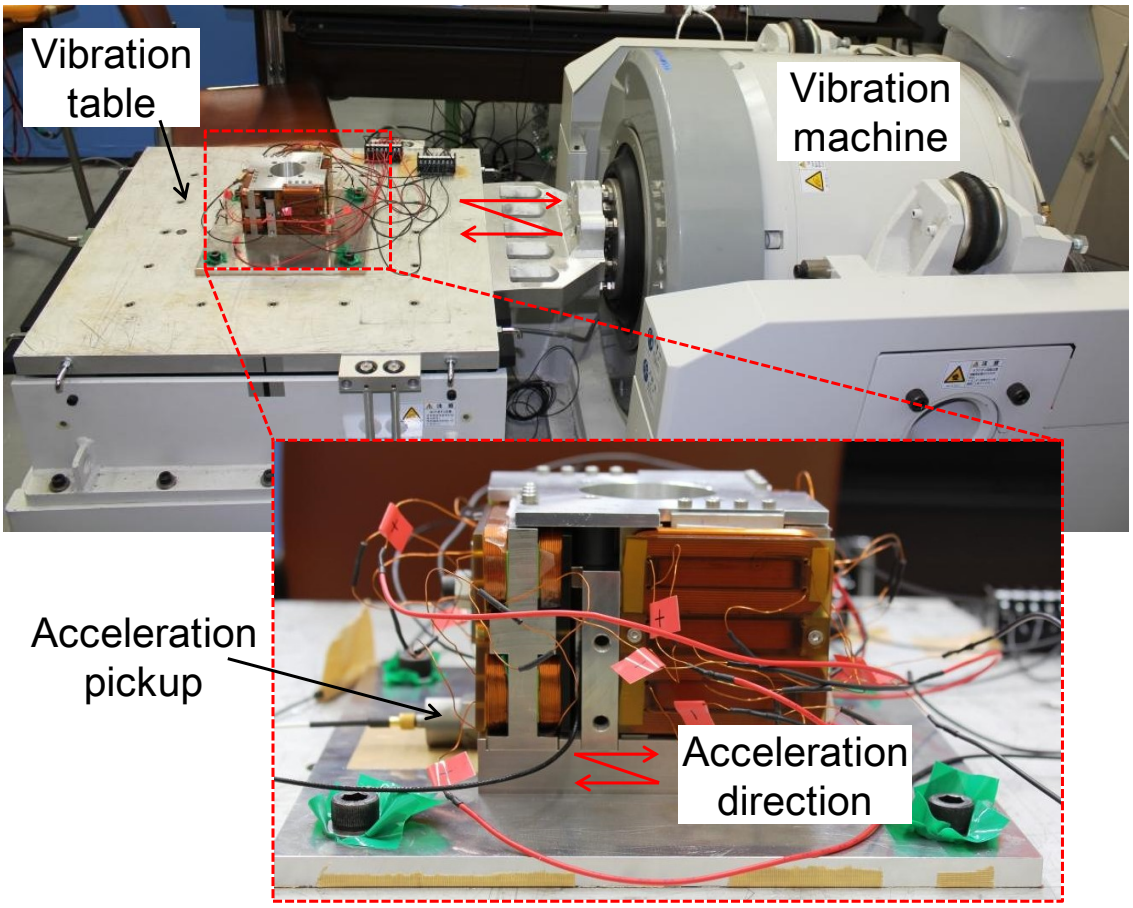

Fig. 4.21 Experiment setup of vibration test

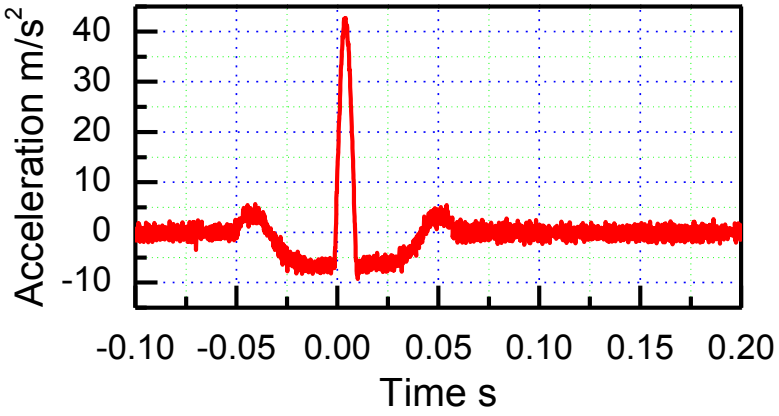

Fig. 4.22 Half sine wave acceleration

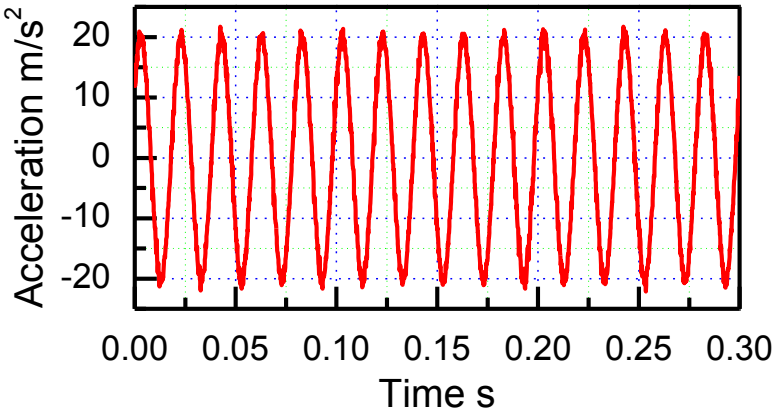

Fig. 4.23 Sine wave acceleration

The settings of the vibration condition are based on the working conditions of a laser cutting machine tool (ML3015NX, Mitsubishi Electric Corp.) in which the actuator is to be installed.

Fig. 4.24 shows the positioning error of the lens holder under half sine wave acceleration in the X-direction. During the vibration test, the positioning errors for the lens holder at the +0.5mm, 0mm and -0.5mm positions in the X-direction were recorded. The results show that the compensation for the positioning errors caused by the 40m/s^2, 10ms half sine wave acceleration was successfully accomplished, with the positioning errors being less than ±10μm in all positions.

Fig. 4.25 shows the positioning error of the lens holder under sine wave acceleration in the X-direction. During the vibration test, the positioning errors for

the lens holder at the +0.5mm, 0mm and -0.5mm positions in the X-direction were recorded. The results show that the compensation for the positioning errors caused by the 20m/s^2, 50Hz sine wave acceleration was successfully accomplished, with the positioning errors being less than ±10μm in all positions.

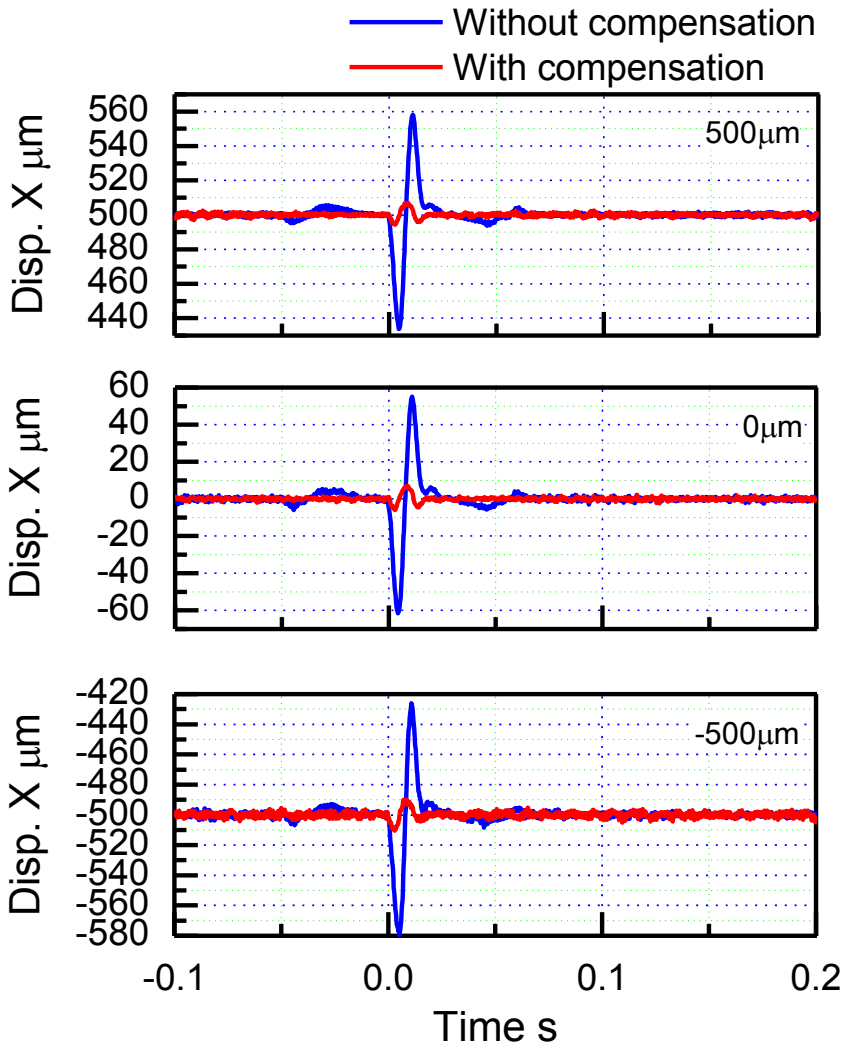

Fig. 4.24 Positioning error under half sine wave acceleration (4G, 10ms) in the X-direction

Fig. 4.26 and Fig. 4.27 show the tracking errors of the lens holder in the X-Y plane at the origin point. According to the results, when the maglev lens driving actuator was accelerated under 40m/s^2, 10ms half sine wave acceleration and 2G, 50Hz sine wave acceleration in the X-direction, positioning errors were only detected in the accelerated direction. After compensation, the tracking errors of

the lens holder were less than ±10μm in the both X- and Y-directions.

The results of vibration test in the Y-direction, which are not shown, are almost identical to those in the X-direction.

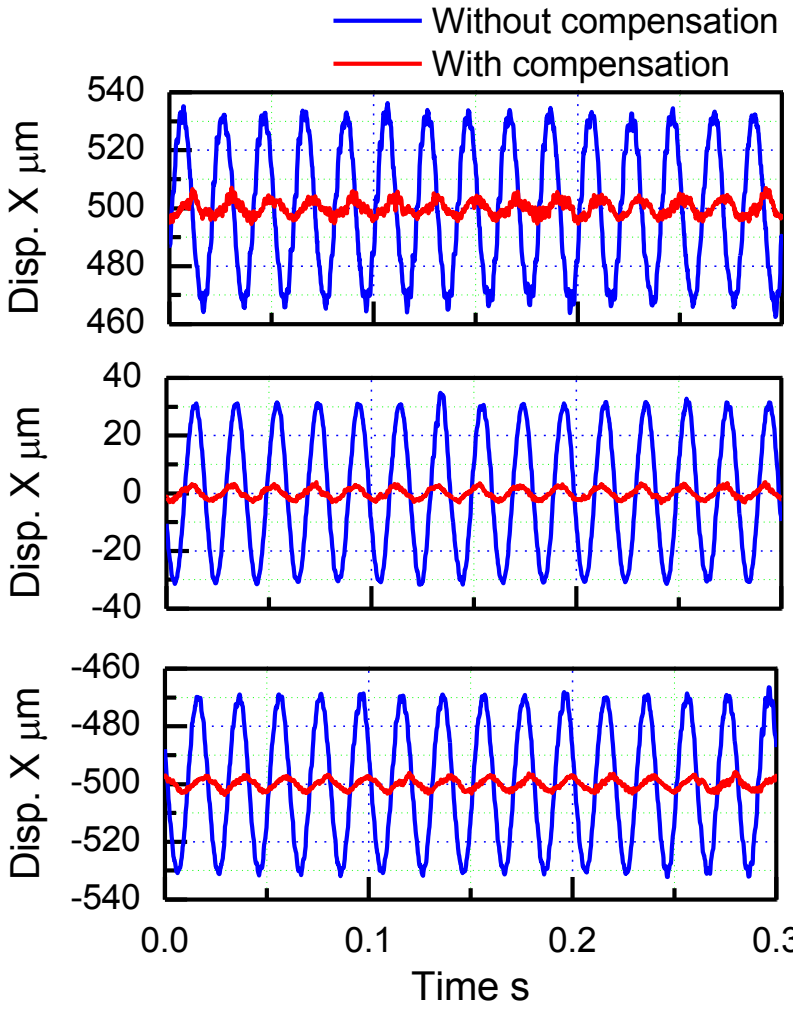

Fig. 4.25 Positioning error under sine wave acceleration (2G, 50Hz) in the X-direction

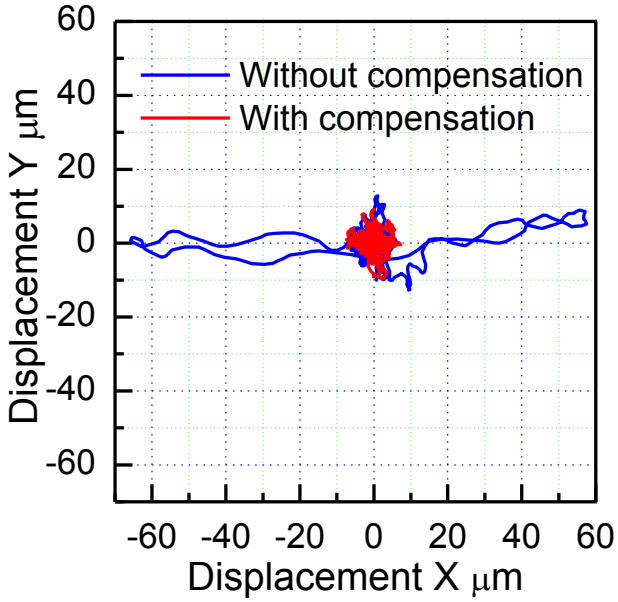

Fig. 4.26 Tracking error under half sine wave acceleration (4G, 10ms) in the X-direction

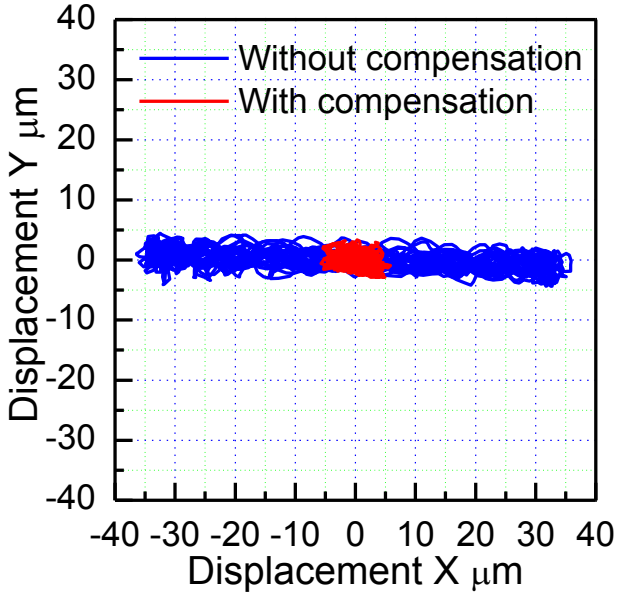

Fig. 4.27 Tracking error under sine wave acceleration (2G, 50Hz) in the X-direction

4.5 Conclusion

In order to realize real-time control of the eccentricity between the lens axis

and the assist gas supply nozzle axis during two-dimensional off-axis laser beam cutting, as well as real-time adjustment of the focal point of a laser beam in laser cutting, cladding and deep piercing etc., a maglev lens driving actuator was proposed and fabricated.

A novel air core coil type electro-magnetic driving unit was designed to actuate the lens holder. The driving unit can generate both repulsive and attractive forces by utilizing a modified Halbach array on the driven target and the air core coils. The air core coil windings allowed a spatial-cross-arrangement of the components, enabling the actuator to be sufficiently compact for it to be accommodated in the machining head of a laser beam machining tool.

Four electro-magnetic driving units were off-set from X- and Y-axis and symmetrically arranged around Z-axis for driving a lens holder. The actuator was designed so that the lens could be driven with a full positioning stroke of ±1mm with a tracking error of less than 1μm in the X- and Y-directions and with a full positioning stroke of ±5mm with a tracking error of less than 12 μm in the Z-direction. The bandwidths are greater than 100Hz in all three orthogonal directions. The prototype actuator has a compact size of 124mm×124mm×101mm so that it can be accommodated in a conventional laser machine tool.

Under half sine wave acceleration (40m/s2, 10ms) and sine wave acceleration (2G, 50Hz) in the X- and Y-directions, compensation for the disturbance was implemented so that the actuator controls the lens holder to maintain a tracking error of less than ±10μm.

In future work, the prototype maglev lens driving actuator will be installed in a laser beam machining tool, so that the effectiveness of off-axis control of the lens and adjustment of the focal point of the laser beam on the machining speed and quality can be experimentally investigated.

Chapter 5 Conclusion

5.1 Summary

In order to increase the machining speed and quality in electrical discharge machining (EDM) and laser beam machining (LBM), additional high speed and multi-DOF maglev actuators were developed in this study. In this thesis, the development of a 5-DOF maglev electrode driving actuator (chapter 2) and its effectiveness on the machining speed of small hole and micro hole EDM (chapter 3); and the development of a maglev lens driving actuator (chapter 4) were introduced and discussed.

In the EDM project, a maglev electrode driving actuator was designed and fabricated; the maglev actuator enabled an electrode, which is attached to a levitated spindle shaft, to realize a faster positioning response than a conventional EDM machine tool in three orthogonal and two tilt directions. Meanwhile, a novel magnetic coupling mechanism in the maglev electrode driving actuator realized the electrode rotation, and realized discharge voltage supply to the electrode without disturbing its multi-DOF motion and rotation. For the purpose of increasing the machining speed in EDM, the effectiveness of fast positioning response of the electrode, electrode rotation, and their combination realized by the developed maglev electrode driving actuator was experimentally investigated.

In the LBM project, a maglev lens driving actuator was designed and fabricated. By using a novel air core coil type electro-magnetic driving unit, the maglev lens driving actuator realized high speed off-axis control in radial direction and focal point adjustment in axial direction.

The content of this research is summarized as follows:

Chapter 1 "Introduction"

This chapter first described the basic concept of electrical discharge machining (EDM) and laser beam machining (LBM), as well as the challenges

encountered in EDM and LBM for achieving higher machining speed and better machining quality.

In the EDM, in order to increase the machining speed and quality, an electrode should be rapidly positioned for maintaining a suitable gap distance to a work-piece; orbital motion, rotation, tilt motion and jump motion of the electrode are required for obtaining stable electrical discharge by removing the debris accumulated around electrode during EDM process.

In the LBM, in order to reduce the assist gas consumption and increase the laser beam cutting speed and quality, high speed real-time off-axis control is required; in order to increase the machining speed and the aspect ratio of machined hole in laser piercing, adjustment of the laser beam focal point is needed.

Conventional machine tools for EDM and LBM cannot realize the functions mentioned above. Therefore, supplementary actuators for driving an electrode in EDM and for driving a lens in LBM were developed using maglev technology in this study. The use of such technology could enable the actuators to have a fast response, a simple structure, be compact, etc.

Chapter 2 “Maglev electrode driving actuator for EDM”

This chapter introduced the mechanical structures and the experimental performance of a compact maglev electrode driving actuator. The developed prototype maglev actuator realizes 5-DOF motion of a spindle shaft by two radial magnetic bearings and one thrust magnetic bearing. The Lorentz type thrust had a long positioning stroke and the generated driving force was quite linear to the applied current and bias displacement.

An electrode was attached to the levitated spindle shaft. A magnetic coupling mechanism was proposed to realize discharge voltage supply without direct contact between brushes and levitated spindle shaft, as well as transmit

rotational torque from a DC motor to the levitated spindle shaft for rotating the attached electrode. Furthermore, the magnetic coupling generated a restoring force to balance the gravity of the spindle shaft, which decreased the power consumption.

Experimental results indicated that the prototype actuator possessed sub-micron positioning resolution with an angular resolution of several micro-radians, bandwidths greater than 200 Hz in the 5-DOF directions, and positioning strokes of 2mm in the thrust direction, 180μm in the radial direction and 3.6mrad in tilt direction, respectively. Moreover, the spindle shaft could be rotated smoothly at up to 2000rpm with vibration amplitudes of less than 1.5μm and 30μrad, while the discharge current could be fed to the electrode while the spindle shaft was rotating without any friction force induced by the power supply brushes.

Chapter 3 “Experimental EDM using the maglev electrode driving actuator”

This chapter firstly discussed the problems of applying the prototype maglev electrode driving actuator to experimental EDM and the solutions. The positioning stroke of the prototype actuator was not enough for machining a deep hole with depth than 2mm, a co-operatively controlled EDM system using the prototype maglev electrode driving actuator combined with a conventional EDM machine was proposed to solve this problem.

The co-operative EDM system realized as large travel range of the electrode as that of the conventional EDM machine, and realized as fast positioning response of the electrode as that of the prototype maglev electrode driving actuator.

A new electrode attachment mechanism having a better coaxiality between the spindle shaft and the attached electrode was designed and fabricated; which decreased the electrode rotational error from ±35μm to less than ±5μm.

Secondly, experimental EDM of ϕ0.5mm×4mm and ϕ1mm×4mm through holes were also presented in this chapter. The co-operative EDM system increased the positioning response of the electrode, so that the electrode was positioned more rapidly. Therefore, without electrode rotation, the co-operative EDM increased machining rate by 125% and 337% in ϕ0.5mm×4mm and ϕ1mm×4mm though hole EDM, respectively, compared to the conventional EDM machine.

In co-operative rotary EDM, electrode rotation helped removing the debris accumulated around the electrode, and this enabled more stable electrical discharge. Therefore, electrode rotating at 800rpm increased machining rate by maximum of 97% in ϕ0.5mm×4mm though hole EDM; and electrode rotating at 600rpm increased machining rate by maximum of 22% in ϕ1mm×4mm though hole EDM.

Finally, micro hole EMD was also conducted. ϕ60μm×2.4mm micro electrodes were on-machine fabricated for eliminating the clamping error. Without electrode rotation, both co-operative EDM and conventional EDM machine failed to machine through a 1mm work-piece. Within the same feeding range, the co-operative EDM machined a deeper hole within shorter time than the conventional EDM machine. Co-operative EDM with electrode rotating at 800rpm machined a 1mm micro through hole with diameter less than 0.1mm.

Chapter 4 “Maglev lens driving actuator for LBM”

This chapter presented a maglev lens driving actuator for realizing a real-time high speed relative displacement between a lens and an assist gas nozzle in radial directions and for adjusting the laser beam focal point in axial direction.

In the maglev lens driving actuator, a lens holder was actuated by four novel electro-magnetic driving units. In each driving unit, a modified Halbach PM array was mounted to the lens holder, and air core driving coils were fixed on the base.

The modified PM array generated enhanced magnetic field on both side, driving forces was generated to the lens holder in both radial and axial directions by air core coils on the base, and long travel range with lower nonlinearity of the lens holder was also achieved. The air core coil windings allowed a spatial-cross-arrangement of the components, enabled the actuator to realize a compact size of 121mm×121mm×101mm.

In the fabricated prototype maglev lens driving actuator, a large aperture in the center of the lens holder was used to attach a ϕ50.8mm lens and to pass the high energy laser beam. Radial displacement of the lens up to ±1mm with a tracking error of 1μm and a bandwidth of more than 150Hz was achieved; and a ±5mm stroke of the lens with a tracking error of less than 3μm and a bandwidth of more than 100Hz was also obtained in the axial direction.

In experimental high speed laser beam cutting, the maglev lens driving actuator should be driven under a high acceleration from 2G to 4G. Therefore, vibration test was also conducted in order to confirm the positioning performance of the maglev actuator.

Under external half sine wave (4G, 10ms) and sine wave (2G, 50Hz) acceleration in the radial direction, the prototype maglev lens driving actuator maintained a tracking error of the lens holder less than 10μm by using an acceleration compensator.

5.2 Future works

5.2.1 Future works of the EDM project

The developed maglev electrode driving actuator enabled high speed and high accuracy motion control of an electrode in three orthogonal and two tilt directions. In future work, attitude compensation of the electrode in radial and tilt directions for eliminating electrode clamping error and tapper error of machined hole will be experimentally investigated. The positioning range of the electrode in

radial and tilt directions are planning to be extended if necessary.

The jump motion, combination of rotation and orbital motion of electrode are supposed to be effective for debris removing. The effectiveness of those motions of electrode to the machining speed and accuracy will also be investigated.

5.2.2 Future works of the LBM project

The developed prototype maglev lens driving actuator realized sufficient positioning performance of the lens. In the next step, the prototype maglev lens driving actuator will be installed in a laser beam machining tool, so that the effectiveness of off-axis control of the lens and adjustment of the focal point of the laser beam on the machining speed and quality can be experimentally evaluated.

Since the prototype maglev lens driving actuator realized unique motions of the lens which cannot be realized by conventional LBM machine tools, new laser beam machining methods using the high speed motions of a lens will be attempted.

Furthermore, the prototype maglev lens driving actuator realized much larger positioning range than that of the 5-DOF maglev electrode driving actuator, and with the same positioning error magnitude. Therefore, experimental EDM is planning to be conducted using the maglev lens driving actuator by attaching an electrode to the lens holder.

References

[1] Kunieda M, Lauwers B, Rajurkar K, Schumacher B. Advancing EDM through Fundamental Insight into the Process. CIRP Annals, 2005; 54; 64-87

[2] Boothroyd G, Winston AK. Non-conventional machining processes. Fundamentals of Machining and Machine Tools. Marcel Dekker, Inc, New York, 1989; p491

[3] McGeough JA. Electrodischarge machining. Advanced Methods of Machining. Chapman & Hall, London, 1988; p130

[4] Ho HK, Newman TS. State of the Art Electrical Discharge Machining (EDM). International Journal of Machine Tools and Manufacture, 2003; 43(13); 1287-1300

[5] Varanasi K, Nayfeh S, The Dynamics of Lead-screw Drives: Low-Order Modeling and Experiments. Trans ASME J Dyn Syst Meas Control, 2004; 126; 388-396

[6] Zhao Y, Zhang X, Liu, Yamazaki K. Geometric Modeling of the Linear Motor Driven Electrical Discharge Machining (EDM) Die-sinking Process. International Journal of Machine Tools & Manufacture, 2004; 44; 1-9

[7] Dubey AK, Yadava V. Laser beam machining--A review. International Journal of Machine Tools & Manufacture, 2000; 48; 609-628

[8] Duan J, Man HC, Yue TM. Modeling the laser fusion cutting process: I. Mathematical modeling of the cut kerf geometry for laser fusion cutting of thick metal. J. Phys. D: Appl. Phys, 2001; 34; 2127-2134

[9] Golnabi H, Bahar M. Investigation of optimum condition in oxygen gas-assisted laser cutting. Optics & Laser Technology, 2009; 41; 454-460

[10] Kovalev OB, Yudin PV, Zaitsev AV. Modeling of flow separation of assist gas as applied to laser cutting of thick metal. Applied Mathematical Modeling, 2009; 33; 3730-3745

[11] Quintero F, Pou J, Lusquinos F, Boutinguiza M, Soto R, Perez-Amor M. Comparative study of the influence of the gas injection system on the Nd:yttrium-aluminum-garnet laser cutting of advanced oxide ceramics. Review of Scientific Instruments, 2003; 74; 4199-4205

[12] Ketting HO, Olsen FO. High pressure off-axis laser cutting of stainless steel and aluminum. Proceedings of ILAMP, Nagaoka, Japan, 1992; 607-612

[13] Quintero F, Pou J, Fernandez JL, Doval AF, Lusquinos F, Boutinguiza M,

Soto R, Perez-Amor M. Optimization of an off-axis nozzle for assist gas injection in laser fusion cutting. Optics and Laser in Engineering, 2006; 44; 1158-1171

[14] Riveiro A, Quintero F, Lusquinos F, Comesana R, Pou J. Effects of processing parameters on laser cutting of aluminum-copper alloys using off-axial supersonic nozzles. Applied Surface Science, 2011; 257; 5393-5397

[15] Xie SQ, Tu YL, Shaw A, Duan ZC. A fuzzy integral sliding mode control algorithm for high-speed laser beam focus tracking control. International Journal of Advanced Manufacturing Technology, 2002; 20; 296-302

[16] Bordatchev EV, Nikumb SK. Effect of focus position on informational properties of acoustic emission generated by laser-material interactions. Applied Surface Science, 2006; 253; 1122-1129

[17] Tam SC, Yeo CY, Jana S, Lau MWS, Lira LEN, Yang LJ, Noor YM. Optimization of laser deep-hole drilling of Inconel 718 using the Taguchi method. Journal of Material Processing Technology, 1993; 37; 741-757

[18] Fox MDT, French P, Peters C, Hand DP, Jones JDC. Applications of optical sensing for laser cutting and drilling. Applied Optics, 2002; 41; 4988-4955

[19] Wang XC, Zheng HY, Chu PL, Tan JL, Teh KM, Liu T, Ang BCY, Tay GH. High quality femtosecond laser cutting of alumina substrates. Optics and Lasers in Engineering, 2010; 48; 657-663

[20] Yao Q, Dong J, Ferreira P. A novel parallel-kinematics mechanisms for integrated, multi-axis nanopositioning Part 1. Kinematics and design for fabrication. Precision Engineering, 2008; 32; 7–19

[21] Yao Q, Dong J, Ferreira P. A novel parallel-kinematics mechanisms for integrated, multi-axis nanopositioning Part 2: Dynamics, control and performance analysis. Precision Engineering, 2008; 32; 20–33

[22] Huang Z, Tao WS, Fang YF. Study on the kinematic characteristics of 3 DOF in-parallel actuated platform machanism. Mech. Mach. Theory, 1996; 31(8); 999-1007

[23] Magnetic bearings-a new world opens for design engineers. World Pumps, 2003; 446; 21-25

[24] Jayawant B.V. Electromagnetic suspension and levitation techniques. Proc. R. Soc. Lond A, 1988; 416; 245-320

[25] Active magnetic bearings for turbo-machinery. Tribology International, 1978; 11(4); p257

[26] Shi L, Yu A, Yang G, Shi Z, Xu Y. Technical design and principle test of active magnetic bearing for the turbine compressor of HTR-10GT. Nuclear Engineering and Design, 2012; doi:10.1016/j.nucengdes.2011.11.037

[27] Gourc E, Seguy S, Arnaud L. Chatter milling modeling of active magnetic bearing spindle in high-speed domain. International Journal of Machine Tools & Manufacture, 2011; 51; 928-936

[28] Holmes M, Hocken R, Trumper D. The long-range scanning stage: a novel platform for scanned-probe microscopy. Precision Engineering, 2000; 24; 191-209

[29] Shinno H, Yoshioka H, Taniguchi K. A newly developed motor-driven aerostatic X-Y planar motion table system for nano-machining. Annals of the CIRP, 2007; 56; 369-372

[30] Kim W, Trumper D. High precision magnetic levitation stage for photolithography. Precision Engineering, 1998; 22; 66–77

[31] Morimoto Y, Shinshi T, Okamoto T, Nakai T. A TWO-DOF Controlled Lens Drive Actuator for Off-Axis Laser Beam Cutting. Proceeding of the 6th International Conference on Leading Edge Manufacturing in 21st Century, 2011; No. 3376

[32] Imai Y, Satake A, Taneda A. Improvement of EDM Machining Speed by Using High Frequency Response Actuator. International Journal Electrical Machining, 1996; 1; 21–26

[33] Masuzawa T, Tanaka K, Fujino M. Study on the High Speed Machining by EDM Using a Moving Coil Head Type Feed Control. Proc. of the 19th International MTDR Conference, 1978; 543-549.

[34] Imai T, Nakagawa T, Miyake H, Hidai H, Tokura H. Local Actuator Module for Highly Accurate Micro-EDM. Journal of Materials Processing Technology, 2004; 149(3); 328-333

[35] Ghoreishi M, Atkinson J. A comparative experimental study of machining characteristic in vibratory, rotary and vibro-rotary electro-discharge machining. Journal of Material processing Technology, 2001; 120; 374-384

[36] Soni JS, Chakraverti G. Machining characteristics of titanium with rotary electro-discharge machining. Wear, 1994; 171; 51-58

[37] Wang CC, Yan BH. Blind-hole drilling of Al203/6061Al composite using rotary electro-discharge machining. Journal of Material processing Technology, 2000; 102; 90-102

[38] Mohan B, Rajadurai A, Satyanarayana KG. Effect of SiC and rotation of

electrode on electric discharge machining of Al-SiC composite. Journal of Material processing Technology, 2002; 124; 297-304

[39] Bamberg E, Heamawatanachai S. Orbital electrode actuation to improve efficiency of drillingmicro-holes by micro-EDM. Journal of Materials Processing Technology, 2009; 209; 1826–1834

[40] Hsue A, Chung C. Novel jump control for debris processes of electrical discharge machining with direct-drive spindle. Advanced Materials Research, 2010; 97(101); 4178-4181

[41] Cetin S, Okada A, Uno Y. Electrode jump motion in linear motor equipped die-sinking EDM. Journal of Manufacturing Science and Engineering, 2003; 125; 809-815

[42] Zhang X, Shinshi T, Shimokohbe A, Sato T, Miyake H, Nakagawa T. High-speed Electrical Discharge Machining By Using a 5-DOF Controlled Maglev Local Actuator. Journal of Advanced Mechanical Design, Systems, and Manufacturing, 2008; 2(4); 493-503

[43] Ueyama Y, Zhang X, Shinshi T, Shimokohbe A, Nakagawa T, Sato T, Miyake H. Small-hole Electrical Discharge Machining Using a Maglev Actuator. Journal of the JSPE, 2010; 76(6); 638-642

[44] Zhang X, Shinshi T, Kajiwara G, Shimokohbe A, Imai Y, Miyake H, Nakagawa T. 5-DOF Controlled Maglev Local Actuator and its Application to Electrical Discharge Machining. Precision Engineering, 2008; 32; 289-300

[45] Shinshi T, Iijima C, Zhang X, Choi K, Sato K, Shimokohbe A. Precision Radial Magnetic Bearing. Proc. of the 15th ASPE Annual Meeting, Arizona 2000; 240-243.

[46] Zhang X, Shinshi T, Li L, Shimokohbe A. A combined Repetitive Control for Precision Rotation of Magnetic Bearing. Precision Engineering, 2003; 27; 273-282

[47] He D, Morita H, Zhang XY, Shinshi T, Nakagawa T, Sato T, Miyake H. Development of a novel 5-DOF controlled maglev local actuator for high-speed electrical discharge machining. Precision Engineering, 2010; 34; 453-460

[48] Kunieda M, Hayasaka A, Yang X, Sano S, Araie I. Study on nano EDM using capacity coupled pulse generator. Annals of the CIRP, 2007; 56(1); 213–216

[49] He D, Shinshi T, Zhang XY, Yuzawa T, Sato T. Improving the Speed of Small Deep Hole Electrical Discharge Machining by Combining Rotation of the Electrode with a Rapid-Response. Journal of Advanced mechanical Design,

System, and Manufacturing, 2011; 5(4); 284-294

[50] Chiba A, Fukao T, Ichikawa O, Oshima M, Takemoto M, Dorrell G. Magnetic Bearings and Bearingless Drives. Elsevier, 2005; ISBN: 0750657278

[51] Halbach K. Design of permanent multi-pole magnets with oriented rare earth cobalt materials. Nuclear Instruments and Methods, 1980; 169; 1–10

Acknowledgements

I here express the special gratitude to my academic supervisor, Professor Tadahiko SHINSHI, for the encouragement and valuable advices along the past 4 years of study at Tokyo Institute of Technology. The support he provided me in the studies and life in Japan was fundamental for this work.

I also express special gratitude to Associate Professor Xiaoyou ZHANG in Nippon Institute of Technology and Professor Rongqiang LIU in Harbin Institute of Technology for helping me entered Tokyo Tech, and for their valuable advices and orientations in the study and the life.

I would like to gratefully acknowledge

Professor Haruo HOUJOH

Professor Shinichi YOKOTA

Associate Professor Kaiji SATO

Associate Professor Hayato YOSHIOKA

for the attention and the valuable advices on the elaboration of this work.

Thanks are due to Takashi YUZAWA, Tatsusi SATO, Takahiro NAKAI in Mitsubishi Electric Corporation for the helpful supports and advices along this study.

I express my gratitude to Mr. Hiroki MORITA, who proposed the maglev electrode driving actuator for EDM. I also express my gratitude to Yoshitaka UEYAMA for teaching me the operation method and the advices during the experimental EDM. Thanks to Mr. Atsushi YUMOTO, for his friendship, and

helpful discussions in the course of this study.

Thanks are due to Dr. Wataru HIJIKATA, Dr. Chi Nan PAI, Mr. Shunji GOTO, Mr. Ryo TANABE, Mr. Masato ISHIBASHI, Mr. Manabu UEDA, Mr. Daigo FUJII, Mr. Taichi MAMIYA, Mr. Hirofumi SASAKI, Mr. Chao ZHI, Mr. Yoshihiro MORIMOTO, Miss Yiling SUN, Mr. Kou MOMOSE, Mr. I RYUU, Mr. Ryogen FUJIWARA, Mr. Shodai ABE, and Mr. Takatoki SHIMADA for their friendship and enthusiasm in the course of this study.

Thanks are due to the Japanese Government that provided me the scholarship along the 4 years of study at Tokyo Tech.

Finally, I wish to dedicate this work to my parents, for their lifelong support.

Dongjue HE

August 3rd, 2012